Oceanic hydrodynamic processes around the Shetland Islands

A data study on the prevailing ocean conditions and main characteristics

J. (Jenske) Kroes

October 2018

Delft University of Technology

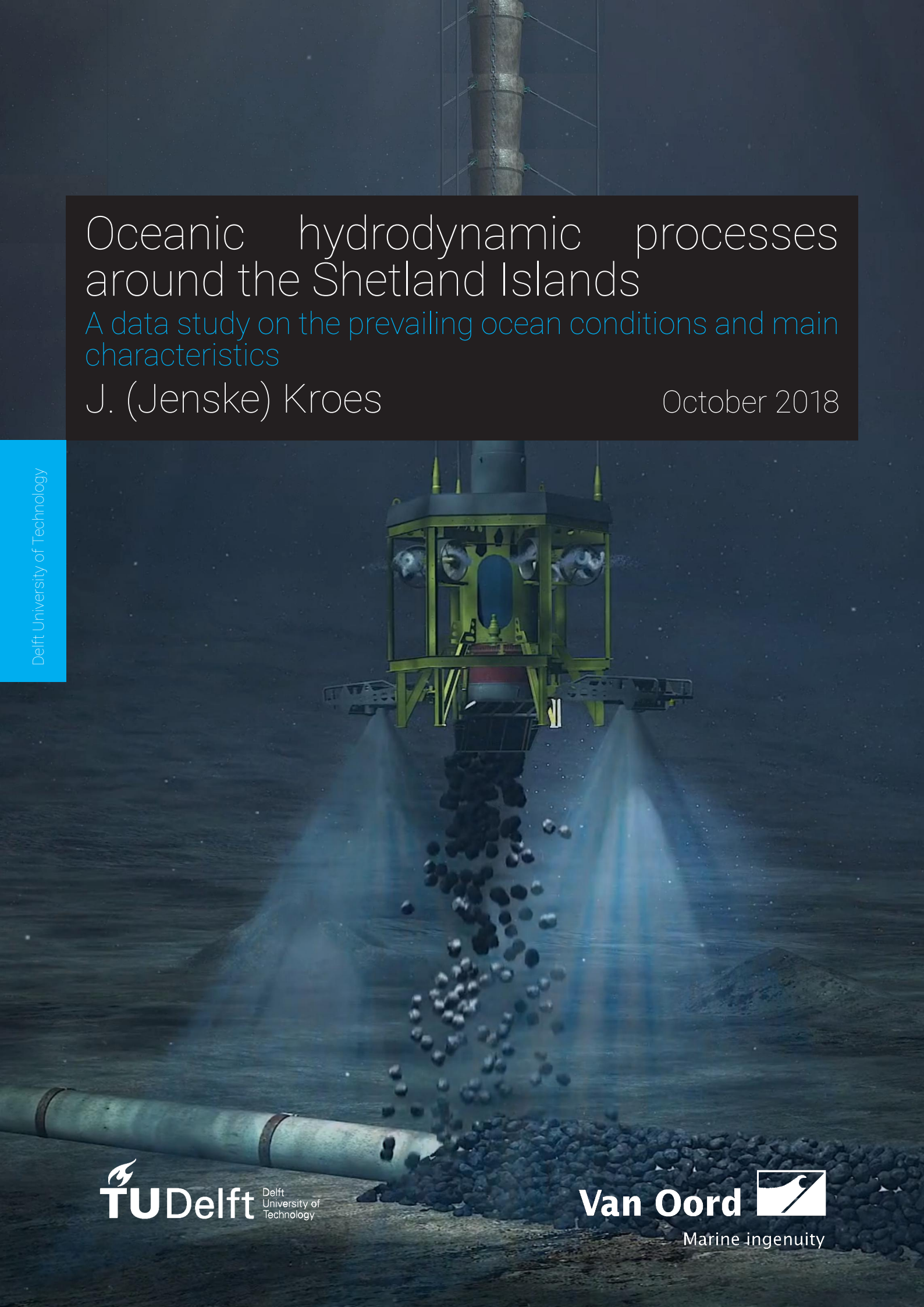

TU Delft Delft University of Technology

Van Oord
Marine ingenuity

Cover image: Remotely Operated Vehicle covering a pipeline with rocks, on the bottom of the ocean (retrieved and adapted from Van Oord (2018)).

Oceanic hydrodynamic processes around the Shetland Islands

A data study on the prevailing ocean conditions and main characteristics

by

J. (Jenske) Kroes

in partial fulfilment of the requirements to obtain the degree of

Master of Science
in Hydraulic Engineering

at the faculty of

Civil Engineering and Geosciences

at

Delft University of Technology

to be defended publicly on Thursday October 11, 2018 at 1:00 PM.

Student number:	4143949	
Project duration:	February 20, 2018 – October 4, 2018	
Thesis committee:	Prof. dr. J.D. Pietrzak	TU Delft
	Prof. dr. ir. M. Verlaan	TU Delft & Deltares
	Dr. C.A. Katsman	TU Delft
	Dr. ir. G.J. de Boer	Van Oord

An electronic version of this thesis is available at http://repository.tudelft.nl/.

TU Delft Delft University of Technology

Van Oord
Marine ingenuity

Preface

It feels strange to think about the content of the final part of my graduation thesis, which is also my very last text that I will write as a student of Delft University of Technology. I still need to get used to the idea that I will officially become an engineer in less than two weeks. From February until now, I dived, not literally, into the oceanic hydrodynamic processes around the Shetland Islands. I tried to find out which phenomenon compromises the working conditions of the SRI vessels owned by Van Oord. This was a challenging task, as data or measurements from this area are scarce. In my opinion, I did not completely solve the problem. However, I think the conclusions are valuable for the SRI department at Van Oord.

I would like to name a few people who helped me during the project and without whom I would never have achieved this result. First, thanks to Julie Pietrzak and Caroline Katsman for sharing your infinite knowledge of the ocean with me. The two of you also reminded me of the academic level of my formulations and argumentation, which is, unfortunately, one of my weaker points. I also would like to thank Martin Verlaan, who provided me with data from his hydrodynamic model, which is quite an essential aspect of this research. You also came up with smart and practical solutions for the problem, which I really appreciated.

And of course, many thanks to Gerben de Boer, for being such an inspiring supervisor at Van Oord. You gave me a lot of freedom and responsibility, so I could make this project totally my own. I really enjoyed our (almost) weekly 30 minute meetings, in which we came up with new ideas and plans. I learned to make notes extremely fast, as the information density from your side is always **very** high. Your tricks (Dutch: *ezelsbruggetjes*) for the wind and flow direction and Tufte's 'Information over Ink ratio' will never be erased from my memory. I really hope we can work together again in the future!

Last, but not least, I would like to thank Sam for all his support throughout this project. By asking me *'Why do you want to do this or that?'* on a regular basis, you kept me sharp and self-critical on my ideas. This was exactly what I needed. You also operated as a Python help-desk, which I sometimes used for the impossible bugs in my scripts. In one month, we will go to 'your' Oman for an amazing holiday. I cannot wait!

On to the next step, which is working at Van Oord. I am really looking forward to learning much more about marine processes and develop myself into a professional hydraulic engineer.

J. (Jenske) Kroes
Delft, October 2018

Summary

From 2014 to 2017, Van Oord executed multiple Subsea Rock Installation (SRI) projects at two different locations in the vicinity of the Shetland Islands, situated north of the United Kingdom in the Atlantic Ocean. These projects have a duration of multiple weeks or months, in which rocks are placed on top of pipelines by flexible fallpipe vessels. The fallpipe consists of a sequence of steel and synthetic buckets and a Remotely Operated Vehicle (ROV), which contains measuring devices, is located at the end. During the installation activities around the Shetland Islands, the vessels of Van Oord are exposed to all kinds of weather and flow conditions. Under certain conditions, the fallpipe and the ROV cannot hold their dynamic position above the pipeline without risking a pop-out of one of the buckets. This leads to an undesirable and expensive interruption of the activities, as the day rate of an SRI vessel is high.

The interruptions of activities are hypothesised to be the result of the prevailing hydrodynamic conditions, because the SRI vessels only experience this behaviour west of the Shetland Islands. This research can be considered as a detective story, in which all available resources are deployed to solve the whodunnit. In other words, which phenomena or processes are responsible for the interruption of the installation activities. The following four types of data are used:

- Hydrodynamic data of four full years from the 3D Dutch Continental Shelf Model (3D DCSM-FM) by Zijl et al. (2016), which is the most suitable available model;
- Daily Progress Reports (DPR) indicating the begin and end times of the 55 non-working intervals reported on the vessels during five different projects;
- Data from the Automatic Identification System (AIS), which stores the positional data of a vessel;
- Data of the sensors located on the ROV of an SRI vessel, which consists of 25 Hz time series downsampled to one minute.

The data from the different sources is combined into overview plots, to be able to identify possible patterns. This is done for ten tracks, consisting of a subsequent number of days that a vessel was working on a project around the Shetland Islands. An example of a part of such an overview plot is depicted in Figure 1.

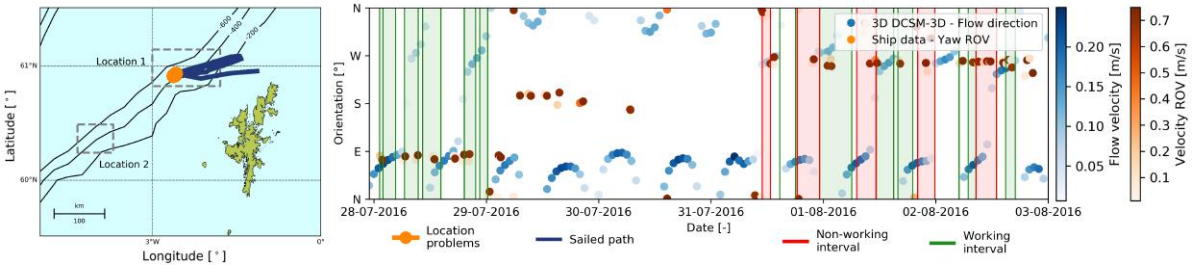

Figure 1: Part of an overview plot for the period ranging from 28-07-2016 to 03-08-2016. On the left, a map of the area around the Shetland Islands is presented, including project Location 1 and 2. The blue track represents the sailed path of the SRI vessel. On the right side a graph is plotted, which contains the magnitude and orientation (yaw) of both the ROV and the flow velocity [m/s]. The red and green vertical lines represent the working and non-working intervals of the vessel.

Based on the analysis of all the full-scale overview plots, two major conclusions can be drawn regarding Location 2. First, in case the tidal flow is oriented to the east or east-northeast in the bottom part of the water column at Location 2, it is highly likely that the working activities are interrupted. This conclusion follows from a flow rose of the dataset. The rose indicates that tidal flow to the east results in non-working conditions in 100% of the cases, whereas tidal flow oriented to the east-northeast has a probability of 88%. Secondly, for values of the turbulent vertical eddy viscosity in the bottom part of the water column higher than 10^{-2} m^2/s,

the chance on non-working conditions at Location 2 increases significantly. The probability increases from 12% for a value of 0.01 m^2/s, to 39% for a value of 0.0146 m^2/s and 82% for a value of 0.028 m^2/s. A similar percentual distribution yields for the turbulent kinetic energy and the turbulent energy dissipation.

As the tide seems to play a significant role in the area around the Shetland Islands, a Fast Fourier Transform (FFT) is performed in order to quantify the characteristics. With the FFT the main tidal frequencies are filtered from the original flow velocity signal and the remaining frequencies in the signal are determined. In this case, the filtered tidal signal explains 80% of the variance, whereas the value for the residual signal is 20%. However, the amplitude of the residual flow velocity signal still has approximately the same value as the original signal. As the major part of the energy in the residual spectrum is centred around a frequency of 1.7 cycles per day (cpd) it can be assumed that this frequency dominates the residual movement. This is most likely caused by the presence of inertial waves, which have a frequency of 1.72 cpd in the area of the Shetland Islands. Nevertheless, the residual flow velocity signal is relatively constant in time, so no correlation with the working or non-working intervals can be identified.

An additional analysis of the behaviour of the ROV during working and non-working intervals is performed based on the logged sensor signals of the SRI vessels. This analysis indicates that the average distance between the ROV and the moonpool, which is the launching platform of the ROV, is similar for working and non-working intervals. Moreover, the maximum deviation of the ROV is larger for working intervals. During working intervals, the distance between the moonpool and the pipeline is approximately twice the distance between the ROV and the pipeline. For the non-working intervals, the deviation of the ROV is two-thirds of the deviation of the moonpool.

Furthermore, scatter plots of the turbulent vertical eddy viscosity and both the roll and the pitch of the ROV indicate that a high value of the pitch or roll (2°-3°) does not immediately lead to an interruption of the working activities. Therefore, it is assumed that both the roll and the pitch of the ROV are not singularly responsible for the downtime of the SRI vessel. For the other variables, such as the velocity and the horizontal power, no clear correlation between the behaviour over time and the presence of a working or a non-working interval is found.

From all types of analysis performed in this study, it can be concluded that, in general, no unambiguous pattern or correlation between the prevailing conditions in the ocean and an interruption of the activities has been found. This might be due to the interpolation applied to the output of the 3D DCSM-FM or the fact that certain processes, such as internal tide or waves, are not specifically included in this hydrodynamic model. Also, only ten of the tracks are considered suitable for this analysis, whereas 25 tracks are available. By disregarding the remaining fifteen tracks, possible patterns or correlations can be overlooked. However, an alternative hypothesis is that the problems are caused by a combination of the hydrodynamic conditions and the characteristics of the SRI vessel and the fallpipe in particular. For example, the eigenfrequency of the fallpipe can be relevant, as oscillations might be induced by the (short) appearance of a hydrodynamic phenomenon.

For further research into this topic, a few things are recommended. First, one could analyse the variation of the magnitude and direction of the flow over the water column by means of a theoretical dynamic Ekman layer model. This will provide more insight in the shear and veering patterns in the water column. The second recommendation regards an in-depth analysis of the characteristics and the behaviour of the fallpipe structure, by studying the eigenfrequencies, as oscillations might be induced by the (short) appearance of a hydrodynamic phenomenon. Lastly, Van Oord can consider to change the working method of the SRI vessels. Instead of working in one direction covering a pipeline section, the vessel adapts the working direction to the orientation of the tidal flow. In this way, each six hours the vessel changes direction, resulting in less downtime.

Contents

List of Tables

List of Figures

Nomenclature

Abbreviations

Abbreviation	Full name
3D DCSM-FM	3D Dutch Continental Shelf Model-Flexible Mesh
ADCP	Acoustic Doppler Current Profiler
AIS	Automatic Identification System
BODC	Britisch Oceanic Data Centre
CPD	Cycles Per Day
DPR	Daily Progress Report
GEBCO	General Bathymetric Chart of the Oceans
HiRLAM	High-Resolution Limited Area Model
HYCOM	HYbrid Coordinate Ocean Model
INS	Inertial Navigation System
ISOW	Iceland Scotland Overflow Water
MEIC	Modified East Icelandic Current
MNAC	Modified North Atlantic Current
MRU	Motion Response Unit
NAC	North Atlantic Current
NOAA	National Oceanic and Atmospheric Administration
NSAIC	Norwegian Sea Arctic Intermediate Current
NSDWC	Norwegian Sea Deep Water Current
NWP	Numerical Weather Prediction
ROV	Remotely Operated Vehicle
SRI	Subsea Rock Installation
TAPPY	Tidal Analysis Program in Python

Latin symbols

Symbol	[Units]	Description
A_i	[m]	Amplitude of component i of the signal
a_{ROV}	[m/s^2]	Acceleration of the ROV
a_M	[m/s^2]	Gravitational pull of the Moon on 1 kg of mass of the Earth

Symbol	[Units]	Description
a_S	[m/s^2]	Gravitational pull of the Sun on 1 kg of mass of the Earth
B	[-]	Coefficient for the Equation of State
B_i	[m]	Amplitude of component i of the signal
C	[-]	Coefficient for the Equation of State
$C_{D,fp}$	[-]	Drag coefficient of the fallpipe
$C_{D,ROV}$	[-]	Drag coefficient of the ROV
c	[m/s]	Wave propagation speed
c_e	[m/s]	Propagation speed of an external wave
c_i	[m/s]	Propagation speed of an internal wave
D	[s]	Duration of the recorded signal
d_{fp}	[m]	Diameter of the fallpipe
d_M	[m]	Distance between Earth and Moon = $384 \cdot 10^6$
d_{ROV}	[m]	Diameter of the ROV
d_S	[m]	Distance between Sun and Earth = $150 \cdot 10^9$
$F_{Z,fp}$	[N]	Gravity force on the fallpipe
$F_{Z,ROV}$	[N]	Gravity force on the ROV
$F_{B,fp}$	[N]	Buoyancy force on the fallpipe
$F_{B,ROV}$	[N]	Buoyancy force on the ROV
$F_{D,fp}$	[N]	Drag force on the fallpipe
$F_{D,ROV}$	[N]	Drag force on the ROV
f	[rad/s]	Coriolis parameter
f_0	[Hz]	Eigenfrequency of the fallpipe
f_i	[rad/s]	Frequency of component i of the signal
G	[Nm^2/kg]	Universal gravitational constant = $6.6 \cdot 10^{-11}$
g	[m/s^2]	Gravitational constant on Earth = 9.81
h	[m]	Water depth
h_{ROV}	[m]	Height of the ROV
h_1	[m]	Water depth of the upper layer
h_2	[m]	Water depth of the lower layer
L_{fp}	[m]	Length of the fallpipe
M_m	[kg]	Mass of the Moon = $7.35 \cdot 10^{22}$
M_s	[kg]	Mass of the Sun = $1.99 \cdot 10^{30}$
m_{ROV}	[kg]	Mass of the ROV
$P_{ROV,h}$	[W]	Horizontal power of the ROV
Re_{fp}	[-]	Reynolds number of the fallpipe
Re_{ROV}	[-]	Reynolds number of the ROV
S	[PSU]	Salinity
T	[°C]	Sea water temperature
T_0	[s]	Eigenperiod of the fallpipe
t	[s]	Time of the recorded signal
u	[m/s]	Flow velocity

Symbol	[Units]	Description
u_{ROV}	[m/s]	Velocity of the ROV
u_{w}	[m/s]	Wind speed
$u_{\text{w,x}}$	[m/s]	Wind speed in x-direction
$u_{\text{w,y}}$	[m/s]	Wind speed in y-direction
u_1	[m/s]	Flow velocity in the upper layer
u_2	[m/s]	Flow velocity in the lower layer
Δu	[m/s]	Difference in velocity between the upper and lower layer
z	[m]	Depth

Greek symbols

Symbol	[Units]	Description
ϵ_ρ	[-]	Relative density difference
$\eta(t)$	[m/s]	Recorded velocity signal
ν	[m^2/s]	Kinematic viscosity = 10^{-6}
ν_{eddy}	[m^2/s]	Turbulent vertical eddy viscosity
ρ_{fp}	[kg/m^3]	Density of the fallpipe
ρ_{w}	[kg/m^3]	Density of water
$\rho_{\text{w,1}}$	[kg/m^3]	Density of water in the upper layer
$\rho_{\text{w,2}}$	[kg/m^3]	Density of water in the lower layer
ϕ	[°]	Latitude
Ω	[rad/s]	Rotation rate of the Earth = $7.2921 \cdot 10^{-5}$
ω_{inertial}	[cpd]	Frequency of inertial waves
ω_{shelf}	[cpd]	Frequency of shelf waves

Chapter 1

Introduction

This chapter provides an introduction to the performed study into the oceanic hydrodynamic phenomena around the Shetlands Islands where Subsea Rock Installation (SRI) activities take place on a regular basis. Firstly, background information on the topic of Subsea Rock Installation in general is given, together with specific characteristics of the Van Oord vessels and projects executed by the company. After that, in Section 1.2, the research objective and research questions are posed, followed by the methodology of the research (Section 1.3) and an outline of the report, in Section 1.4.

1.1. Background information

As long as people live, rock is used to build and construct different aspects of structures, such as a bed protection of dikes or scour holes. The method used for the construction of bed protections is called stone dumping and takes place above water or in shallow water. This is realised by means of a side stone dumping vessel, which has a flat deck for the storage of the stones, and a limited placing accuracy (IADC, 2012). During the past couple of decades, a new type of stone dumping, called Subsea Rock Installation, evolved. This was a natural evolution as more and more activities take place in deeper water, around explored gas and oil fields. To be able to work at greater depths, where rocks are placed on top of pipelines or as a foundation of offshore structures, a larger placement accuracy is required (IADC, 2012). This is realised by the design and construction of a fallpipe at the bottom of the vessels, see Figure 1.1. The figure illustrates how an SRI vessel of Van Oord Dredging and Marine Contractors covers a pipeline at the bottom of the ocean.

At the lower end of the fallpipe, a so-called Remotely Operated Vehicle (ROV) is attached, which is equipped with devices that determine the position of the ROV in relation to the pipeline, for example. However, the speed and location of the ROV depend on the position and pace of the vessel, as the ROV cannot move independently. In the first designs, the fallpipe was rigid as a whole, but nowadays flexible fallpipes are available for SRI vessels. A cross section of the flexible fallpipe, which is connected to the vessels owned by Van Oord, is depicted in Figure 1.2. The 'pipe' consists of a sequence of buckets, which are made of synthetic material or steel and have a length of approximately two meters (Van Oord, 2015). More details regarding the characteristics of the SRI vessels owned by Van Oord can be found in Appendix A.

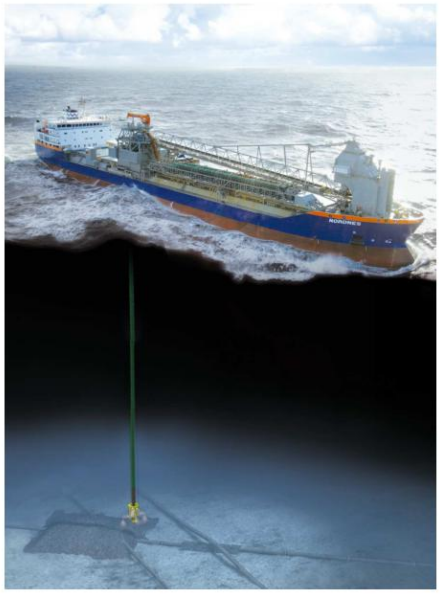

Figure 1.1: Van Oord's SRI vessel Nordnes covers a pipeline (Van Oord, 2016).

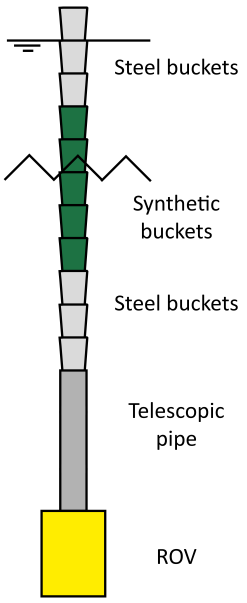

Figure 1.2: Cross section of the composition of the flexible fallpipe system, adapted from Ravelli (2012). Figure not drawn to scale.

A significant part of the SRI activities take place in the vicinity of gas and oil fields, as pipelines and cables are an essential part of the transport of these fossil fuels. At the west side of the Shetland Islands, multiple fields are located that form an important fuel source for the United Kingdom these days, see Figure 1.3. According to Kinect (2017), the two newest gas fields (Edradour and Glenlivet) will provide approximately 1.9 million barrels of gas and oil equivalent in 2018. The fuels from the subsea wells are transported to the mainland of the United Kingdom via the Shetland Gas Plant, see Figure 1.3.

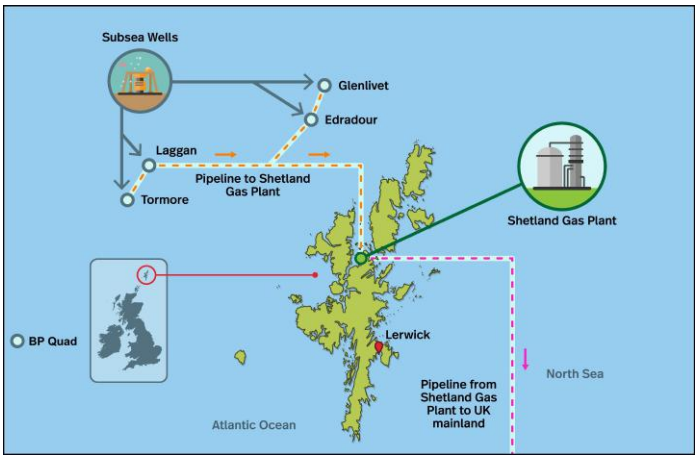

Figure 1.3: Overview of the gas and oil fields (Tormore, Laggan, Edradour, Glenlivet and BP Quad) around the Shetland Islands and their connection to the mainland, adapted from (Kinect, 2017).

During activities around the gas and oil fields west of the Shetland Islands, the SRI vessels are exposed to all kinds of weather and flow conditions. Both the weather and the flow conditions in the ocean are closely watched to prevent accidents with the equipment or personnel. Sometimes the conditions are unfavourable and the work has to be interrupted for a certain (short) period. Such an interruption can be caused by a strong flow near the bed, for example. This flow negatively influences the working conditions, as the fallpipe and the ROV cannot hold their dynamic position without risking a pop-out of one of the buckets. An exaggerated example of the different conditions is depicted in Figure 1.4, in which a distinction is made between the 'normal' and 'adverse' conditions.

Under normal conditions, the vertical distance between the ROV and the pipeline is approximately equal to five meters. This distance is chosen to prevent the ROV from bouncing into the bed. For average flow velocities the length of the fallpipe can be adjusted in order to remain the same vertical space between the ROV and the pipeline. However, as the flow gets stronger, it is more difficult to keep the ROV at its correct dynamic position. In practice, the following yields as a rule of thumb: the horizontal distance between the ROV and the pipeline should not be larger than 10% of the water depth. If the distance exceeds this value, the activities should be interrupted and one should wait for calmer conditions to resume the installation of the rocks. Recently, the 10% horizontal deviation rule has been incorporated in the automatic operating system of the ROV and the operator receives an automatic warning in case this fixed distance is exceeded. Appendix B contains graphs of the theoretical deviation of the ROV for different depth and flow velocity combinations, based on a simplified relation between the forces exerted on an SRI vessel.

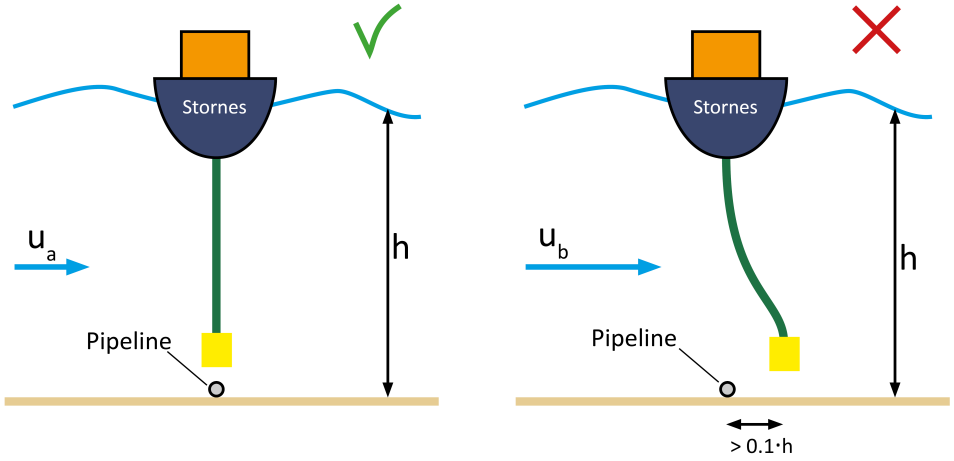

(a) 'Normal' conditions (b) 'Adverse' conditions

Figure 1.4: Schematic overview of the conditions (a) 'normal' and (b) 'adverse') that can occur during the activities of the SRI vessels, in this case the Stornes. u is the flow velocity ($u_b > u_a$) and h represents the water depth. Figure not drawn to scale.

The fallpipe vessels of Van Oord performed SRI activities around the Shetland Islands in 2014, 2015, 2016 and 2017 for five different projects (Solan, BP Quad, Edradour, Laggan and BP West). During two of the five projects, adverse flow conditions occurred, which caused a significant disruption of the activities. The other major cause of delays during these projects is a bad weather condition. The percentual contribution of both aspects is visualised in Figure 1.5. In these charts, the dark blue parts indicate activities, such as loading, sailing to the project site or quarry, working, survey checking or a change of the crew.

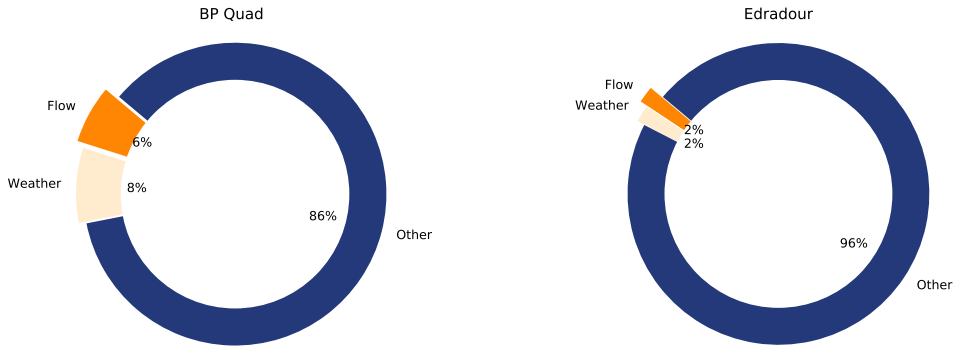

(a) BP Quad (b) Edradour

Figure 1.5: Charts that depicts the percentual contributions of the delay due to adverse flow conditions or bad weather conditions during (a) the BP Quad project and (b) the Edradour project, both executed by Van Oord. The location of these projects is depicted in Figure 1.3.

Figure 1.5 shows that for both the BP Quad and the Edradour project, the activities were interrupted due to adverse flow conditions for 6% and 2% of the total amount of elapsed working hours. These percentages are significant and caused a loss of several 100 k€ for each project.

In 2016, Les and Laukens predicted the magnitude of the flow for a specific project of Van Oord by means of a large scale ocean model. The details of this study are described in Chapter 2. The average predicted flow velocity was 0.15 m/s, which is theoretically below the workable limit of the vessels of Van Oord. However, during the project it turned out that the magnitude of the flow was significantly larger and therefore these predictions were not considered to be useful for Van Oord. This discrepancy was the reason to start this research.

1.2. Research objective and research questions

In the future, Van Oord wants to continue her SRI activities in the area around the Shetland Islands. Ideally, Van Oord wants to be able to prevent unforeseen downtime due to unfavourable metocean conditions. This requires more insight in the prevailing hydrodynamic conditions in the Shetland area, as at this moment these conditions are the assigned cause of the downtime. Therefore the following research objective for this study is formulated:

Understanding of the oceanic hydrodynamic processes in the North Atlantic Ocean west of the Shetland Islands.

To be able to achieve this objective a main research question and four sub-questions are posed below. The sub-questions are specific and contribute to the more general main question.

Main question

What are the characteristics of the oceanic hydrodynamic processes around the Shetland Islands that affect the workability of the SRI vessels?

Sub-questions

- What are the important hydrodynamic processes in the area around the Shetland Islands, that *might* contribute to the presence of non-working intervals?
- Which available hydrodynamic model is the most suitable for the representation of the oceanic conditions around the Shetland Islands?
- Which patterns, in relation to the non-working intervals, can be identified in the model output of the hydrodynamic model?
- Which patterns, in relation to the non-working intervals, can be identified in the historical logged data of the SRI vessels?

1.3. Methodology

The steps listed below are taken to answer the main research question and the sub-questions.

- The hydrodynamic processes that *might* contribute to the non-working conditions are identified based on literature research.
- The most suitable hydrodynamic model is selected from a broad range of available global and regional models. This model is used as a source of hydrodynamic data around the Shetland Islands.
- The hydrodynamic data is analysed and compared to identify possible patterns in depth, location, strength and direction and correlations with other variables.
- The available data from the SRI vessels of Van Oord is analysed to get more insight into the conditions during working and non-working intervals.
- The contributions of the hydrodynamic processes is explained based on the analysis of the hydrodynamic data and the SRI vessel data.

1.4. Outline of the report

Figure 1.6 provides an overview of the outline of this report. The problem description and the research set-up are discussed above, whereas in Chapter 2 a review of the relevant literature is given. Subsequently, in Chapter 3, the output from the hydrodynamic model is validated. Chapter 4 describes the method of combining the different data types for the identification of patterns and poses a couple of conclusions and hypotheses. Chapters 5 and 6 contain short analyses which assess these hypotheses. A discussion on certain aspects of this research is included in Chapter 7. Finally, the conclusions and recommendations for further research are posed in Chapter 8. The appendices (A, B, C, D, E, F and G) are attached behind the bibliography and contain background information and additional plots and figures.

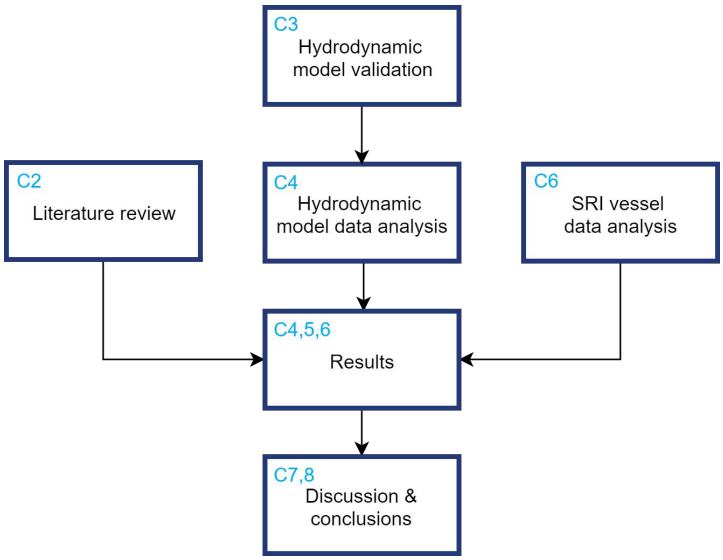

Figure 1.6: Outline of the report of this study.

Chapter 2

Review of literature and previous studies

As the cause of the interruption of the working activities of the SRI vessels around the Shetland Islands is still unknown, the main goal of the literature study is to investigate the potentially relevant processes. Therefore, this chapter contains information regarding different hydrodynamic phenomena, such as tides, large-scale ocean flows, internal and external waves and local flow patterns. It is self-evident that the information described is all applicable to the situation around the Shetland Islands. The landscape and environment at the mainland of the Shetland Islands are not considered to be relevant for this study.

Before the hydrodynamic processes are explained, two more general topics are discussed. Section 2.1 elaborates on the characteristic aspects of the North Sea. The Shetland Islands are located on the continental shelf approximately 125 kilometers from the continental slope, this topography might have an influence on the flow conditions in that area. Therefore, the characteristics of the shelf edge and its surroundings are described in Section 2.2. The order of discussion of the hydrodynamic processes listed above, is determined based on the scale of the phenomenon. First, the large-scale phenomena (ocean flows and tides) are described in Section 2.3 and after that, in Section 2.4, the small-scale aspects (waves and local flow patterns) are examined. The last section of this chapter summarises the previous performed studies into the hydrodynamic conditions around the Shetland Islands.

2.1. North Sea characteristics

The North Sea is a shallow sea, situated on the Northwest European shelf, that is part of the North Atlanctic Ocean. This body of water has a length of approximately 500 kilometers in the east-west direction and about 900 kilometers in the north-south direction (Quante and Colijn, 2016). The area of the North Sea roughly stretches from 5°W to 10°E and from 50°N to 62°N and is surrounded by Norway, Denmark, Germany, the Netherlands, Belgium and the United Kingdom. The average depth in the sea is 100 meters and the deepest point, which has a depth of 700 meters, is located in the Skagerrak, which is part of the Norwegian Trench (Rodhe et al., 2004). A complete depth profile of the North Sea is depicted in Figure 2.1.

In this figure the Norwegian Trench can be identified on the left and next to the Fair Isles Channel, another deep area can be observed. The latter area represents the transition from the continental shelf via the continental slope to the Atlantic Ocean and will be described in more detail in Section 2.2. In one year the entire basin of the North Sea flushes, which means that the water, that is in the area at this moment, is replaced by 'new' water from outside the domain of the sea. This water originates from the North Atlantic Ocean and the rivers that discharge into the North Sea (Quante and Colijn, 2016). According to Rodhe et al. (2004), there are three ways for the ocean water to enter the North Sea basin: via the Norwegian Trench, just to the east of the Shetland Islands and through the gap between the Shetland Islands and the Orkneys called the Fair Isle Channel, see Figure 2.1.

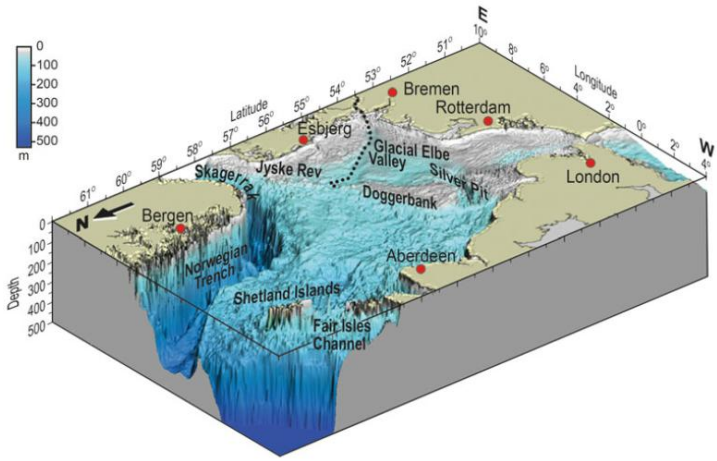

Figure 2.1: Bathymetry of the North Sea, adapted from Quante and Colijn (2016).

The two types of inflow (salt and fresh), in combination with the depth profile and tide in the North Sea, result in the presence of different physical processes (Rodhe et al., 2004). These processes are depicted in Figure 2.2. This figure gives a general overview of the three regions that can be identified based on the physical processes that occur in that specific area.

1. A deep, narrow trench where a baroclinic coastal current is prevailing;
2. A shallow part in the middle with seasonal stratification;
3. A part where the tide dominates.

The Shetland Islands are located in the second area, but their exact location is not incorporated in Figure 2.2. The specific details of all the phenomena in the different areas are described in Sections 2.3 and 2.4. However, the existence of these physical processes results in a spatial fluctuation of variables such as, temperature, salinity and wind. An overview of the mean values of the relevant variables is given in Table 2.1. In this table, a distinction is made between the North Sea in general and the area around the Shetland Islands.

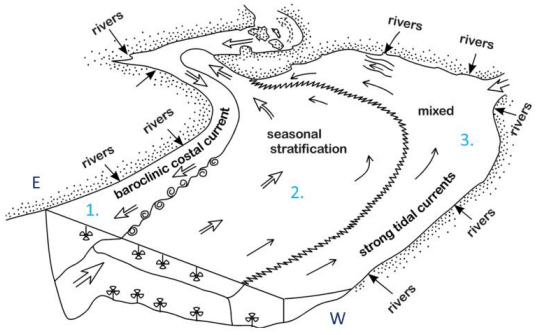

Figure 2.2: Overview of the physical processes that take place in the North Sea and their associated regions numbered from 1 to 3, adapted from Rodhe et al. (2004).

Table 2.1: Summary of the overall North Sea properties and their value around the Shetland Islands, based on Quante and Colijn (2016) and Rodhe et al. (2004).

Property	Unit	North Sea overall	Shetland Islands
Salinity	PSU	32-35	35
Sea Surface Temperature	°C	9.5-11.0	9.5
Wind	m/s	7.0-10.5	9.0
Geostrophic wind	m/s	10.0-11.5	11.5
Air temperature	°C	7	8
Air pressure	hPa	1008-1016	1008

The values in the table vary over the year due to different weather conditions, such as a fluctuating wind climate. Especially the sea surface temperature differs a lot in summer and winter: from north to south the temperature variation ranges with 3 to 7°C in the North Sea (Quante and Colijn, 2016). This variation, amongst other aspects, causes the presence of a seasonal thermocline of approximately 50 meters in the northern part of the North Sea. In the southern part of the sea, the depth profile remains more or less constant throughout the year.

2.2. The continental slope and shelf

As mentioned in the introduction of this chapter, the Shetland Islands are located on the continental shelf, which is situated on the Eurasian tectonic plate. The distance from the island group to the continental slope in the north west is approximately 125 kilometers, see Figure 2.3. Figure 2.4 depicts a general overview of the different parts of the underwater landscape in the ocean, including the continental shelf and slope. The situation in this figure is not identical to the situation around the Shetland Islands, although the structure of the different parts in relation to each other, is the same.

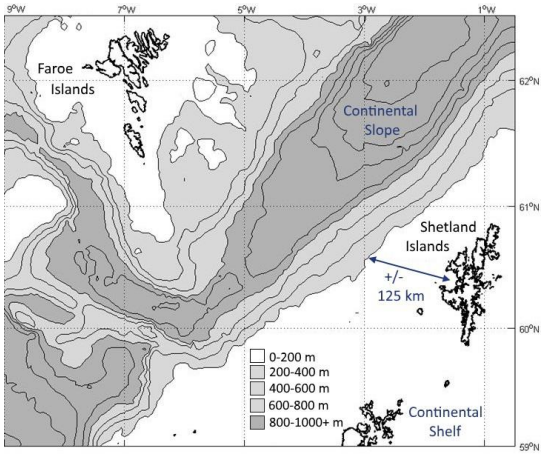

Figure 2.3: Location of the Shetland Islands on the continental shelf and the distance to the continental slope, adapted from Broadbridge and Toumi (2015).

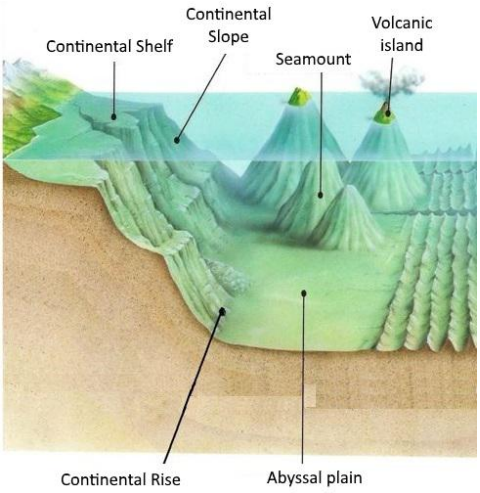

Figure 2.4: Overview of the different parts of the underwater landscape, adapted from Willis (2016).

According to Blaas and de Swart (2002), the typical difference in height between the continental shelf and the ocean floor (abyssal plain in Figure 2.4) on the European continental shelf is 3,800 meters over a stretch of 10,000 meters. The slope between these two levels is then equal to 38%, which is quite significant. The continental slope located closely to the Shetland Islands has a slightly smaller slope, as the vertical difference in height between the continental shelf and the ocean floor is smaller. The presence of a steep slope is accompanied by certain local flow patterns which are described in Section 2.4.

2.3. Large-scale hydrodynamic processes

This section describes the large-scale hydrodynamic processes in the surrounding area of the Shetland Islands. First the ocean gyres are discussed, followed by the tides and swell waves.

2.3.1. Ocean gyres

The global flow patterns, called gyres, which can be identified in the oceans on Earth exist because of two driving mechanisms: wind and sea water density. Both mechanisms interact with each other and are explained below, starting with the behaviour of the wind. The wind dominates the surface currents as the patterns, in which these gyres propagate, are similar to the global patterns of the wind. These global wind patterns can be explained by the existence of the Hadley Circulation (Pietrzak, 2014). This circulation is based on the varying amount of solar insolation on Earth. Areas close to the equator receive a relatively large amount of solar energy compared to the areas located at higher latitudes. This results in an upward flow of air around the equator, which is subsequently directed to the poles, where it cools down and returns to the equator completing the circle. According to Pietrzak (2014), in total six of those convection cells are observable on Earth, divided over two hemispheres: the Hadley cell, the Ferrel cell and the Polar cell, see Figure 2.5. The global winds originally have the same direction as the bottom parts of these cells, but these winds are deflected to the right or left by Coriolis, depending on the location on Earth. The surface flows in the ocean basins follow the deflected direction of the winds, see Figure 2.6.

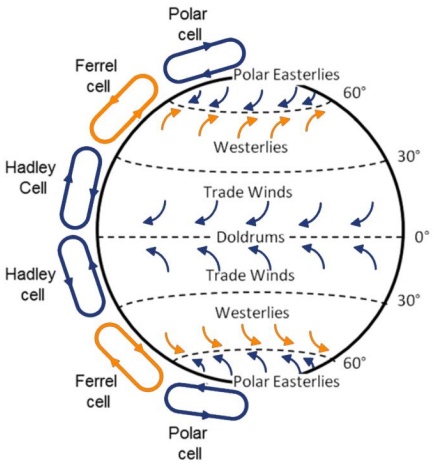

Figure 2.5: Schematic overview of the three convection cells: the Polar Cell, the Ferrel Cell and the Hadley Cell, adapted from Pietrzak (2014).

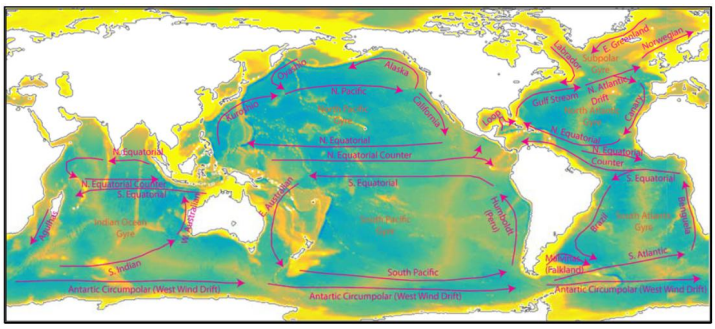

Figure 2.6: Main ocean surface gyres based on wind patterns (Pietrzak, 2014).

The second phenomenon that induces large-scale ocean gyres is the variation of the sea water density. The density varies with latitude and also with depth, as deep water from the poles is colder than surface water from the Mediterranean Sea, for example. However, the salinity of the latter water mass is much higher than the salinity of water originating from the north, resulting in water masses with different densities. A natural consequence of density differences is a pressure gradient, which causes baroclinic flows (Pietrzak, 2014). These flows are components of the thermohaline circulation, which is a contraction of the words thermo (temperature) and haline (salinity). In fact, this means that a volume of water with a high salinity (low temperature) flows under water mass with a low salinity (high temperature). A common name for the interaction of all these flows is the 'ocean conveyor belt' (Pietrzak, 2014). A small part of this belt is depicted in Figure 2.7a and an enlargement of the area around the Shetland Islands is presented in Figure 2.7b. The gyres that can be observed in this image are described in more detail in the next paragraph.

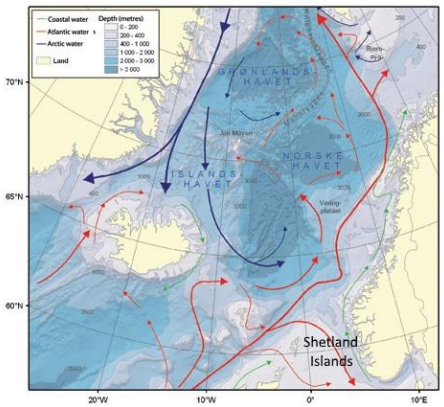

(a) Norwegian Sea

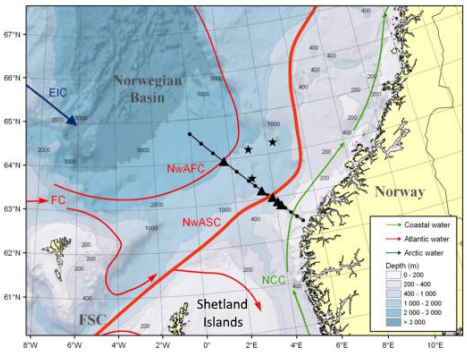

(b) Around the Shetland Islands

Figure 2.7: Overview of the ocean gyres (a) in the Norwegian Sea and (b) in the nearby surroundings of the Shetland Islands, adapted from Mork and Skagseth (2010).

Gyres around the Shetlands

The two currents that are noticeable in the surroundings of the Shetland Islands are the Norwegian Atlantic Current (NAC) and the Faroe Bank Channel Overflow (FBCO), see Figure 2.8, where the blue lines represent the FBCO. Both flows contribute to the North Atlantic Oscillation, which is part of the thermohaline circulation. However, the currents have an opposing flow direction and different characteristics, which are summarised in Table 2.2. The FBCO current is one of the three branches of the Iceland Scotland Overflow Water (ISOW) and the properties listed in the table are in line with the values described by Zou et al. (2017).

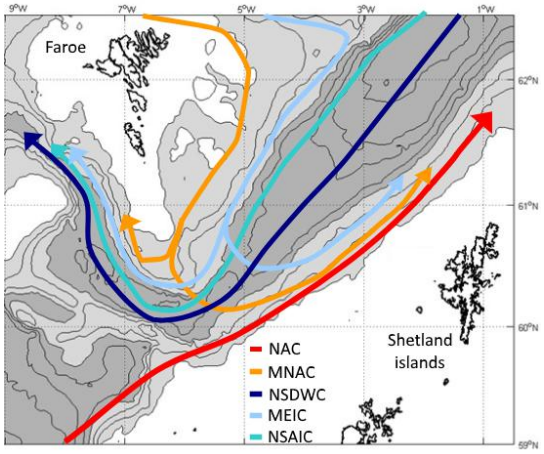

Figure 2.8: Detailed overview of the patterns of the gyres around the Shetland Islands, adapted from Berx et al. (2013). The meaning of the abbreviations is as follows: NAC: North Atlantic Current, MNAC: Modified North Atlantic Current, NSDWC: Norwegian Sea Deep Water Current, MEIC: Modified East Icelandic Current and NSAIC: Norwegian Sea Arctic Intermediate Current.

Table 2.2: Summary of the characteristics of the gyres around the Shetland Islands (NAC and FBCO), based on Mork and Skagseth (2010), Andersson et al. (2011) and Hansen and Østerhus (2007).

Characteristic	Unit	NAC	FBCO
Volume flux	Sv	5.1 ± 0.3	2.1 ± 0.3
Flux variability	%	20	10
Temperature	°C	7.1	3.0
Salinity	PSU	35.2	27.9
Density	kg/m^3	27.8	35

2.3.2. North Sea tide

The general aspects of the tide, described in Appendix C, in combination with a specific geographic location result in a unique tidal climate. Each climate has its own tidal range and tidal constituents, for example. The North Sea basin has a specific geometry inducing resonance in the semi-diurnal spectral range (Quante and Colijn, 2016). Two dominant tidal components are the M_2 and the S_2 constituents, which have both a significant difference in amplitude between spring and neap tide. Quante and Colijn (2016) list a few statistics of the North Sea: the tidal range is 1.40 meters, which can be enforced during spring tide. Moreover, the tidal range around the Shetland Islands, measured at Lerwick, is almost 2.5 meters. At last, the speed of the tidal currents in the North Sea is approximately equal to ten or twenty centimeters per second. Figure 2.9 depicts the characteristics of the tide in the entire basin. Three amphidromic points can be identified: (1) near the entry of the Southern Bight, (2) at the eastern tip of the Dogger Bank and (3) at the southern tip of Norway (Otto et al., 1990).

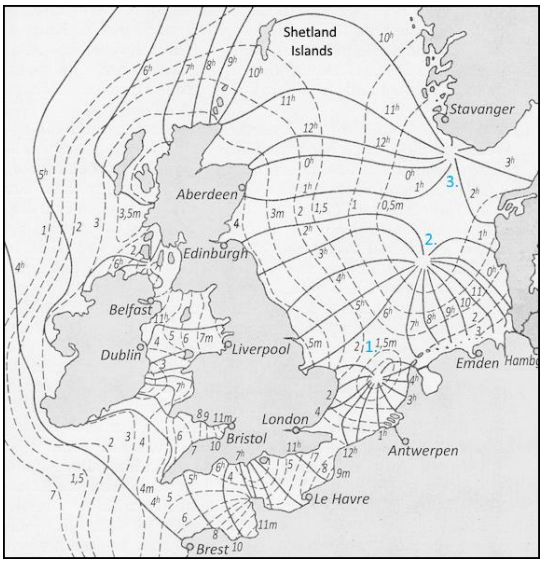

Figure 2.9: Co-tidal lines (hours) and co-range lines (amplitudes in m) of the M_2 and the S_2 tide in the North Sea and the three amphidromic points, depicted in cyan, adapted from Sager (1959).

Internal tide around the Shetland Islands

According to Sherwin (1991), the Wyville-Thomson ridge, which reaches until 500 meters from the sea surface, generates an internal tide resulting in large internal waves in the Faroe-Shetland Channel. This evidence is based on observations obtained from a downward-looking Acoustic Doppler Current Profiler (ADCP). There are two requirements for the generation of an internal tide: the presence of a pronounced sloping topography and a vertically stratified water column (Sherwin, 1991). Both of these aspects are observed around the Shetland Islands, as the continental shelf edge is located nearby and cold (warm) water flows in from the north (south). The local slope in the topography of the sea floor determines the propagation direction of the internal waves. A distinction is made between a 'sub-critical' and a 'super-critical' slope. Sherwin (1991) states that a modal analysis of the ADCP output at Station M6, see Figure 2.10, indicates the appearance of six different modes with different wave lengths. Another appearing feature is the observation of an internal wave with an M_2 amplitude of 37 meters at a depth of almost 600 meters (Sherwin, 1991). Therefore, the internal tide around the Shetland Islands is assumed to have the frequency of the dominant tidal constituent, which is M_2.

The article by Zhao (2017) describes the propagation velocity of the semi-diurnal internal tides at the Hawaiian Ridge in the North Pacific Ocean. An overview of the magnitude of these velocities can be found in Table 2.3. The magnitude of the internal tide around the Shetland Islands will not be identical to these numbers, as the stratification and inertial frequency differ for the Hawaiian Ridge and the Shetland Islands. However, the magnitudes provide a general indication of the influence of the internal tide on the flow conditions in the ocean.

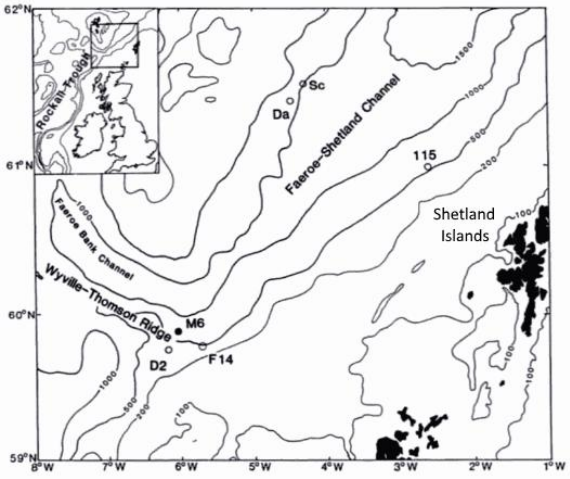

Figure 2.10: Indication of Station M6 between the Wyville-Thomson ridge and the Faroe-Shetland Channel, adapted from Sherwin (1991). The isolines represent the depth of the water column in meters.

Table 2.3: Mean propagation velocity of the semi-diurnal tidal constituents on the Hawaiian Ridge, adapted from Zhao (2017). The theoretical value per constituent is given in parentheses.

Constituent	Mean velocity [m/s]	Type
M_2	3.62 (3.55)	Phase
S_2	3.51 (3.45)	Phase
$M_2 + S_2$	1.87 (1.93)	Group

2.3.3. Swell waves

In general, two types of wave systems can be distinguished in a water body: swell generated by a storm and wind sea as a result of local gusts (Holthuijsen, 2007). Several days pass by between the generation of swell and the actual arrival at a certain location. According to Holthuijsen (2007), the waves usually have a long-crested character and a low frequency, around 0.1 Hz. It is possible that wind from the north in combination with a storm in the Norwegian Basin, see Figure 2.7b, results in persistent waves around the Shetland Islands. On board of the SRI vessel, the behaviour of the waves is monitored separately from the flow conditions. The sudden appearance of swell waves can potentially lead to an interruption of the working activities. This might be caused by the effect of the swell wave on the movement of the vessel-fallpipe combination as a whole.

2.4. Small-scale hydrodynamic phenomena

The phenomena described in this section occur on a slightly smaller scale and are therefore considered to be more local than the tide, for example. However, the exact location where the effects of these phenomena are observed is varying over time. First, the general characteristics of internal and external waves are described,

and subsequently shelf waves are discussed. At last, a list of specific flow patterns or combinations of patterns is given. The phenomena are quite arbitrary, but these processes might possibly be the cause of the interruption of the working activities around the Shetland Islands and are therefore considered relevant for this study.

2.4.1. Internal and external waves

Internal and external waves occur if two water masses with a different density interact, or in case water flows over a topographic feature (Pietrzak, 2015). An example of a topographic feature is the Camarinal Sill, which is a shallow ridge, in the strait of Gibraltar between Spain and Morocco. Due to the density differences or a topographic feature, the free water surface and the interface between the two layers of water move up or down, see Figure 2.11. In case of external waves, both the free surface and the interface move in the same direction (up or down), whereas for internal waves, these motions are opposed. The waves are analysed by means of the method of characteristics, which shows that the external phase velocity is one order of magnitude larger than the internal phase velocity (Pietrzak, 2015). The equations for the external and internal phase velocity are given in Appendix C.

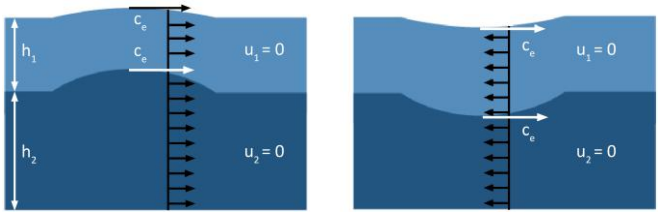

(a) External waves

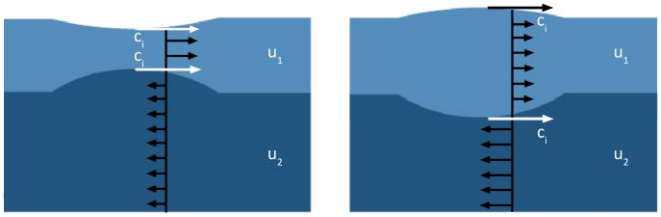

(b) Internal waves

Figure 2.11: Properties of (a) external waves and (b) internal waves, adapted from Pietrzak (2015).

Waves around the Shetland Islands

The type of waves discussed above could also occur in the surrounding area of the Shetland Islands. This might be caused by density differences in the water in that area. Another cause of the formation of internal waves is described by Qian et al. (2010). Their study involves the numerical modelling of a barotropic tidal flow over a steep two-dimensional ridge with a strong upper-ocean stratification. The results of this modelling process show that part of the energy from the barotropic tide is transferred to a baroclinic wave, which is a type of internal wave. This can only occur when the ratio of the maximum ridge slope to the maximum wave slope is lager than 1 (Qian et al., 2010). As the Shetland Islands are located relatively close to the continental slope, the effect of this interaction might be observed in the vicinity of the islands.

2.4.2. Inertial waves

A special type of internal waves are the inertial waves, which propagate only in the interior of a fluid. These waves can be observed in every body of water on the planet since the waves are initiated by the rotation of the Earth. According to Fu (1980), the frequency of the inertial waves is given by Equation 2.1, as their restoring force is the Coriolis force. For the area around the Shetland Islands, the Coriolis parameter is approximately equal to $1.263 \cdot 10^{-4}$ rad/s, resulting in a inertial wave frequency (ω_{inertial}) of 1.73 cycles per day (cpd).

$$\omega_{\text{inertial}} = \frac{f \cdot 24 \cdot 3600}{2 \cdot \pi} \tag{2.1}$$

$$f = 2\Omega \cdot \sin(\phi) \tag{2.2}$$

Where:	ω_{inertial}	[cpd]	Frequency of inertial waves
	f	[rad/s]	Coriolis parameter
	Ω	[rad/s]	Rotation rate of the Earth = $7.2921 \cdot 10^{-5}$
	ϕ	[°]	Latitude

García Lafuente and Lucaya (1994) researched the inertial waves in the Ibiza Channel, located in the Mediterranean Sea. Their two major findings might be relevant for the situation around the Shetland Islands. In the channel, a correlation has been found between the presence of an atmospheric front and the appearance of inertial waves, moving with a velocity equal to a couple of meters per day. From this can be concluded that the weather can be a generating force for these types of waves, as well as the rotation of the Earth (García Lafuente and Lucaya, 1994). Furthermore, García Lafuente and Lucaya (1994) state that a high value of the Richardson number (> 1/4) throughout the water column, accommodated the decay of the waves. In that way, the waves are prevented from travelling larger distances through the water body.

2.4.3. Shelf waves

As mentioned before in Section 2.2, the presence of a shelf edge might induce additional hydrodynamic processes. One of these processes is the continental shelf wave, see Figure 2.12. In principle, these waves are similar to Kelvin waves, which propagate in one direction, parallel to the coast (Cutchin and Smith, 1973). The wave can move along a sloping bottom via a process described by Longuet-Higgins (1968): the water particles that are displaced downward on the slope, acquire positive relative vorticity, whereas the upward moving particles have negative vorticity. These changes in vorticity are caused by atmospheric disturbances according to Gill and Schumann (1974). The frequency of a shelf wave is five times smaller than the inertial frequency, see Equation 2.3 by Schulz et al. (2012). Since the Shetland Islands are located close to the continental shelf, shelf waves might occur in this area. The waves will have a frequency of approximately 0.35 cycles per day.

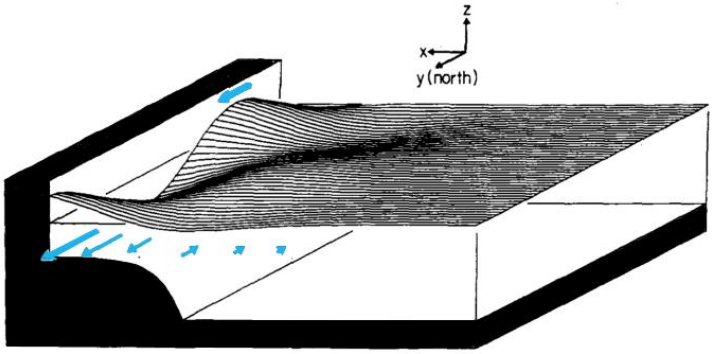

Figure 2.12: An exaggerated example of a continental shelf wave propagating to the north, adapted from Cutchin and Smith (1973).

$$\omega_{\text{shelf}} = \frac{0.2 \cdot f \cdot 24 \cdot 3600}{2 \cdot \pi} \tag{2.3}$$

Where: ω_{shelf} [cpd] Frequency of shelf waves

2.4.4. Local flow patterns

This section summarises three articles about specific flow patterns, which are tidal mixing in the North Sea, seasonal circulation on the continental shelf and residual circulation over the continental slope. These processes might occur in the surrounding area of the Shetland Islands.

Tidal mixing in the North Sea

As discussed in Section 2.3, the tide in the North Sea is semi-diurnal and has a significant tidal range. Due to the inflow of water, originating from different parts of the world, the density of the North Sea is not uniform. The major part of the basin is stratified during normal conditions. However, according to Kleptsova (2013), tidal mixing takes place in certain regions of the North Sea during spring and neap tide, see Figure 2.13. Just

below the Shetland Islands, a significant part of the sea is mixed during spring tide and a slightly smaller part during neap tide. In general, tidal mixing causes density driven flows, which might have an influence on the ocean conditions at the south west of the Shetland Islands.

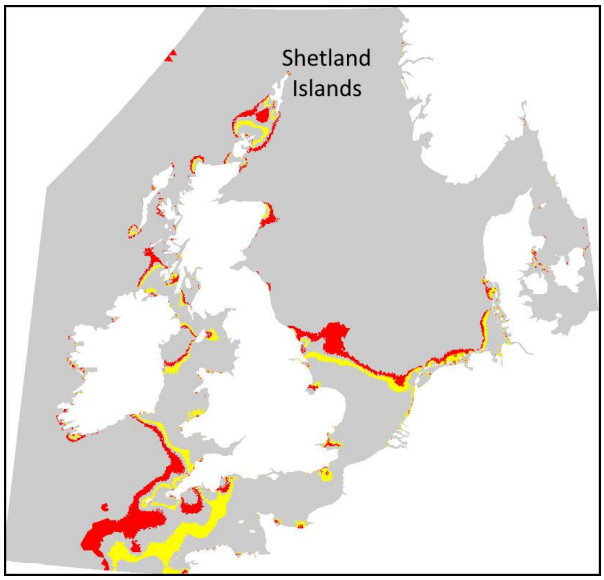

Figure 2.13: Predicted position of tidal mixing fronts at spring (red) and neap tide (yellow) in the North Sea, adapted from Kleptsova (2013).

Seasonal circulation on the continental shelf

Holt and Proctor (2008) conducted a numerical study into the currents on the Northwest European Shelf, in the North Sea. The goal of this study was to gain more insight into the varying contribution of three different types of components to the flow in this area. These three types are wind, density and oceanic-driven components. Their contribution was assessed by three model experiments with different settings: one fully baroclinic, one fully barotropic and one baroptropic model with tidal and oceanic forcing. It turned out that all components are observed year-round, but the density-driven component is especially important in the autumn and summer (Holt and Proctor, 2008). In general, the highest flow velocities are found in the Norwegian Trench, around Ireland and between the Orkney Islands and the mainland of Scotland.

Residual circulation over the continental slope

Blaas and de Swart (2002) and Csanady (1988) both researched the (residual) currents on the continental slope. However, both applied a different approach and their conclusions regard different aspects of the slope. On the one hand, Blaas and de Swart (2002) made an hydrodynamic numerical model of the European shelf and calibrated it on measurements from two locations nearby the slope, the Bay of Biscay and the Hebrides. Based on the interpretation of the model results at both locations, it can be concluded that the slope current and the cross-shelf circulation linked to that current, mainly depend on the flow and shelf characteristics. A different effect dominates in the Bay of Biscay and in the Hebrides, even though both places are located on the same shelf edge. In the Bay of Biscay, the tidal and density effects are of the same order of magnitude, whereas in Hebrides the density effects dominate, resulting in a different interaction current (Blaas and de Swart, 2002). Moreover, the model proved that the solution of the interaction current from a depth-averaged model significantly differs from the depth-average values of the interaction current itself. Both conclusions might be relevant for the the prevailing conditions around the Shetland Islands.

Csanady (1988) on the other hand, states that the major part of the ocean flows are affected by the presence of the continental slopes, as 12% of the ocean's surface is covered by this topographic feature. This results in large-scale physical processes that take place on the continental slope, or in the nearby surroundings. An example of such a process is depicted in Figure 2.14, where an eddy occurs due to the upwelling process over the continental slope in the direction of the shelf. These processes might also take place at the shelf edge close to the Shetland Islands.

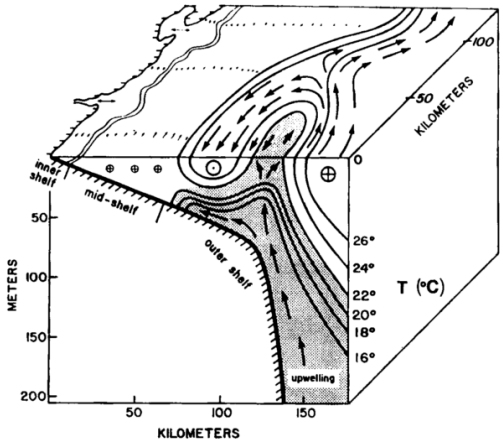

Figure 2.14: Schematic visualisation of a frontal eddy that is partly located at the shelf edge and partly at the slope (Csanady, 1988). The eddy is caused by the differences in temperature over depth.

2.5. Previous research

In the past, two types of research are executed that are relevant for this study into the prevailing oceanic conditions around the Shetlands. The first type, which was already mentioned in Chapter 1, is a project-specific prediction of the strength of the flow in July 2016. These predictions were based on the HYbrid Coordinate Ocean Model (HYCOM) of the National Oceanic and Atmospheric Administration (NOAA) (Les and Laukens, 2016). The surface current velocity and direction, the temperature and salinity and the sea surface level were predicted on a time interval of one hour. However, the predictions of the model did not coincide with the observed velocities at the location of the project. The predictions underestimated the actual flow velocities, which caused a significant delay in the SRI activities around the Shetland Islands.

The other research regards a prediction of the wave and flow climate for the planned construction of a cable route around the Orkney Islands by Kroon et al. (2013). These islands are located just south of the Shetland Islands and therefore this study can be seen as a reference case for the study into the hydrodynamic processes around the Shetland Islands. The flow patterns around the Orkney Islands were predicted by a depth-averaged, 2D model of the European continental shelf, which was validated by means of flow velocity measurements in the Pentland Firth (the gap between the mainland of Scotland and the Orkneys), see Figure 2.15. At that same location, the forecasted flow velocities were significant, in the order of 0.8 to 1.3 m/s. In the remaining part of the area, which mainly consists of open sea, the predicted velocities were a bit lower, in the range of 0.3 to 0.6 m/s. However, the model is 2D and does not include all physical processes in the area.

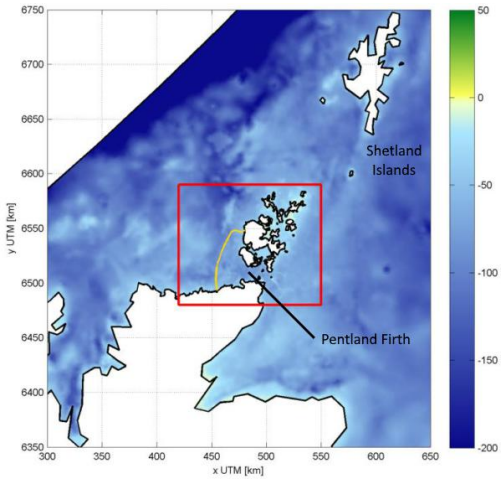

Figure 2.15: Overview of the European Continental Shelf Model area of the Orkney Islands, adapted from Kroon et al. (2013). The yellow line indicates the location of the cable route.

Chapter 3

Validation of the 3D DCSM-FM output

In order to gain more insight in the hydrodynamic conditions, which have an influence on the working conditions around the Shetland Islands, the available data is screened, combined and compared. The following three types of data, from different sources, are analysed:

- Daily Progress Reports (DPR) of the activities executed by the SRI vessels of Van Oord (Stornes and Nordnes);
- Data from the Automatic Identification System (AIS), which tracks current and historical positions of vessels all over the world;
- Output data from the 3D Dutch Continental Shelf Model (3D DCSM-FM), which is a 3D hydrodynamic model of the Northwest European Shelf and the North Sea created by Zijl et al. (2016). Appendix D contains a detailed description of the characteristics of this model, including the model and user artifacts and the details of the dataset.

The first two types of data are analysed to select the most suitable time ranges of the projects, executed by Van Oord in the past few years. This process is described in Section 3.1. In Section 3.2, the validity of the output of different variables from the 3D DCSM-FM is assessed by comparing it to data or measurements from other sources.

3.1. 3D DCSM-FM output selection

A DPR is a description of the different activities that are performed on an SRI vessel during the 24 hours of a day. These activities are logged on a five minute interval and consist, amongst others, of loading, sailing, surveying and installing. The delays that occur due to adverse weather and flow conditions or traffic are also written down in these reports. However, the position of the vessel cannot be retrieved from the DPRs and is therefore obtained from the AIS. By combining the information of these two sources, a selection of suitable time ranges is made. In this case, suitable means that a non-working interval due to adverse flow conditions is logged in the DPR and the data of the vessel position is available.

To be able to properly assess these time ranges, which are part of one of the five finalised projects, mentioned in Chapter 1, a code is assigned to each track individually. One track consists of a number of subsequent days that one of the SRI vessels was working on a project in the area around the Shetland Islands. The overviews of these codes, consisting of one letter (S for Stornes and N for Nordnes) and one number, can be found in Tables 3.1 and 3.2. The tables show the project name, the start date and the end date for each track. The table also indicates whether or not a non-working interval due to adverse flow conditions occurred in this time range and provide a range of dates for which AIS data is available. In general, the AIS data does not cover a full track of a vessel and for one track of both the Stornes and the Nordnes (S2 and N2) all AIS data is missing. The presence of a 'y' and a date range in the last two columns indicates that the track is considered suitable for selection. From the Stornes eight tracks are selected (S4, $S6_1$, $S6_2$, S7, S8, S9, S10, S11) and from the Nordnes two tracks are chosen (N4 and N13). For plotting purposes in further analyses, the data range in the last column might deviate from the initial track range and the AIS data range.

Table 3.1: Characteristics of the vessel tracks of the Stornes from the projects executed by Van Oord in 2014, 2015 and 2016.

STORNES

Track code	Project name	Start date	End date	Non-working interval	AIS data range	Suitable	Plotting range
S1	Solan	25-11-2014	01-12-2014	no	27-11 to 30-11	no	-
S2	BP Quad	11-06-2014	17-06-2014	yes	-	no	-
S3	BP Quad	01-12-2014	07-12-2014	no	02-12 to 06-12	no	-
S4	BP Quad	26-12-2014	01-01-2015	yes	28-12 to 01-01	yes	29-12 to 01-01
S5	Edradour	08-09-2015	20-09-2015	no	09-09 to 19-09	no	-
$S6_1$	BP Quad	18-10-2015	23-10-2015	yes	20-10 to 23-10	yes	21-10 to 23-10
$S6_2$	BP Quad	24-10-2015	30-10-2015	yes	24-10 to 29-10	yes	24-10 to 29-10
S7	BP Quad	13-01-2016	21-01-2016	yes	14-01 to 21-01	yes	15-01 to 20-01
S8	Edradour	14-07-2016	27-07-2016	yes	17-07 to 26-07	yes	18-07 to 26-07
S9	Edradour	01-08-2016	17-08-2016	yes	02-08 to 17-08	yes	03-08 to 09-08
S10	Edradour	01-09-2016	03-10-2016	yes	03-09 to 03-10	yes	20-09 to 26-09
S11	Edradour	06-10-2016	10-10-2016	yes	07-10 to 10-10	yes	08-10 to 10-10
S12	Edradour	14-10-2016	18-10-2016	no	16-10 to 17-10	no	-

Table 3.2: Characteristics of the vessel tracks of the Nordnes from the projects executed by Van Oord in 2014, 2016 and 2017.

NORDNES

Track code	Project name	Start date	End date	Non-working interval	AIS data range	Suitable	Plotting range
N1	Laggan	06-08-2014	13-08-2014	no	10-08 to 13-08	no	-
N2	Laggan	08-09-2014	08-09-2014	no	-	no	-
N3	Laggan	12-09-2014	15-09-2014	no	13-09 to 15-09	no	-
N4	Edradour	25-07-2016	03-08-2016	yes	26-07 to 03-08	yes	28-07 to 03-08
N5	Edradour	16-08-2016	27-08-2016	no	17-08 to 26-08	no	-
N6	Edradour	04-09-2016	10-09-2016	no	05-09 to 10-09	no	-
N7	Edradour	15-09-2016	23-09-2016	no	17-09 to 22-09	no	-
N8	Edradour	16-11-2016	21-11-2016	no	18-11 to 20-11	no	-
N9	Edradour	09-04-2017	28-04-2017	yes	10-04 to 28-04	no	-
N10	Edradour	11-05-2017	19-05-2017	no	12-05 to 18-05	no	-
N11	Edradour	13-08-2017	23-08-2017	no	15-08 to 23-08	no	-
N12	Edradour	19-09-2017	25-09-2017	no	19-09 to 25-09	no	-
N13	BP West	02-10-2017	11-10-2017	yes	05-10 to 10-10	yes	05-10 to 10-10

3.2. 3D DCSM-FM output validation

The 3D DCSM-FM, which is based on three previous versions of the model, is originally developed for the assessment of the long-term water quality in the North Sea (Zijl and Veenstra, 2018). The model is quantitatively calibrated on the water level elevation, the sea water temperature and the sea water salinity from thirteen measurement stations along the Dutch coast (Zijl et al., 2016). However, the area around the Shetland Islands has not been validated yet, as measurements from this area are scarce. Therefore, in this section, the model output from the 3D DCSM-FM is compared to data from different sources. The validation is applied to the ten tracks, which were selected in Section 3.1. Section 3.2.1 contains a validation of the depth profile based on the SRI vessel data. In Section 3.2.2, the water level elevation is set side by side to the measurements from the tidal station in Lerwick (EMODnet, 2017). Subsequently, in Section 3.2.3, the density profile from the model is compared to data from the ocean model by CMEMS (2018). At last, in Section 3.2.4, the differences and similarities between the flow velocities from the 3D DCSM-FM and measurements by BODC (2018) are identified. These comparisons provide more insight in the credibility of the model results, presented in Chapter 4.

3.2.1. Depth profile

During the working activities of the SRI vessels, thousands of sensor signals are stored continuously. These signals are collected by the various types of measuring equipment on the vessel and on the ROV. The physical movements of both objects, such as rotation, roll and heave are important for the dynamic position of the vessel-fallpipe combination. The values of these variables are predicted based on the Inertial Navigation System (INS), which determines a new position based on the current rotation and acceleration of the ROV (Farrell and Barth, 1999). Other signals that are measured are, for example, the velocity and acceleration of the ROV and the distance to the sea bed.

The latter is used to verify the depth profile of the 3D DCSM-FM as it indicates whether or not the local depth boundary is correct, see Figure 3.1. In general, the depth profile of the 3D DCSM-FM is accurate as the distance between both lines is approximately ten meters, which is of the same order of magnitude as attempted five meters distance. However, at certain moments in time, for example around the beginning of July 29th, the blue line crosses the brown line, which is theoretically not possible. At those locations, the actual depth is larger than the current depth in the 3D DCSM-FM.

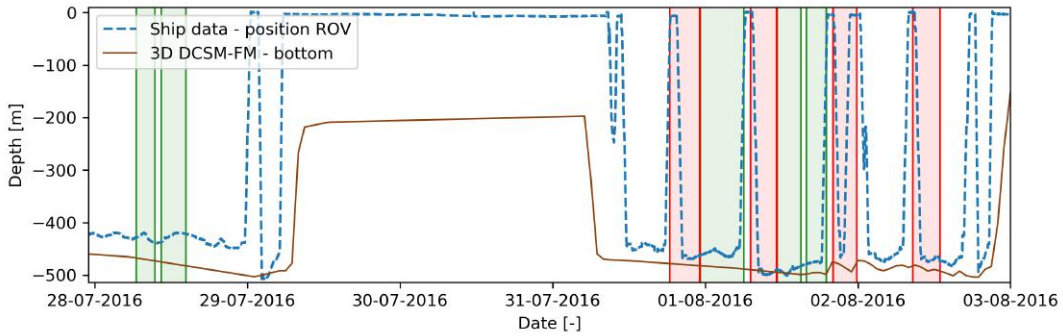

Figure 3.1: Plot of the location of the sea bed in the 3D DCSM-FM (brown) by Zijl et al. (2016) and the position of the ROV above the bed (blue) for Track N4. The green and red vertical lines represent the working and non-working intervals with a duration of at least 2% of the plotted time range.

In total, the depth profiles of the ten selected tracks contain eighteen non-working intervals, which have a duration of at least 2% of the plotted time range. During sixteen of these eighteen intervals, the ROV was deployed after the non-working interval has started. This can be observed in Figure 3.1, within the non-working interval that ends at the first of August. In case of the two remaining non-working intervals, the ROV was already launched into the water column. It was expected that during a non-working interval, the ROV would be positioned at the moonpool, as the conditions in the ocean are adverse at these moments in time. However, it turns out that in almost 90% of the cases the ROV has been launched during a non-working interval.

3.2.2. Water level elevation

The 3D DCSM-FM output of the water level elevation is compared to the measurements of the water level elevation from the tidal station at Lerwick (EMODnet, 2017). The 3D DCSM-FM provides model output at equally spaced stations, see Figure 3.2. This figure also indicates the location of Lerwick's tidal station (red dot) and the selected station from the 3D DCSM-FM (green dot), which is located nearest to Lerwick. The water level comparison is made for the time span of the same tracks, which were selected in Section 3.1. As the time ranges of these tracks vary between different years, this analysis provides an overview of the general behaviour of the water level over these years. The measurements of the tidal station at Lerwick are corrected in time to coincide with the results of the 3D DCSM-FM. The correction in time consists of an one hour shift to compensate for the time zone and the 'summer' months. Since the reference level of both sources differs, the long-term mean is subtracted from each dataset individually.

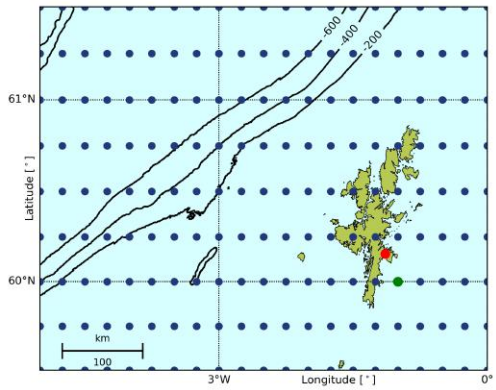

Figure 3.2: Overview of the locations of the output stations of the 3D DCSM-FM (Zijl et al., 2016) indicated by dark blue dots, the position of the tidal station at Lerwick in red and the selected station for the comparison in green.

Figure 3.3 contains part of the results of the comparison of the water level elevation of both sources. Track S8 is plotted in the upper part of the figure, whereas Track S7 can be found in the lower part of the figure. These tracks are chosen on purpose as the time ranges represent the general picture of the results. For a couple of tracks, for example S8, the pattern of the water level elevation is almost identical, see Figure 3.3a. The difference between the two lines over time as a percentage of the maximum amplitude is approximately 5% for this set of tracks. For the other tracks, the phases of both water level elevation patterns still coincide. However, the magnitude of the elevation is slightly different at certain moments in time. This can be seen in Figure 3.3b at times ranging from January 17th to January 21th. The overall difference between the values of both sources approximates to 10%. In short, from these results can be concluded that the deviation of the water level elevation in the 3D DCSM-FM is relatively small (5-10%). Therefore, it is assumed that the magnitude and phase of the water level elevation are represented well in the 3D DCSM-FM.

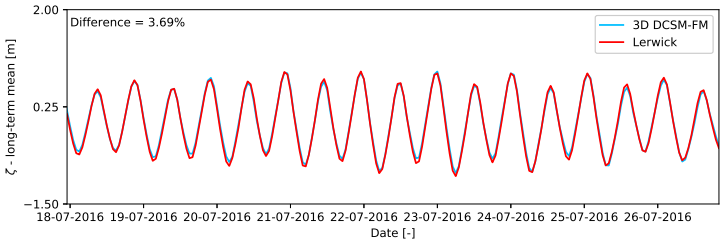

(a) Track S8

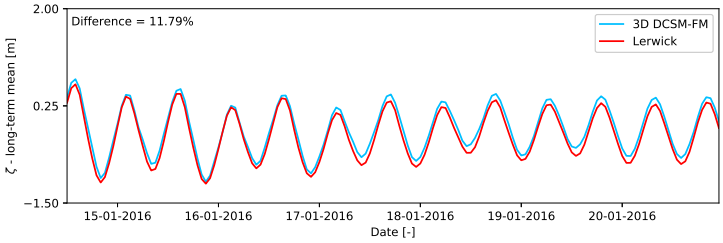

(b) Track S7

Figure 3.3: Plot of the water level elevation [m] minus the long-term mean from the 3D DCSM-FM by Zijl et al. (2016) in light blue and measurements from the tidal station at Lerwick on the Shetland Islands (EMODnet, 2017) in red for (a) Track S8 and (b) Track S7. The percentage plotted in the top left corner indicates the difference between both lines relative to the maximum amplitude.

3.2.3. Density profile

For the validation of the density profiles in the 3D DCSM-FM, the output is compared to data from an ocean model from Metoffice by CMEMS (2018) at both project locations, see Figure 3.4. The specific details of this ocean model can be found in Appendix D. The density is calculated from the sea water temperature and the salinity, as described in Appendix D, by means of an Equation of State. The ocean model generates output

averaged per day, which is significantly different to the interval of the 3D DCSM-FM, that provides output every hour. Moreover, the amount of layers in the model by CMEMS (2018) is smaller, 16 versus 20, and the layers are non-evenly spread over the water column. The resolution in the upper part is much higher as the first 100 meters of the water column is subdivided in eight layers.

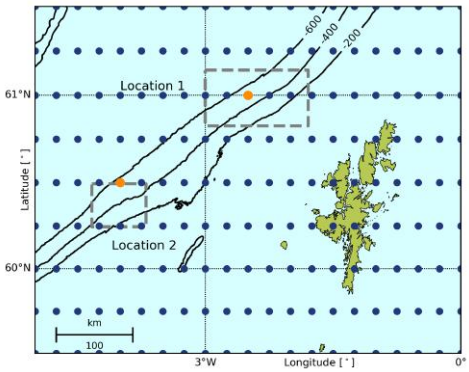

Figure 3.4: Overview of the locations of the output stations of 3D DCSM-FM (Zijl et al., 2016) indicated by dark blue dots and the selected stations for the comparison at Location 1 and Location 2 in orange. The grey-dotted squares indicate the project areas.

The density profiles at Location 1 for both models, plotted for one month and over a depth of 500 meters, are depicted in Figure 3.5. For a fair comparison, the colours of the plots have the same limits. However, the values of the 3D DCSM-FM lie in a higher range than the values of the ocean model by CMEMS (2018): 1027.6 to 1027.8 and 1027.0 to 1027.6, respectively. Due to the different output intervals, the colour plot of the latter model, see Figure 3.5b is less smooth than the plot of the 3D DCSM-FM. The yellow parts on top of the water column in this figure, which represent lighter water volumes, seem to appear four or five times a month. The second and the fourth time, the water is less dense than the other three times, see Figure 3.5b. The underlying phenomenon or process causing the presence of these lighter water masses remains unclear. Surface plots of the entire area around the Shetland Islands over a time range of one month, show volumes with a higher temperature/salinity that move slowly back and forth over the continental shelf. However, this does not explain the variations in the upper part of the water column, indicated in Figure 3.5b.

The plots of the temperature and the salinity, that are used to compute the density, can be found in Appendix F. The difference in density profiles can be explained by the varying temperature, as the temperature in the ocean model is four degrees Celsius higher than in the 3D DCSM-FM. A change in water density due to a decrease of 4 °C is equivalent to a change due to an increase of 1 PSU (Beer, 1997). Therefore, the density in the 3D DSCM-FM is higher than the density in the ocean model by CMEMS (2018). In short, it can be inferred that a the baroclinic processes are not represented correctly in the 3D DCSM-FM, as a comparison with the ocean model by CMEMS (2018) results in significant differences.

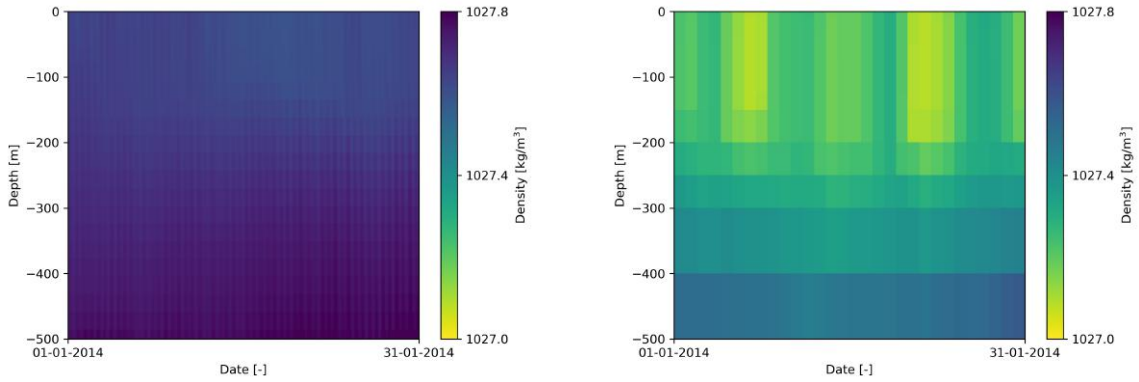

(a) 3D DCSM-FM by Zijl et al. (2016)

(b) Ocean model by CMEMS (2018)

Figure 3.5: Plot of the density profile [kg/m^3] at Location 1 over depth and time for (a) the 3D DCSM-FM by Zijl et al. (2016) and (b) the ocean model by CMEMS (2018).

3.2.4. Flow velocity and flow direction

Since no actual flow velocity measurements throughout the water column are available at Location 1 or 2, datasets from BODC (2018) are used to verify the magnitude and the direction of the flow velocity in the 3D DCSM-FM. These datasets consist of a time series of the flow velocity and flow direction, measured at a fixed depth. Around the Shetland Islands, six measuring stations provide suitable time series for a comparison of the behaviour of the flow at Location 1. In Appendix G, specific details of the measuring stations and datasets are written down.

Figure 3.6 contains plots of the magnitude and direction of the flow velocity for both the 3D DCSM-FM and the measurements. Each row represents a part of the water column, which is indicated in the top left corner, h=40 m, for example. These layers from the model are chosen as corresponding time series of measurements were available at those depths. It should be noted that the model time ranges, which are ranging from May to December 2013, differ from the periods of the measurements, as these are from 1972, 1982 and 1988. However, for a visual comparison of the processes, this is not a problem.

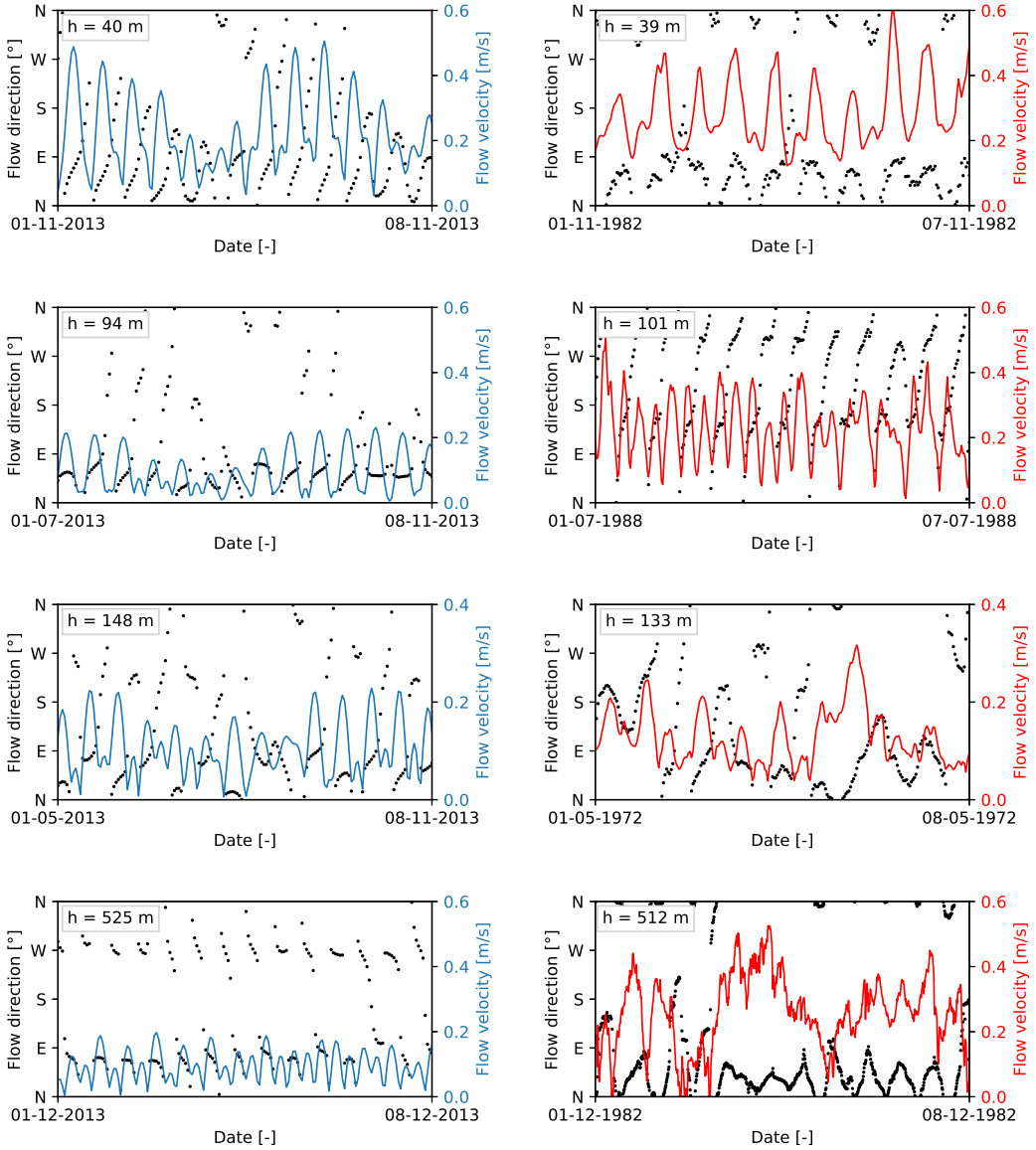

Figure 3.6: Plots of the magnitude [m/s] and the direction [°] of the flow velocity at Location 1 in the 3D DCSM-FM by Zijl et al. (2016) in blue and from the measurement stations by BODC (2018) in red, see Figure G.5. Each row represents a part of the water column, which is indicated in the top left corner.

The similarities and differences between the 3D DCSM-FM and the measurements from BODC (2018) are listed below. Both the plots of the model and the measurements show periodic behaviour over time. This can be observed in the top part of Figure 3.6, in which the direction of the flow varies one or two times per day from north to east and vice versa. This periodicity is appearing more in the upper part of the water column than in the lower part, which can be explained by the intrusion of the tide that decreases for larger depths. In general, the values of the magnitude of the velocity in the model are slightly lower than the measurements, predominantly in the bottom layer of the water column. At certain moments in time, the measured velocity is three times higher than the modelled velocity. However, the velocities in the 3D DCSM-FM give a fair representation of the occurring flow patterns in the area.

3.2.5. Conclusions

In summary, the 3D DCSM-FM by Zijl et al. (2016) is considered to be a suitable hydrodynamic model for this research. Both the depth profile and water level elevation are represented accurately in the model, based on comparisons with SRI vessel data and measurements from the tidal station in Lerwick (EMODnet, 2017). The density profile over depth generated by the 3D DCSM-FM does not provide a clear representation of the baroclinic processes, which take place in the area around the Shetland Islands. Therefore, one should be cautious while interpreting density output from this model. At last, plots of the magnitude and direction of the flow velocity show a similar periodicity, as measured by BODC (2018). However, the values of the flow velocity measurements in the bottom layer of the water column seem to be slightly higher than the modelled velocities.

Chapter 4

Pattern identification by combining data

As discussed in Chapter 3, the 3D DCSM-FM by Zijl et al. (2016) is considered as a reliable source of hydrodynamic data. This data is plotted for each of the ten selected tracks, which consist of a subsequent number of days that a vessel was working on a project, individually. Since Van Oord has mainly worked at two project areas, which are located a hundred kilometers away from each other, a distinction is made between these two locations, called Location 1 and 2. Due to the large distance between these two locations, the local topography and conditions might differ significantly. In Figure 4.1 and Table 4.1, the boundaries of the areas and the corresponding tracks are presented.

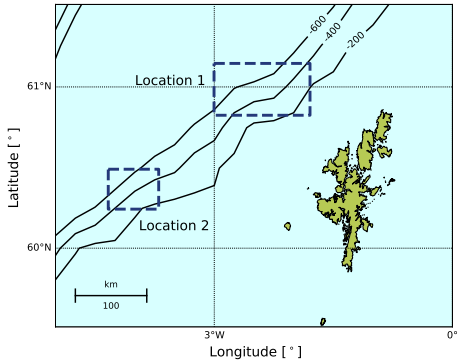

Figure 4.1: Area around the Shetland Islands, including locations of the projects indicated by blue-dotted boxes.

Table 4.1: Overview of the track codes and their corresponding location, specified in Figure 4.1.

Track code	Location
S4	2
$S6_1$	2
$S6_2$	2
S7	2
S8	1
S9	1
S10	1
S11	1
N4	1
N13	1

The output data from the 3D DSCM-FM, coinciding with the time ranges of these tracks, is summarised in an overview plot, see Figure 4.2 for an example. The plot contains a map depicting the sailed path and plots of the working schedule, water level elevation, flow velocity, flow direction, turbulent vertical eddy viscosity, density, Richardson number and the spring-neap cycle. Moreover, depth profiles of certain variables during non-working intervals are included. A detailed description of each aspect of the overview plot can be found in Appendix E, which also contains the overview plot for every individual track. For the purpose of comparison, the limits of the different plot axes are fixed in every overview plot. The data from the DPRs and the AIS are coupled by interpolating the track locations of the vessel to the times of the 3D DCSM-FM output, which is generated hourly. Subsequently, this output is interpolated in space to these locations.

The overview plots are interpreted and appearing findings are discussed in Section 4.1. Certain phenomena, such as shear, veering and the wind direction, are not included in the overview plots. To be able to assess these phenomena, additional plots are created, which are presented in Section 4.1 as well. From all findings and results, explained in Section 4.1, a couple of hypotheses and conclusions are drawn, which are listed in Section 4.2.

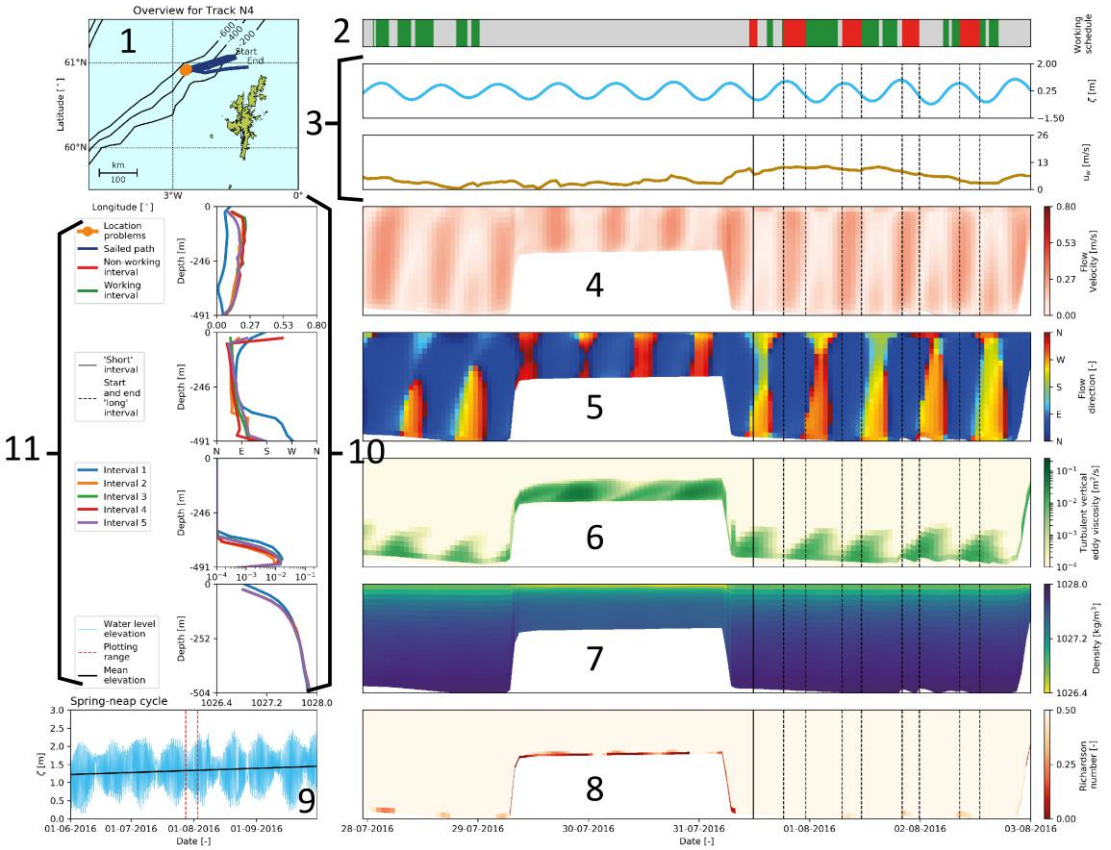

Figure 4.2: Overview plot of the data from the 3D DCSM-FM model by Zijl et al. (2016), combined with the data from the DPRs of the Nordnes for the period ranging from 28-07-2016 to 03-08-2016 (Track N4). In the upper left corner, a map of the area around the Shetland Islands is presented. The blue track represents the sailed path of the SRI vessel. On the right side a couple of variables are plotted over time. From top to bottom: the working schedule, the water level elevation [m], the wind speed [m/s], the flow velocity [m/s], the flow direction [-], the turbulent vertical eddy viscosity [m^2/s], the density [kg/m^3] and the Richardson number [-]. For the flow velocity, flow direction, turbulent vertical eddy viscosity and the density, a depth profile averaged over time per non-working interval is plotted on the left side of the figure. On the bottom left part, the water level elevation, retrieved from EMODnet (2017), is plotted, indicating the spring-neap cycle.

4.1. Interpretation overview plots

Each paragraph in this section describes the behaviour over time and or depth of one of the phenomena mentioned in the introduction of this chapter, which are part of the overview plot. These topics are discussed according to their position in Figure 4.2, starting with the water level elevation and ending with shear and veering patterns.

Vertical and horizontal tide

The periodicity of the tide is visible in the colour plots of the flow velocity, flow direction and the turbulent vertical eddy viscosity (see plot 4, 5 and 6 on the right in Figure 4.2, for example). The changes in these plots coincide with the elevation of the water level (ζ) and the red parts of the working schedule. For example, the profile of the flow velocity is alternately darker red (higher flow velocities) or lighter red (lower flow velocities) twice a day, corresponding to non-working intervals in the working schedule. However, the vertical tide is not considered as a good indicator for this possible correlation, because the tidal amplitude is at least two orders of magnitude smaller than the total depth of the water column. Therefore, a more detailed tidal analysis is performed to assess whether or not correlations with the horizontal tide are observable as well. This is done by means of a Fast Fourier Transform (FFT), which is described in Chapter 5.

Wind direction

As mentioned in Chapter 2, the presence of a continental shelf in the ocean might result in additional physical phenomena that play a role in the flow conditions at that location. One of this phenomena is the continental shelf wave, which is generated, for example, by strong wind speeds. To be able to assess the appearance of

these shelf waves around the Shetland Islands, wind roses are composed from the 3D DCSM-FM output, see Figure 4.3. In these wind roses, the magnitude and direction of the wind at Location 2 are plotted for the working and non-working intervals, lasting longer than two hours, respectively. The wind rose for Location 1, which has the same lay-out as the one presented below, can be found in Appendix F. During the non-working intervals at Location 2, the larger wind speeds (> 6 m/s) originate from the north-west and the north-east. Wind from both these directions might cause the development of a continental shelf wave as their orientations with respect to the shelf edge are perpendicular and parallel. However, the actual presence of continental shelf waves is assessed by analysing the behaviour of the flow at that specific location, see Chapter 5.

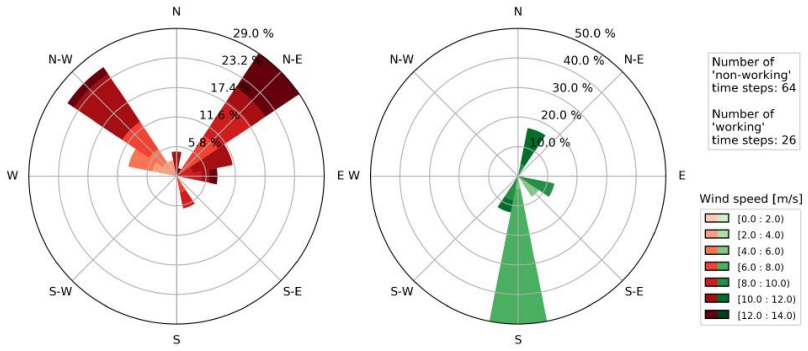

Figure 4.3: Wind rose of the magnitude [m/s] and the direction [°] of the wind at Location 2 for all working (green) and non-working (red) intervals, lasting longer than two hours, assembled. Data retrieved from the 3D DCSM-FM by Zijl et al. (2016).

Flow direction

The colour plots of the flow direction in the overview plot (see plot 5 on the right in Figure 4.2, for example) show multiple direction changes over depth and time per track. The occurrence of these variations in flow direction can be explained by the changing direction of the tide caused by the M_2-component. In order to quantify these changes and visualise the correlation with the working and non-working intervals, roses are created, see Figure 4.4. An additional distinction is made between the different parts of the water column, which is subdivided in three sections. The top part consists of the upper quarter of the water column and the bottom part is the lowest quarter, see Figure 4.5. The remaining sections form the middle part, which is therefore twice as thick as the top and bottom part.

Figure 4.4 depicts the rose for the bottom part at Location 2, whereas the roses of the other parts of Location 2 and all parts of Location 1 can be found in Appendix F. The plot of the bottom part at Location 2 shows a clear correlation between the flow direction and the presence of a non-working interval. During a non-working interval, the water is flowing to the east or east-northeast, whereas during a working interval the main flow directions are west-southwest and west.

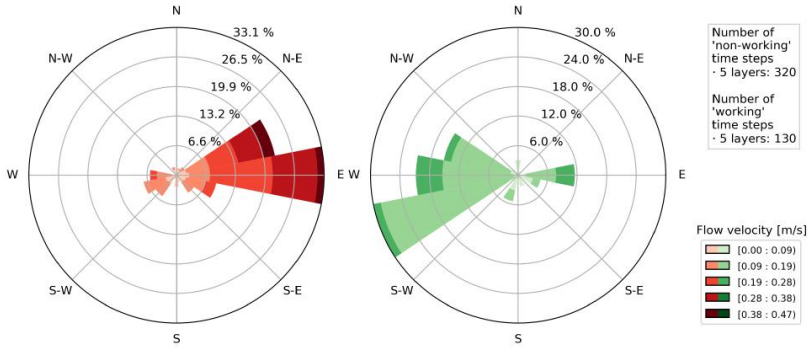

Figure 4.4: Rose of the magnitude [m/s] and the direction [°] of the flow in the bottom part (lowest quarter of the water column) at Location 2 for all the available working (green) and non-working (red) intervals assembled. Data retrieved from the 3D DCSM-FM by Zijl et al. (2016).

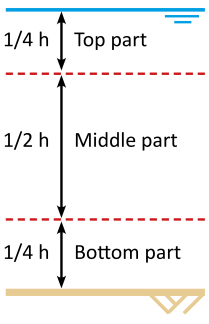

Figure 4.5: Subdivision of the water column in three sections: top part, middle part and bottom part.

This visual correlation is quantified in Table 4.2, which contains the percentage of time that the flow was directed to one of the sixteen main directions. In the table, a distinction is made between working and non-working intervals. The numbers are in line with the visual observation, as the percentages and the number of time steps for east and east-northeast are significant during non-working intervals: 100% for 72 time steps and 88% for 121 time steps. The same yields for the west-southwest and west direction during working intervals.

Table 4.2: Overview of the percentages of time that the flow was directed to each of the sixteen flow directions (FD) during working and non-working intervals in the bottom part of the water column at Location 2. The number of time steps per direction (#) is included to indicate the contribution to the total number of data points from the 3D DCSM-FM by Zijl et al. (2016), which is 450.

Location 2 - Bottom part															
FD	●	●	#	**FD**	●	●	#	**FD**	●	●	#	**FD**	●	●	#
N	33%	67%	6	E	88%	12%	121	S	89%	11%	9	W	41%	59%	46
NNE	83%	17%	6	ESE	83%	17%	35	SSW	30%	70%	10	WNW	0%	100%	20
NE	88%	12%	8	SE	94%	6%	16	SW	90%	10%	20	NW	33%	67%	3
ENE	100%	0%	72	SSE	63%	37%	8	WSW	38%	62%	63	NNW	86%	14%	7

Turbulence

The major part of the colour plots of the turbulent vertical eddy viscosity (ν_{eddy}) in the overview plots (see plot 6 on the right in Figure 4.2, for example) show turbulent structures at the bottom and or top part of the water column. Their appearance seems to coincide with the elevation of the water level and the changes in direction of the flow. Moreover, the non-working intervals start as the turbulence in the lower part of the water column increases from 10^{-4} m^2/s or 10^{-3} m^2/s to at least 10^{-2} m^2/s. Both relations can be visually observed in Figure 4.6a, containing the profile for Track S6$_2$. However, when one studies the colour plot of the turbulent vertical eddy viscosity of a different track, it turns out that a turbulent structure at the bottom part of the water column does not necessarily initiate a non-working interval, see Figure 4.6b. On the left side of this plot, two turbulent structures at the bottom coincide with multiple working intervals.

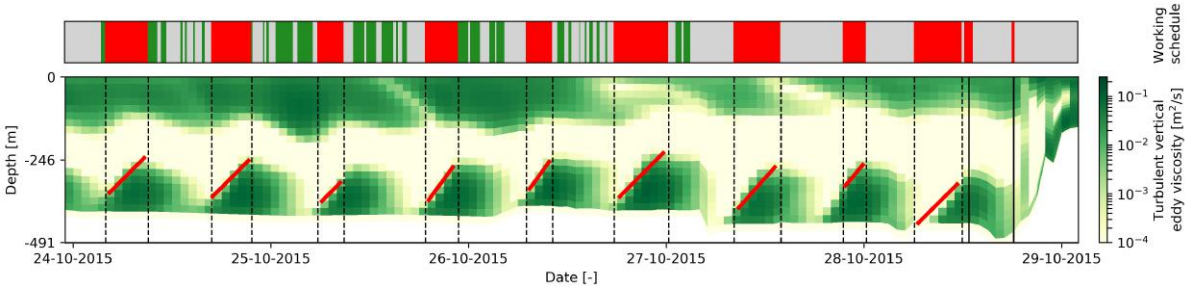

(a) Track S6$_2$

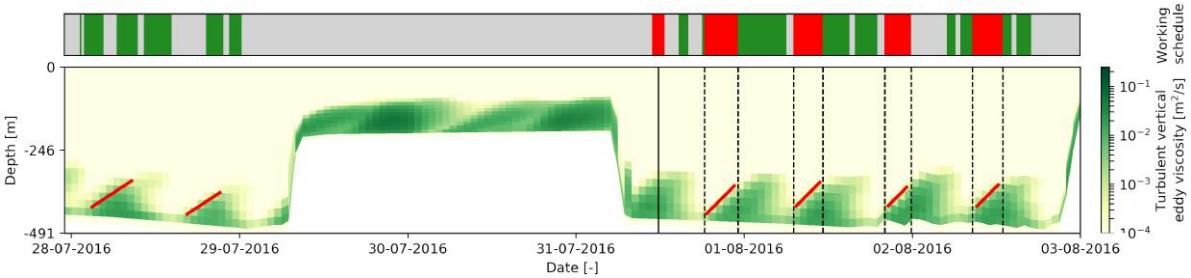

(b) Track N4

Figure 4.6: Colour plot of the turbulent vertical eddy viscosity [m^2/s] of (a) Track S6$_2$ and (b) Track N4, including red lines that highlight the increase in turbulent vertical eddy viscosity during the occurrence of a working or a non-working interval. Above the colour plot, the working schedule is included for completeness. Data retrieved from the 3D DCSM-FM by Zijl et al. (2016).

In order to quantify the visual observations, a scatter plot of the turbulence is created for Location 1 and 2. As the dimensions of these plots are significant, the plots can be found in Figures F.5 and F.6 in Appendix F. For the moments in time during working and non-working intervals, the value of the turbulent vertical

eddy viscosity (ν_{eddy}) and the first derivative in time of the turbulent vertical eddy viscosity ($\frac{\partial \nu_{\text{eddy}}}{\partial t}$) in the bottom layer of the water column are plotted against five different variables related to the velocity (u). These five variables are the standard flow velocity and the first and second derivative in space and time of the flow velocity. The green dots in the scatter plot indicate working intervals and the red dots indicate non-working intervals. Furthermore, a coefficient, indicating the correlation between both variables in the plot, is depicted in the corner. These numbers are based on the correlation coefficients in Figure 4.7.

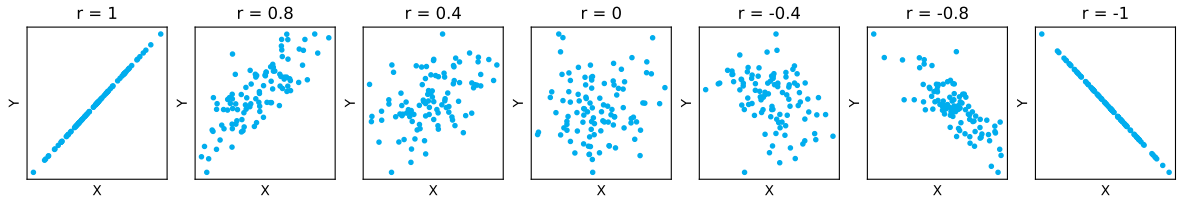

Figure 4.7: Overview of a part of the correlations that can theoretically exist between two variables X and Y.

For Location 1, no significant differences between the green and the red dots can be identified for both the turbulent vertical eddy viscosity and the first derivative of this property in time, see Figure F.5. However, for the plots of the turbulent vertical eddy viscosity at Location 2, the positions of the red dots differ from the positions of the green dots, see Figure F.6. The major part of the red dots is positioned in the higher regions of the graphs (values higher than 10^{-2} m^2/s), whereas the green dots are predominantly found around 10^{-2} m^2/s. The difference between Location 1 and 2 is quantified by computing the correlation coefficient for each of the five variables, see Table 4.3. In five of the five cases, the correlation coefficient for the non-working intervals is significantly higher at Location 2 than at Location 1.

Table 4.3: Overview of the correlation coefficients of the turbulent vertical eddy viscosity (ν_{eddy}) and five different flow velocity variables at Location 1 and 2. The coefficients are obtained from Figures F.5 and F.6 in Appendix F.

ν_{eddy}	u	$\frac{\partial u}{\partial t}$	$\frac{\partial^2 u}{\partial t^2}$	$\frac{\partial u}{\partial z}$	$\frac{\partial^2 u}{\partial z^2}$
Location 1					
Working intervals (●)	0.075	-0.130	0.082	0.130	-0.073
Non-working intervals (●)	-0.095	-0.230	0.147	0.266	0.003
Location 2					
Working intervals (●)	0.063	0.003	-0.152	0.262	0.082
Non-working intervals (●)	0.331	-0.521	0.310	0.383	0.020

The same type of plots are made for two other turbulent variables from the output of the 3D DCSM-FM, namely the turbulent kinetic energy (k) and the turbulent energy dissipation (ϵ). These plots can be found in Appendix F. For these variables, the same conclusion yields as the red dots are located in the upper area of the graphs of Location 2.

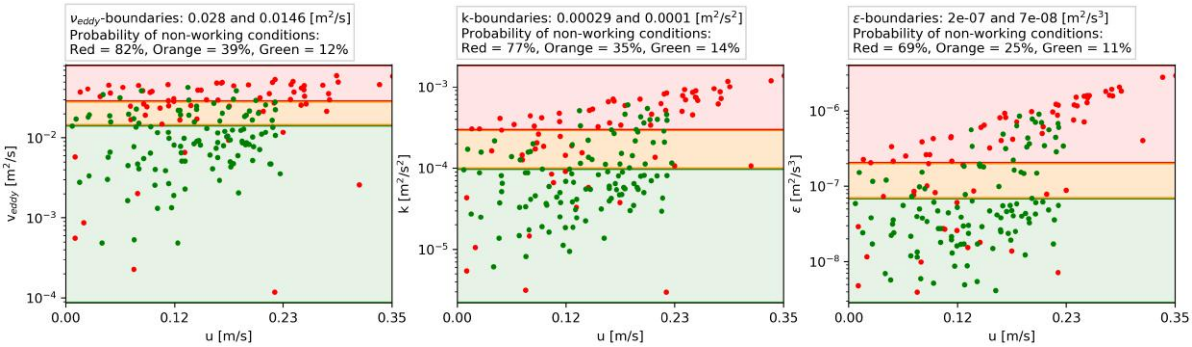

Figure 4.8: Indication of the probability of non-working conditions at Location 2 subdivided in a red, orange and green zone for the turbulent vertical eddy viscosity (ν_{eddy}, the turbulent kinetic energy (k) and the turbulent energy dissipation (ϵ). Data retrieved from the 3D DCSM-FM by Zijl et al. (2016).

Therefore, the scatter diagram of each of the three turbulent variables at Location 2 is used to indicate the probability of non-working conditions, see Figure 4.8. The graphs are subdivided in a red, orange and green zone, which each have their own probability. The probability is higher for the red zones as these parts of the graphs contain more red dots. In conclusion, for certain values of the turbulent vertical eddy viscosity, turbulent kinetic energy and turbulent energy dissipation in the bottom layer of the water column, the chance on non-working conditions increases significantly, at Location 2. This makes sense as the ROV is positioned in this part of the water column and might have difficulties with remaining at its correct dynamic position.

Shear and veering

Both the magnitude and direction of the flow velocity vary significantly over time and depth, which is visible in the overview plots of the tracks in Appendix E. Shear and veering are two phenomena, that are related to these variations, representing the change in flow velocity and flow direction over depth, respectively. For a proper assessment of the behaviour of these phenomena, the derivative of the two horizontal components of the flow velocity and the flow direction over depth ($\frac{\partial u}{\partial z}$, $\frac{\partial v}{\partial z}$ and $\frac{\partial \theta}{\partial z}$) are calculated per layer. This is done for each working and non-working interval per track, individually. Figure 4.9 depicts the results of one of each interval types, consisting of multiple time steps. Each plot also contains an indication of the length of the interval and a legend that specifies the line colour for every time step. Appendix F contains four more graphs of the shear and veering patterns.

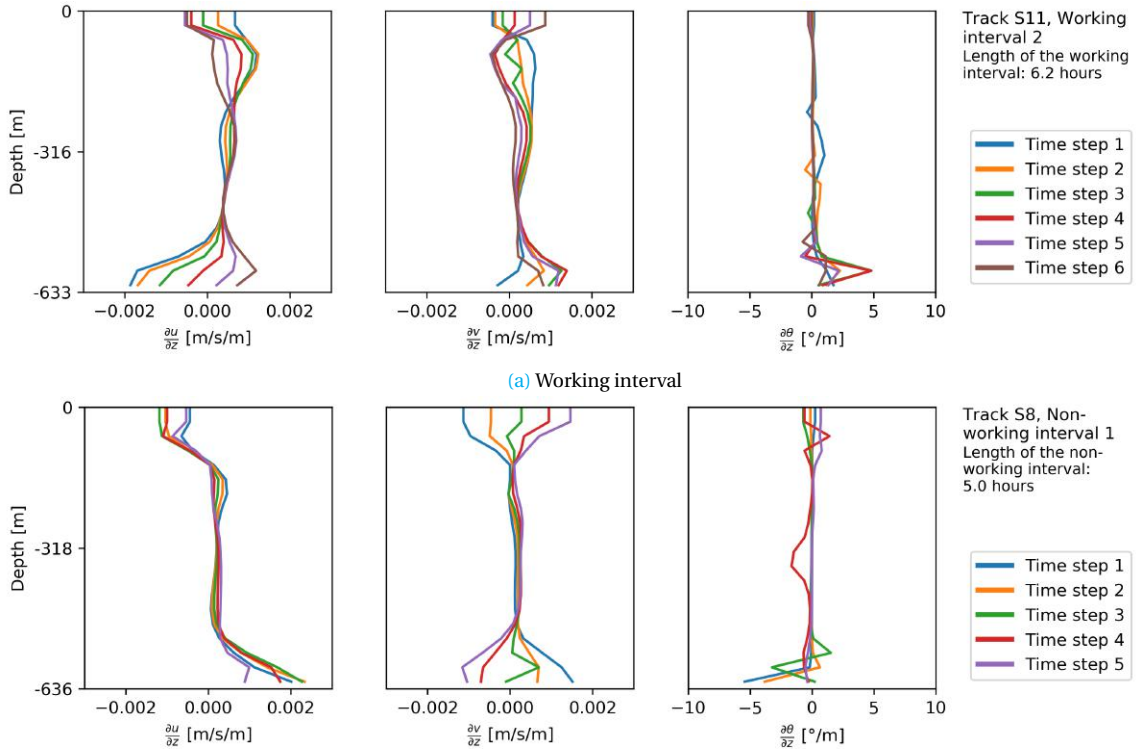

(a) Working interval

(b) Non-working interval

Figure 4.9: Plot of the shear in x-direction [m/s/m] (left), the shear in y-direction [m/s/m] (middle) and the veering [°/m] (right) in the water column for (a) a working interval and (b) a non-working interval. Data retrieved from the 3D DCSM-FM by Zijl et al. (2016).

The plots of the shear profiles are hard to quantify, qualify or compare as the patterns differ significantly for each working and non-working interval. However, for both the working and the non-working intervals, the middle part remains relatively steady, whereas in the top and bottom part, slight changes in the magnitude of the flow over depth occur. This can be observed, for example, in the middle part of Figure 4.9a and the left part of Figure 4.9b. In conclusion, no significant differences in the shear and veering patterns during the working and non-working intervals can be distinguished from these plots. The same conclusion can be drawn for the veering, as for both the working and the non-working intervals small changes in flow direction are visible. The direction changes are indicated by the horizontal peaks in the right part of Figures 4.9a and 4.9b.

Based on the analysis of the shear and veering patterns in the water column, it can be concluded that both phenomena are not singularly responsible for the interruption of the working activities, as the working and non-working interval patterns are almost identical. However, due to the coarseness of the layers in the model (one layer is 30 meters thick at a depth of 600 meters), it is highly possible that a part of the detailed shear and veering patterns is not captured by the 3D DCSM-FM by Zijl et al. (2016).

4.2. Hypotheses and conclusions

After interpreting the combined information from the DPRs, the AIS data and the output from the 3D DCSM-FM, the following hypotheses and conclusions are posed:

1. The appearance of a non-working interval seems to be linked to the magnitude and periodicity of the horizontal tide. These correlations are assessed by means of an FFT, see Chapter 5;

2. The conditions for the presence of continental shelf waves are met at Location 2, but not at Location 1. The final assessment of the presence of these shelf waves is made based on the results of the FFT in Chapter 5;

3. In case the water is flowing to the east or east-northeast in the bottom part of the water column at Location 2, it is highly likely that the working activities are interrupted. This conclusion follows from the flow rose, which indicates that tidal flow to the East results in non-working conditions in 100% of the cases, whereas tidal flow oriented to the East-northeast has a probability of 88%.

4. At Location 2, for values of the turbulent vertical eddy viscosity (ν_{eddy}) in the bottom layer of the water column higher than 0.028 m^2/s, the chance on non-working conditions increases. The same yields for values of the turbulent kinetic energy higher than $2.9 \cdot 10^{-4}$ m^2/s^2 and for values of the turbulent energy dissipation higher than $2.0 \cdot 10^{-7}$ m^2/s^3;

5. The phenomena of shear and veering are not singularly responsible for the interruption of the working activities. However, due to the coarseness of the layers in the model (one layer is 30 meters thick at a depth of 600 meters), it is highly possible that a part of the detailed shear and veering patterns is not captured by the model.

These hypotheses and conclusions are further assessed in the next chapters, in which an FFT is described and the data from the SRI vessels is analysed. In Chapter 8, a final assessment of each of this hypotheses is stated.

Chapter 5

Tidal analysis by a Fast Fourier Transform

The variation of the water level elevation at the project locations around the Shetland Islands has been analysed in Section 4.1. It turns out that the tidal movements seem to dominate the behaviour of both the flow velocity and the flow direction. In order to determine whether or not the tide is fully responsible for this behaviour, a more-detailed tidal analysis is performed. This is done by means of a Fast Fourier Transform (FFT). A general description of the characteristics of an FFT is given in Appendix C. The following two types of the FFT are discussed and applied to the output of the 3D DCSM-FM by Zijl et al. (2016):

- A regular FFT, in which periodic movements with a constant predefined tidal frequency are identified and filtered from the original flow velocity signal. The proper functioning of this method is verified by putting in the elevation of the water level, see Appendix G. Table G.1 in Appendix G provides an overview of the main tidal constituents that are filtered from the velocity signal. In the remaining part of this chapter this type is called the 'regular' FFT.
- A special type of the FFT from the Tidal Analysis Program in Python (TAPPY), that filters all movements with a frequency higher than 0.8 cpd from the original flow velocity signal. This analysis is based on the findings of Walters and Heston (1982) and is named TAPPY in this chapter.

In Section 5.1, the set-up and the results of both FFT types for the output data from the 3D DCSM-FM by Zijl et al. (2016) are presented. Subsequently, in Section 5.2, the results are analysed and appearing features are pointed out.

5.1. FFT set-up and results

The FFT is applied to the signal of the flow velocity (see plot 4 on the right in Figure 4.2, for example), according to the theory described in Appendix C. To be able to perform an FFT on the output of the 3D DCSM-FM, a few simplifications and assumptions are made. First, it is chosen to take the flow velocity output of the stations that were assigned to Location 1 and 2 in Chapter 3, see Figure 3.4. Secondly, one out of the twenty depth layers is selected for the analysis, as it is not possible to merge the spectra of multiple layers. From the spectra created for each layer can be concluded that Layer 14, which is one the middle layers, is representative for the entire water column as it contains the widest spread in frequencies and the highest peaks. In the bottom layers, for example, fewer flow movements are observed and therefore the spectrum contains less distinctive peaks.

The second assumption regards the mean value of the flow velocity over time, which is approximately equal to 0.15 m/s. This value represents the slow-moving part of the signal and results in a dominant low-frequency peak in the spectrum around zero. This peak is filtered, by subtracting the mean of the signal, as it decreases the quality of the results of the FFT. The FFT and filtering are performed for the component of the flow velocity both in x-direction and y-direction, before the results are merged to a total signal. Figure 5.1 depicts the original frequency spectrum and the spectrum that remains after the velocity signal in y-direction is filtered, for the regular FFT and the TAPPY FFT. The spectra for the signal in x-direction can be found in Appendix G.

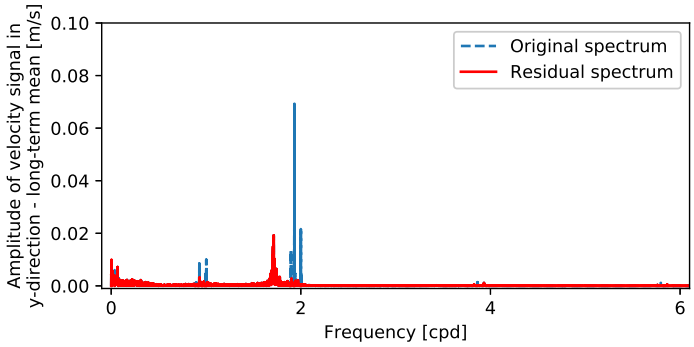

(a) Regular FFT

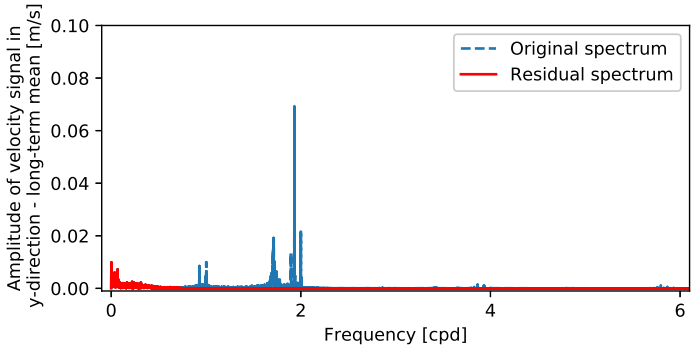

(b) TAPPY FFT

Figure 5.1: Frequency spectrum of flow velocity [m/s] in y-direction at Location 1 for (a) a regular FFT and (b) the TAPPY FFT. The original (blue) and residual (red) frequency spectrum are depicted for Layer 14 of the 3D DCSM-FM by Zijl et al. (2016).

Both of the spectra in Figure 5.1 can be considered as a so-called 'narrow' spectrum of which the signal consists of modulated harmonic elevations (Holthuijsen, 2007). The main difference between both spectra is the peak around 1.7 cpd, which is not filtered in the regular FFT, see Figure 5.1a. Table G.2 in Appendix G contains an overview of the amplitudes of the different tidal constituents. In Figure 5.2a a small time range of the total length of the combined flow velocity signal is decomposed in three different parts. The blue line represents the original signal of the velocity, whereas the orange line depicts the tidal signal that is filtered from the original signal. The red line is the residual signal, obtained after subtraction of the tidal signal from the original signal. The tidal part oscillates around zero, which is in line with the expectations of this specific phenomenon. The varying amplitude of the tidal signal is due to the spring-neap cycle and the interaction between the different tidal constituents. The residual signal of the TAPPY FFT is much flatter and less periodic than the residual signal of the regular FFT, see Figure 5.2b.

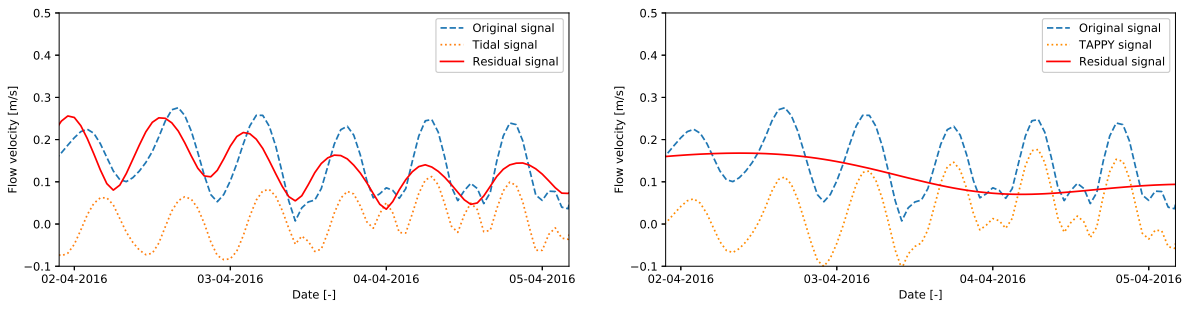

(a) Regular FFT

(b) TAPPY FFT

Figure 5.2: Plot of a time range of approximately three days containing the original (blue), tidal (orange) and the residual (red) signal of the flow velocity [m/s] for (a) a regular FFT and (b) the TAPPY FFT. The signal depicts the flow in Layer 14 of the 3D DCSM-FM by Zijl et al. (2016) at Location 1.

5.2. Conclusions FFT

The results of the FFT of the 3D DCSM-FM output, consisting of the filtered spectrum and the residual signal, presented in Section 5.1, are interpreted in this section. Table 5.1 and 5.2 contain a couple of numbers, such as the mean flow velocity and the variance, for each of the components indicated in Figure 5.2. Two main conclusions can be drawn from these overview tables. In the first place, the mean values of the different signals prove that the residual signal still has a significant amplitude. Secondly, the filtered tidal signal explains 80% (89%) of the variance, whereas the value for the residual signal is 20% (11%) for the regular FFT and the TAPPY FFT, respectively. These numbers are based on the surface area under the frequency spectra in Figure 5.1. Therefore, it can be concluded that a significant part of the variations in the magnitude of the flow velocity is due to the presence of the tide.

Table 5.1: Overview of the mean and maximum value of the flow velocity [m/s] and the variance [%] for the original signal, and both the tidal and residual signal of the regular FFT.

Regular FFT	$\|u\|_{mean}$ [m/s]	$\|u\|_{max}$ [m/s]	**Variance** [%]
Original signal	0.146	0.496	100
Tidal signal	0.071	0.237	80
Residual signal	0.120	0.439	20

Table 5.2: Overview of the mean and maximum value of the flow velocity [m/s] and the variance [%] for the original signal, and both the tidal and residual signal of the TAPPY FFT.

TAPPY FFT	$\|u\|_{mean}$ [m/s]	$\|u\|_{max}$ [m/s]	**Variance** [%]
Original signal	0.146	0.496	100
TAPPY signal	0.077	0.365	89
Residual signal	0.108	0.325	11

Residual spectrum

The characteristics of the remaining part of the signal are assessed by analysing the filtered spectrum and the plots of the flow velocity signal for each of the tracks, selected in Chapter 3. Figure 5.3 depicts a zoom of the residual spectra of both types of the FFT. The different tidal constituents are indicated by their abbreviation and a black-dotted line.

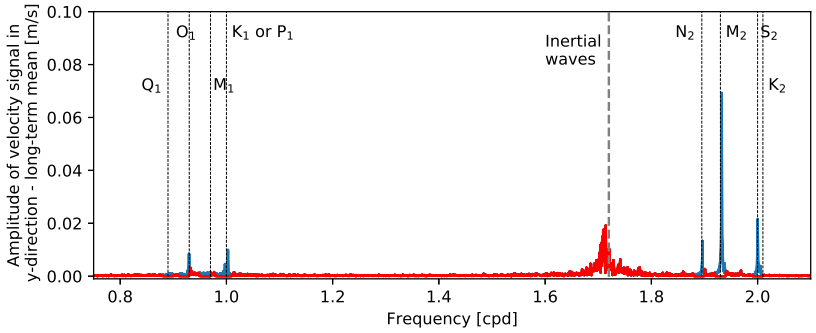

(a) Regular FFT, range 0.8 to 2.0 cpd

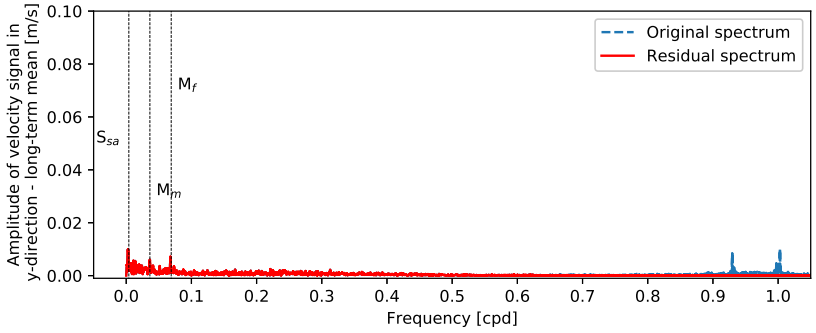

(b) TAPPY FFT, range 0.0 to 1.0 cpd

Figure 5.3: Zoom of the frequency spectrum of flow velocity [m/s] in y-direction from the 3D DCSM-FM by Zijl et al. (2016) at Location 1 for (a) a regular FFT and (b) the TAPPY FFT. The original (blue) and residual (red) frequency spectrum are depicted for Layer 14 of the 3D DCSM-FM by Zijl et al. (2016).

The spectrum of the regular FFT analysis contains one high peak around 1.7 cpd, see Figure 5.3a. This peak cannot be explained by the presence of a tidal component as the known constituents are filtered from the signal. Therefore, the characteristics of other hydrodynamic phenomena are compared to these frequencies ranging from approximately 1.65 to 1.8. It turns out that the frequency of inertial waves, which are described in Chapter 2, lies exactly within this range for the area around the Shetland Islands. This is indicated in the plot of the residual spectrum by a grey-dotted line, see Figure 5.3a. As this line corresponds almost exactly to the remaining red peak, it is highly likeable that this peak is the result of the presence of inertial waves. The characteristic frequency of the continental shelf waves (0.35) is not visible in the spectrum and are therefore not considered in this analysis. The residual spectrum of the TAPPY FFT is completely flat for values higher than 0.8 cpd, as all these values are filtered. The low-frequency tidal constituents are still observable in the spectrum, which explains the slowly moving periodic elevation in Figure 5.2b.

Residual signal

The plots of the flow velocity signals for the different tracks indicate that these inertial waves do not cause the non-working intervals. This can be concluded from Figure 5.4a, which depicts the different components of the velocity signal for Track S4. The black line, that contains the signal of the inertial waves, shows the same pattern during both working and non-working intervals. A similar trend is observed in the plots of the other tracks. Figure 5.4b shows an almost constant amplitude of the flow velocity during the entire time range. This means that the low-frequency tidal components are not responsible for the interruption of the working activities.

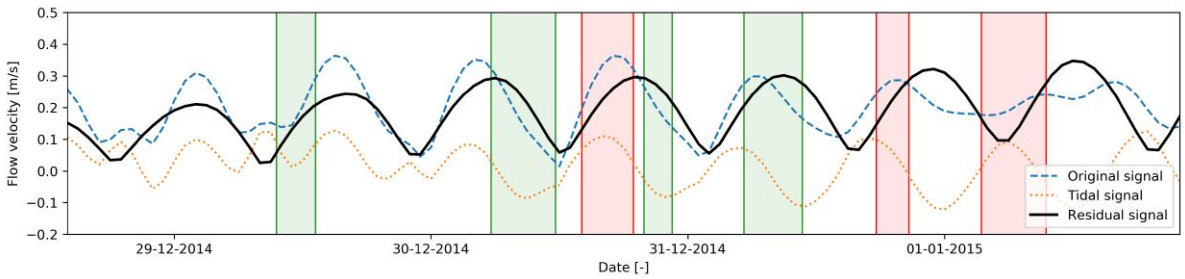

(a) Regular FFT

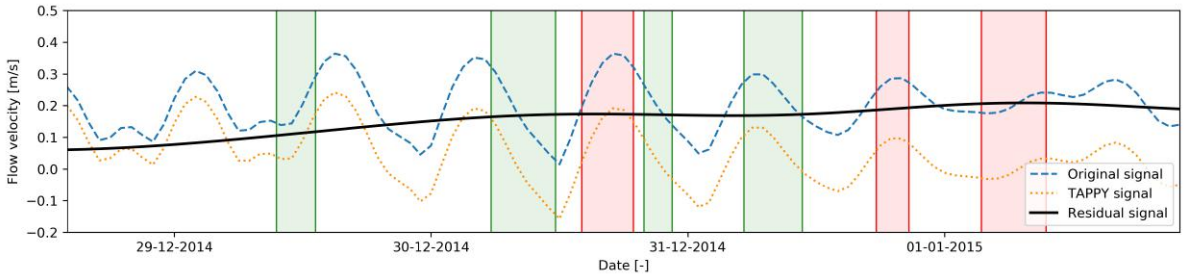

(b) TAPPY FFT

Figure 5.4: Plot of the original flow velocity signal [m/s] (blue), tidal signal [m/s] (orange) and the residual signal [m/s] (black) in Layer 14 at Location 1 for Track S4 for (a) a regular FFT and (b) the TAPPY FFT. The green and red vertical lines represent the working and non-working intervals with a duration of at least 2% of the plotted time range.

Residual flow direction

Figure 5.5 contains the flow direction of the original, tidal en residual signal for a time range of approximately three days. The original and tidal signal fluctuate back and forth over time from west to east, whereas the residual signal is relatively steady. For both the regular and the TAPPY FFT, the signal is oriented to the north-east. This orientation corresponds to the direction of the large ocean gyre, which propagates around the Shetland Islands. This gyre is called the NAC and was mentioned before in Chapter 2. The TAPPY signal in Figure 5.5b is flatter than the signal from the regular FFT, as the inertial waves are not included.

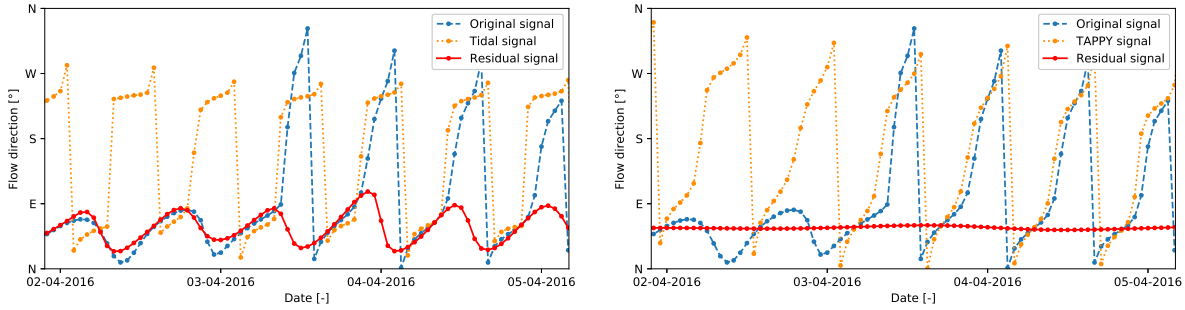

(a) Regular FFT

(b) TAPPY FFT

Figure 5.5: Plot of a time range of approximately three days containing the original (blue), tidal (orange) and the residual (red) signal of the flow direction [°] for (a) a regular FFT and (b) the TAPPY FFT. The signal depicts the flow direction in Layer 14 of the 3D DCSM-FM by Zijl et al. (2016) at Location 1.

In general, the tide does play a significant role in the area around the Shetland Islands. The FFT turns out to be a useful method for the identification of the different components in the flow velocity signal, as almost all parts are assigned to a certain hydrodynamic phenomenon. However, these phenomena are prevailing over the entire time range and are therefore unlikely to be the cause of the interruption of the working activities. In order to get a better idea of the cause of the problem, the data which is logged by the SRI vessels, is analysed and compared to the 3D DCSM-FM output in Chapter 6.

Chapter 6

SRI vessel data analysis

In Section 3.2.1, the position of the ROV in the water column from the signals of the SRI vessels was used to verify the depth profile of the 3D DCSM-FM. In this chapter, other logged variables are used to assess and identify patterns in the appearance of the working and non-working intervals. Vessel data is available for Track N4, N13, S7, S8, S9, S10 and S11, which are seven of the ten selected tracks. From the original 25 Hz vessel data recordings, a one minute subsampling was provided. After this 1500 times data reduction, the datasets still have significant sizes. For plotting purposes, downsampling is applied to the different datasets. This results in a selection of the minimum and the maximum value within a certain interval, for example 60 minutes. In that case the downsampling rate of that variable is equal to 30. In Sections 6.1 to 6.4, the orientation, deviation, velocity, horizontal power and motions of the ROV are discussed, whereas Section 6.6 summarises the results. In case the ROV is not deployed, it is located on the moonpool above the water surface. For these moments in time a small grey dot (●) is plotted in the graphs.

6.1. Orientation

The heading of the SRI vessel depends on the type of activity that is scheduled for a certain time range. In case the vessel has to sail to Norway to obtain new rocks, the heading is similar to the direction of the quarry location. However, during installation activities, for example, the heading of the vessel can be adjusted to either the flow direction or the dominant wave direction. This might change within the hour or even within a shorter time range and is monitored closely by the operators on board. Figure 6.1 depicts the yaw and the heading of the ROV for Track N4. Over time, both the yaw and the heading of the ROV are relatively steady. The orientation of both variables seems to be either the same or opposite. However, in the plot, no correlation between the heading of the vessel and the ROV seems to be noticeable during working or non-working intervals. One would expect coinciding directions during working intervals and opposite directions during non-working intervals.

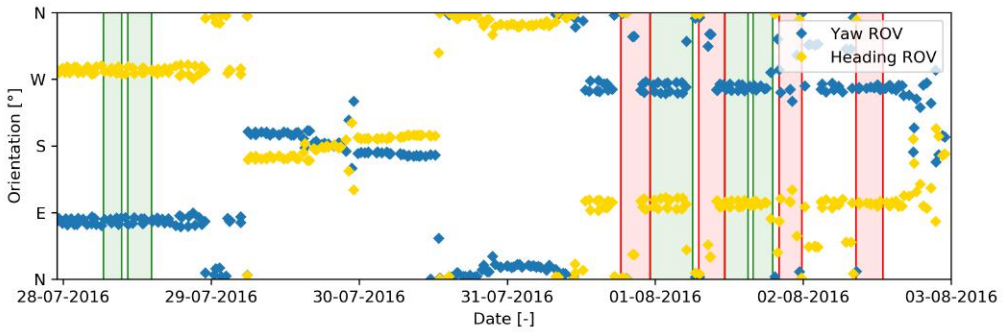

Figure 6.1: Plot of the yaw of the ROV [°] (blue) and the heading of the ROV [°] (yellow) for Track N4. The green and red vertical lines represent the working and non-working intervals with a duration of at least 2% of the plotted time range. The downsampling rate of the variables is 30.

Since the heading depends, amongst others, on the dominant flow direction, the logged vessel data is compared to the output of the 3D DCSM-FM, see Figure 6.2. One would expect indications of a similar flow direction and moonpool heading when the vessel is sailing. This is the case from July 29th to July 31st, see Figure 6.2a. At certain moments in time, the yaw of the ROV coincides with the flow direction, whereas in other cases the heading is oriented opposite to the flow. In general, based on the results in Figure 6.2, one can conclude that neither the moonpool heading nor the yaw of the ROV seems to be influenced by the periodical changes in magnitude and flow direction that are visible in the model output.

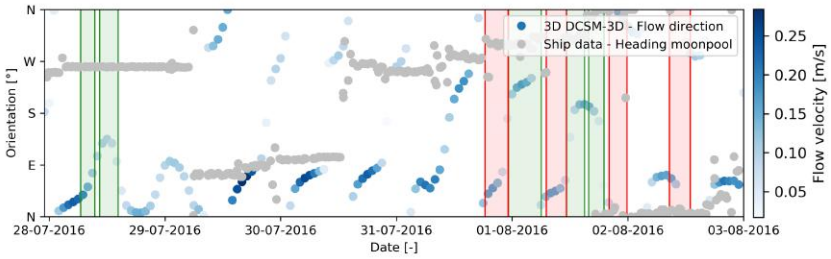

(a) Heading moonpool and flow velocity direction

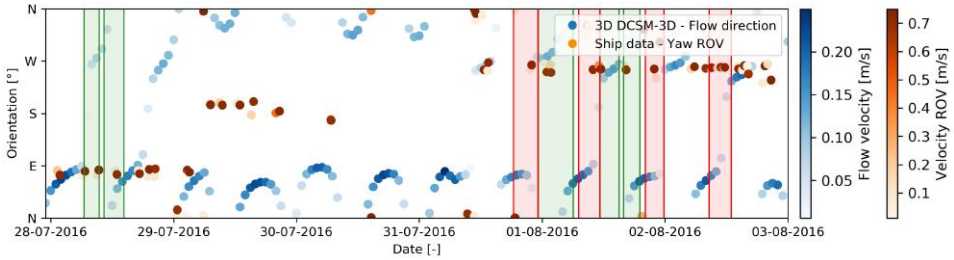

(b) Yaw ROV and flow velocity direction

Figure 6.2: Plot of the direction of the flow velocity in the top/bottom layer of the 3D DCSM-FM by Zijl et al. (2016) and (a) the heading of the moonpool [°] and (b) the yaw of the ROV [°] for Track N4. The magnitude of the flow velocity [m/s] is indicated by the blue colour bar, whereas the velocity of the ROV is represented by the orange colour bar. The green and red vertical lines represent the working and non-working intervals with a duration of at least 2% of the plotted time range. The downsampling rate of the variables is 30.

6.2. Deviation ROV

The deviation of the ROV, indicated by the distance between the moonpool and the centre of the ROV, is retrieved from the positional data of both objects. For Track S10, the results are depicted in Figure 6.3a. The path of the moonpool (vessel) and the ROV are identical, except for the part on the top left of the plot. This yellow curve indicates a malfunctioning of the measuring equipment as it is physically not possible to have a difference of multiple longitudinal degrees between the ROV and the vessel. Moreover, the vessel is sailing, as no green or red dots, indicating working and non-working intervals, are observed within this range.

In Figure 6.3b, a detailed view of one of the non-working intervals is displayed, indicated by the red dots. The exact distance in meters between the ROV (yellow dotted line) and the moonpool (black line) can be determined by means of the haversine function in Python. The results of this analysis are summarised in Table 6.1. The mean deviation during Track S10 is similar for working and non-working intervals, although the deviation is slightly larger for the working intervals. However, it was expected to observe larger values for non-working intervals than for working intervals. The maximum deviation during a working interval for Track S10 is 118 meters, which seems to be quite large. It might be possible that the sensors did not work properly at this moment in time.

Table 6.1: Overview of the mean and maximum deviation of the ROV [m] during working and non-working intervals for Track S10.

Deviation ROV [m]	**Mean**	**Max**
Working intervals (●)	15	118
Non-working intervals (●)	10	56

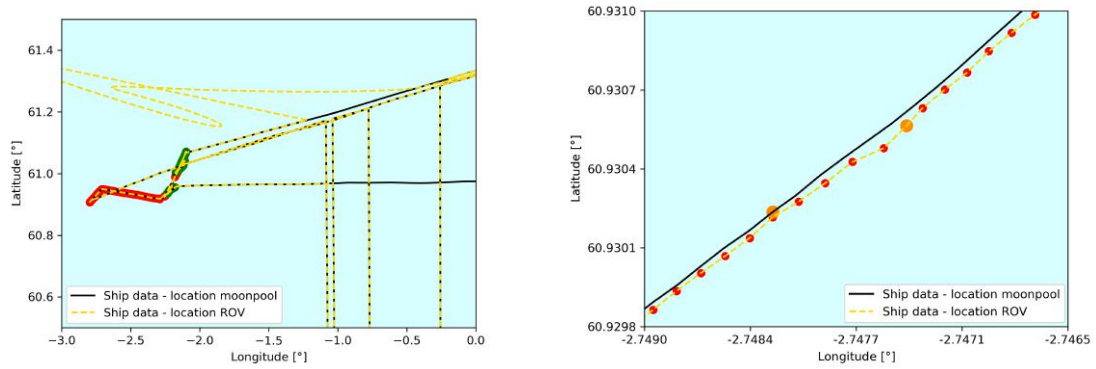

(a) Track S10

(b) Zoom of Track S10

Figure 6.3: Plot of the position of the moonpool (black) and the ROV (yellow) for (a) Track S10 and (b) a zoom of Track S10. In both figures, the green and red dots indicate working and non-working intervals, respectively. The orange dots represent the maximum distance between the ROV and the moonpool.

It was expected that the line distance across the moonpool and the pipeline, which is covered with rocks by an SRI vessel, and the line distance across the ROV and the pipeline are larger during non-working intervals than during working intervals, see Figure 6.4. In order to assess this hypothesis properly, scatter plots of these variables are depicted in Figure 6.5. From Figure 6.5a can be concluded that for both interval types a larger deviation of the moonpool is accompanied by a larger deviation of the ROV, as both correlation coefficients are close to a value of one (0.972 and 0.885, respectively). For the smaller distances between the objects, another pattern is observed, see Figure 6.5b. For working intervals, the distance between the moonpool and the pipeline is approximately twice the distance between the ROV and the pipeline. For the non-working intervals, the deviation of the ROV is two-thirds of the deviation of the moonpool. In conclusion, the correlation between both distances does not differ significantly for the working and non-working intervals.

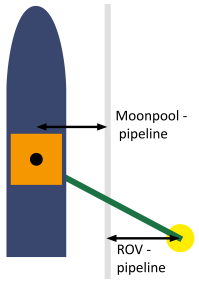

Figure 6.4: Schematic overview of the line distance across the moonpool and the pipeline and the deviation of the ROV. Figure not drawn to scale.

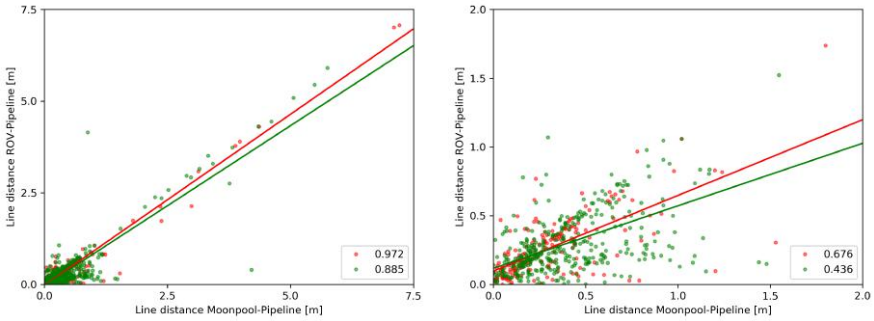

(a) Range 0.0 to 7.5 meter

(b) Range 0.0 to 2.0 meter

Figure 6.5: Scatter plot of the line distance across the moonpool and the pipeline versus the line distance across the ROV and the pipeline for a range of (a) 0.0 to 7.5 meters and (b) 0.0 to 2.0 meters. In both figures, the green and red dots indicate working and non-working intervals, respectively. The numbers in the bottom right corner indicate the correlation between both variables.

6.3. Velocity

While the ROV is working, the surrounding flow velocities are not yet measured in monitored, so this data is not available. In this section, the flow velocity in the bottom layer of the 3D DCSM-FM by Zijl et al. (2016), is compared to velocity of the ROV itself, resulting in the relative velocity of the ROV, see Figure 6.6. This figure illustrates the magnitude of the velocity of the ROV in both x and y-direction when the flow velocity is taken into account. It is expected that during non-working intervals, the velocity of the ROV and the flow velocity are oppositely directed, resulting in a small relative velocity. This hypothesis is assessed by plotting the three velocity variables over time for each track, see Figure 6.7, for example.

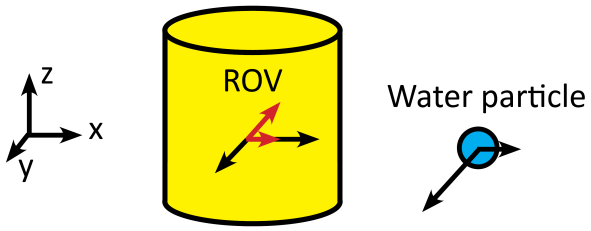

Figure 6.6: Example of the orientation of the velocity of the ROV and a water particle in both x and y-direction. The relative velocity of the ROV compared to the flow velocity is depicted in red. Figure not drawn to scale.

A couple of conclusions can be drawn from Figure 6.7. The flow velocity from the model is relatively constant and smooth over time, whereas the velocity of the ROV changes continuously. In general, the velocity of the ROV is larger than the flow velocity, which might have two possible explanations. First, the actual bottom flow velocities are not modelled correctly in the 3D DCSM-FM. This might be due to approximations in turbulence and bed stress. Secondly, the ROV is working in opposite direction of the flow, resulting in larger magnitudes. However, the directions of the velocity of the ROV and the flow velocity are similar for the plotted time range.

Regardless of the difference in magnitude of the flow velocity and the velocity of the ROV, no visual relation between these phenomena and the presence of a non-working interval can be found. Both for working and non-working intervals, the velocity of the ROV varies between 0 and 0.7 m/s, where one would expect larger velocities during a non-working interval.

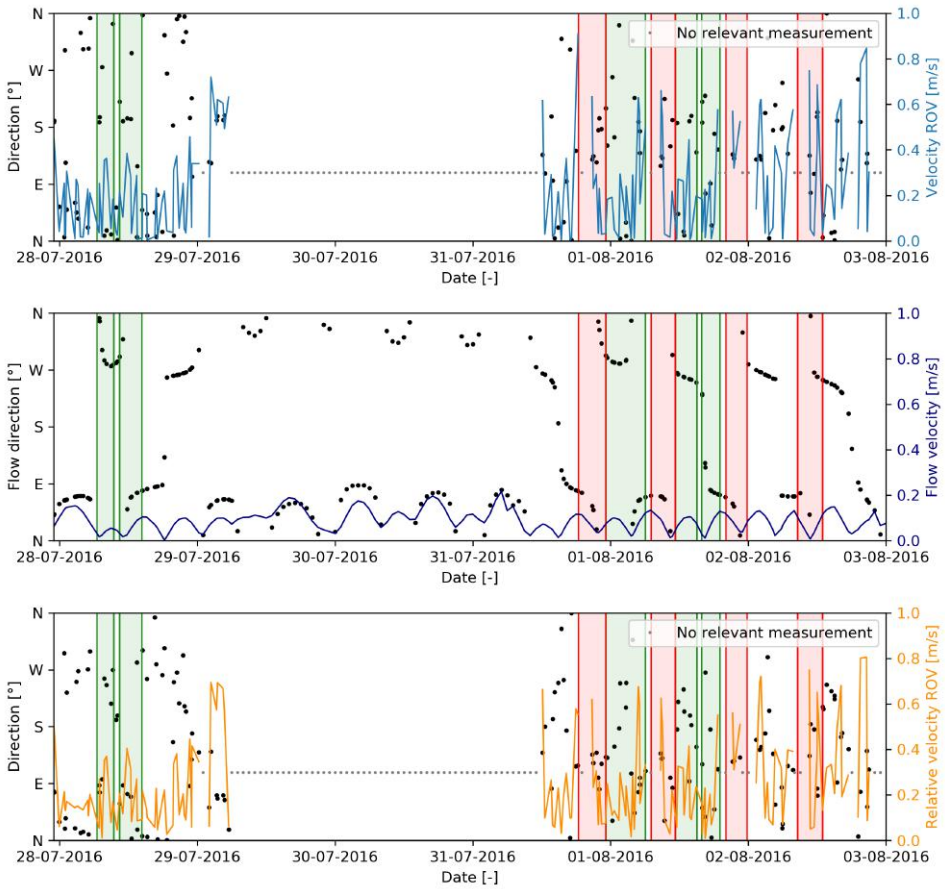

Figure 6.7: Plot of the velocity of the ROV [m/s],the flow velocity in the bottom layer [m/s] of the 3D DCSM-FM by Zijl et al. (2016) and the relative velocity of the ROV [m/s] for Track N4. The green and red vertical lines represent the working and non-working intervals with a duration of at least 2% of the plotted time range. A black dot indicates that the ROV is not launched or the ship is sailing. The downsampling rate of this variable is 30.

6.4. Horizontal power

The power of the thrusters of the ROV, needed during working activities, is monitored, but not logged and archived. Therefore, it has been chosen to compute the horizontal power from the measured acceleration of the ROV, based on a few assumptions. The horizontal power is obtained from a balance of three horizontal forces: the drag force of the water on the ROV, the force of the ROV on the water and the resulting force, see Figure 6.8. Equation 6.1 shows the resulting expression for the horizontal power. The details of the determination of the drag force of the water on the ROV can be found in Appendix B.

$$P_{\mathrm{ROV,h}} = (F_{\mathrm{D,ROV}} - m_{\mathrm{ROV}} \cdot a_{\mathrm{ROV}}) \cdot u_{\mathrm{ROV}} \tag{6.1}$$

Where:			
	$P_{\mathrm{ROV,h}}$	[W]	Horizontal power of the ROV
	a_{ROV}	[m/s^2]	Acceleration of the ROV
	u_{ROV}	[m/s]	Velocity of the ROV

The results of the computation of the horizontal power for Track S10 are depicted in Figure 6.9. The maximum horizontal power allocated during this track is approximately 30 kW, which is significantly lower than the available 4 x 75 kW. This difference might be caused by the simplifications of the computation of the horizontal power. Also the amount of vertical power used in the same time range is unknown. Overall, the power ranges from 0 to 10 kW during both working and non-working intervals.

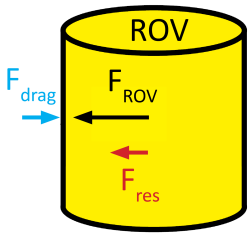

Figure 6.8: Horizontal balance of forces working on the ROV: drag force of the water (blue), the force of the ROV on the water (black) and the resulting force (red).

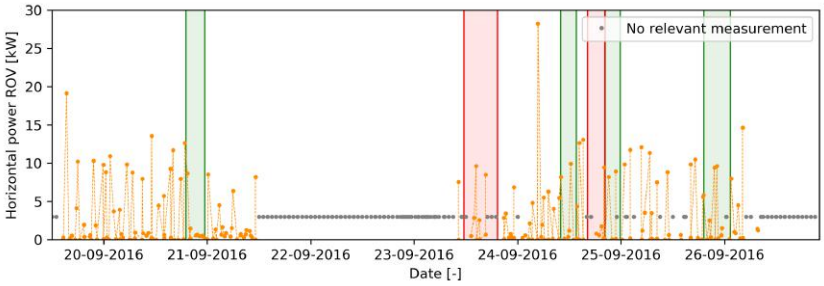

Figure 6.9: Plot of the horizontal power of the ROV [kW] computed from the measured acceleration for Track S10. The green and red vertical lines represent the working and non-working intervals with a duration of at least 2% of the plotted time range. A black dot indicates that the ROV is not launched or the ship is sailing. The downsampling rate of this variable is 30.

6.5. Motions of the ROV

During the rock installation activities, when the ROV is located close to the bottom of the sea, it is hardly ever hanging completely still. This makes sense, as it is slowly following the path of the pipeline and changes occur in the conditions of the surrounding water. For that reason, it is interesting to compare the rotation rate to the turbulent vertical eddy viscosity, see Figure 6.10.

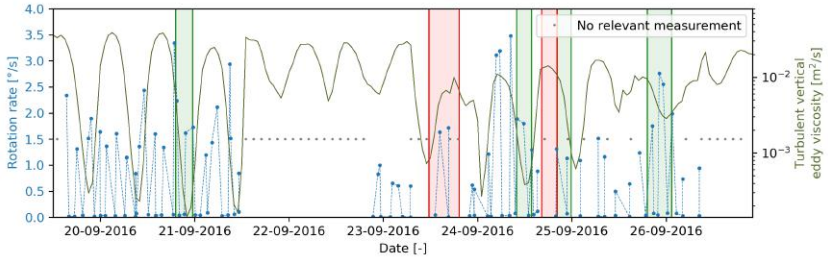

Figure 6.10: Plot of the rotation rate of the ROV [°/s] (blue) and the turbulent vertical eddy viscosity [m^2/s] in the bottom layer of the 3D DCSM-FM by Zijl et al. (2016) (dark green) for Track S10. The green and red vertical lines represent the working and non-working intervals with a duration of at least 2% of the plotted time range and the downsampling rate of this variable is 60.

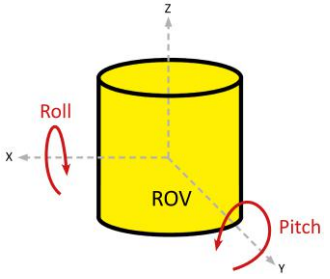

Figure 6.11: Orientation of the relevant motions of the ROV, which are roll [°] around the x-axis and pitch [°] around the y-axis.

The rotation rate is low when the ROV is standing on the moonpool, and varying from 1° to 3° when it is launched and working. During non-working intervals, the averaged rotation rate is slightly higher than the

rate during working intervals. This is in good correspondence with the expected patterns. However, no direct correlation is noticeable between the rotation rate and the turbulent vertical eddy viscosity in the bottom layer, where one would expect this based on theory.

The SRI vessels also log the motions of the ROV, such as the roll around the x-axis and the pitch around the y-axis, see Figure 6.11. The correlation between the turbulent vertical eddy viscosity (ν_{eddy}) in the bottom layer and both ship motions is quantified by means of a scatter plot, see Figure 6.12. In this plot data from both locations is assembled, as only logged data from Track S7 is available at Location 2. The major part of the red dots, which indicate non-working intervals, is located in the lower part of the graphs, representing a pitch or roll ranging from 0° to 2°. According to theory, a higher roll or pitch would lead to a more unstable position, which results in non-working conditions. Therefore, it was expected to find the red dots in the right part of the graphs. Since this is not the case, it can be concluded that the motions of the ROV are not considered to be the cause of the interruption of the working conditions.

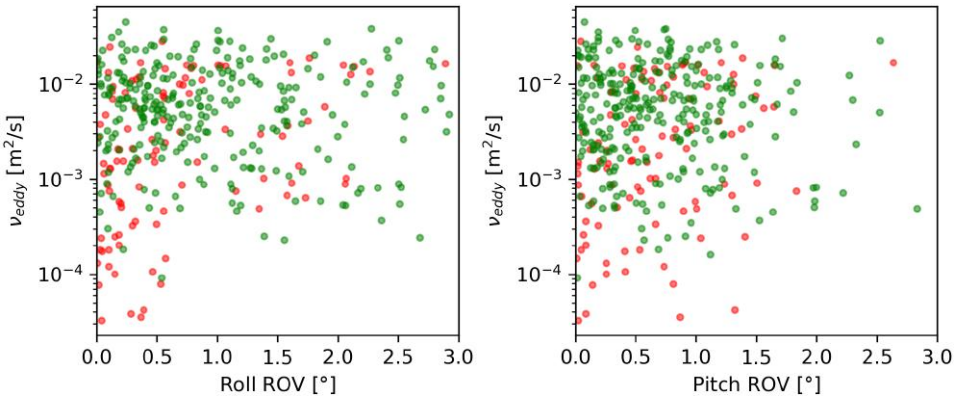

Figure 6.12: Scatter plot of the roll [°] (left) and pitch [°] (right) and the kinematic vertical eddy viscosity [m^2/s]. In both figures, the green and red dots indicate working and non-working intervals, respectively.

6.6. Conclusions

In this chapter, the vessel data from the Stornes and the Nordnes has been compared to the time ranges and locations of the working and non-working intervals. This is done for Track N4, N13, S7, S8, S9, S10 and S11 for five variables, namely the orientation, deviation, velocity, horizontal power and motions of the ROV. These variables are combined and or compared to data from the 3D DCSM-FM.

The analysis indicates that de average distance between the ROV and the moonpool, which is the launching platform of the ROV, is similar for working and non-working intervals. Moreover, the maximum deviation of the ROV is larger for working intervals. During working intervals, the distance between the moonpool and the pipeline is approximately twice the distance between the ROV and the pipeline. For the non-working intervals, the deviation of the ROV is two-thirds of the deviation of the moonpool. Scatter plots of the turbulent vertical eddy viscosity and the roll and the pitch of the ROV indicate that a high value of the pitch or roll (2°-3°) does not immediately lead to an interruption of the working conditions. Therefore, it is assumed that both the roll and the pitch of the ROV are not singularly responsible for the downtime of the SRI vessel. For the other variables, such as the velocity and the horizontal power, no clear correlation between the behaviour over time and the presence of a working or a non-working interval is found.

Chapter 7

Discussion

The objective of this research is to get a better understanding of the prevailing conditions in the ocean around the Shetland Islands in order to get more insight in the cause of the workability problems experienced by the SRI vessels. In this chapter, which is subdivided in sections, a discussion on the assumptions, simplifications and choices made in this study is provided.

Interpolation output 3D DCSM-FM

The 3D DCSM-FM by Zijl et al. (2016) provides output at predefined stations, which are equally spaced horizontally and vertically at 1/4° longitude and latitude, see Figure 7.1. In order to obtain continuous time series of the different variables included in the model output, the data is interpolated in space between the stations. This results in an approximation of the actual situation prevailing in the ocean around the Shetland Islands as the distance between two stations is roughly 33 kilometers. The approximation might lead to an incorrect interpretation of a correlation between two processes or phenomena, for example for the magnitude or direction of the flow velocity.

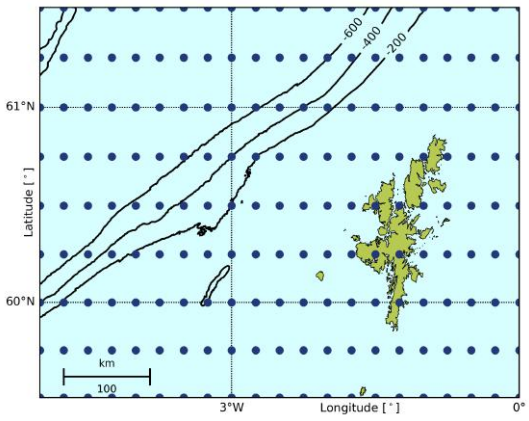

Figure 7.1: Overview of the locations of the output stations of the 3D DCSM-FM by Zijl et al. (2016), indicated by dark blue dots. The contour lines represent the depth of the ocean around the Shetland Islands.

Available bathymetry

The bathymetry of the 3D DCSM-FM is based on the database by EMODnet (2018), which consists of different depth profiles measured by ships and vessels. However, in the area west of the Shetland Islands and specifically at Location 1 and 2, no underlying measurements are available, indicated by the grey areas in Figure 7.2. This means that the bathymetry in this area is based on the General Bathymetric Chart of the Oceans (GEBCO), which is an approximation of the actual depth. It is highly possible that certain local topographic features and their influence on the ocean conditions are not taken into account in the analysis. The bathymetry is considered as a significant feature for the presence of the non-working intervals.

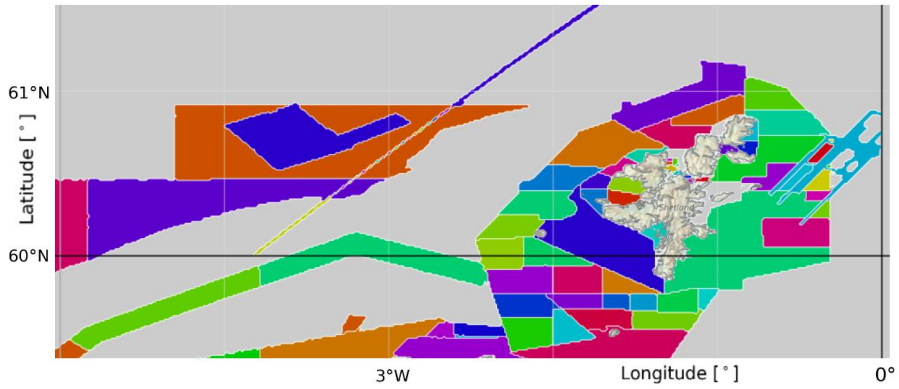

Figure 7.2: Overview of the data sources (depicted in colors) of the bathymetry in the area west of the Shetlands. Grey colors indicate that no measurements are available (adapted from EMODnet (2018)).

Baroclinic processes

As described in Section 3.2.3, certain hydrodynamic processes, such as the internal tide and internal waves, are not specifically included in the model, as the baroclinicity is not yet simulated correctly. This makes it difficult to assess the characteristics and the presence of these processes in the area around the Shetland Islands. As a result, their influence on or correlation with the appearance of the non-working intervals might be corrupted.

In Chapter 2, the characteristics of the internal tide around the Hawaiian Ridge were discussed. The phase and group velocity of the semi-diurnal tidal constituents are in the order of magnitude of 1.8 and 3.5 m/s, respectively, at that location. However, these velocities depend on four variables, the tidal frequency, the Coriolis parameter, the stratification and the depth, which have different values at the Hawaiian Ridge and the Shetland Islands. For example, the maximum depth in the area of interest west of the Shetland Islands is 600 meters, whereas the maximum depth in the vicinity of the Hawaiian Ridge is more than 5000 meters. For that reason, the exact magnitude of the internal tidal velocities can not be estimated directly from the article by Zhao (2017). However, their influence on the dynamic stability of the ROV is assumed to be significant.

Downsampling SRI vessel data

Chapter 6 elaborates on the analysis of the data, which is logged by the SRI vessels. Downsampling is applied to this data for plotting purposes, otherwise the plots would look 'grassy'. During this process of downsampling, the maximum and minimum value of a certain variable within a particular time range are selected. This time period has been calibrated by testing values between fifteen minutes and two hours. It turns out that a range of one hour results in clear plots. After the downsampling, the original patterns are not visible in the time series any more, see Figure 7.3. In the analysis of the vessel data, the presence of these underlying patterns is checked in two of the seven datasets, but the other five are not verified. Therefore, it might be possible that the downsampling process results in a different representation of certain variables.

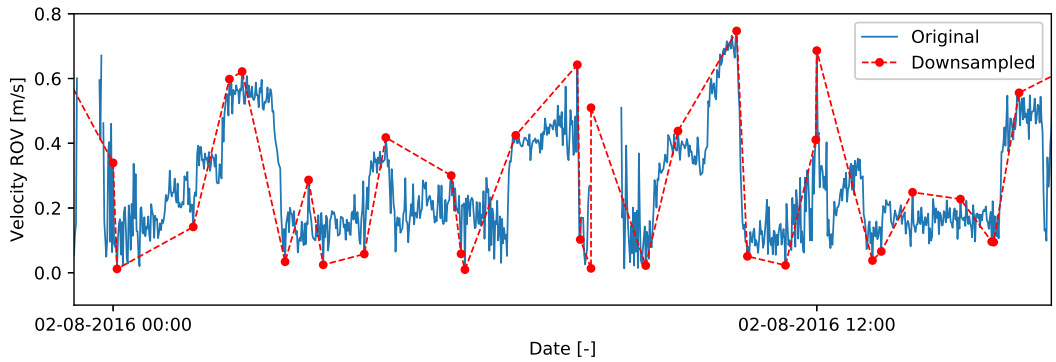

Figure 7.3: A plot of the original signal of the velocity of the ROV [m/s] (blue) and the downsampled time series (red dotted), over a range of approximately 12 hours.

Track selection

In Chapter 4, an overview of the time ranges (tracks) of the projects of Van Oord is presented. In total, 25 tracks of approximately one week are identified. However, only ten of these tracks are analysed in this study, as the time ranges are considered 'suitable', meaning one or more non-working intervals occurred within the time period and AIS data is available. By disregarding the remaining fifteen tracks, potential patterns or correlations can be overlooked.

Simplified force model

The theoretical model of the forces acting on the fallpipe-ROV combination, described in Appendix B, is simplified to make it suitable for a short analysis. One of the main assumptions in this model is the shape of the fallpipe, which is considered to consist of one rigid cylinder instead of a sequence of independent buckets. Moreover, the fallpipe is assumed to be empty, whereas the presence of rocks will result in additional mass and might possibly cause extra forces due to the movement of the rocks through the fallpipe. A third aspect, which was not considered in the simplified model, is the presence of turbulence in the water column and the influence of this phenomenon on the ROV and the fallpipe. This might compromise the dynamic position of both objects in relation to the pipeline and therefore require additional power, which is an extra force. An extra force means a larger deviation from the moonpool and thus more power is required by the ROV.

Accuracy FFT

The conclusions regarding the presence of inertial and shelf waves in the area around the Shetland Islands are based on the results of the FFT analyses. This method for the identification of different tidal constituents is applied to the output of the 3D DCSM-FM by Zijl et al. (2016). A tidal component is selected as it strictly meets the requirements of that constituent. For example, an elevation must have a frequency of exactly $2.237 \cdot 10^{-5}$ to be considered as an M_2-constituent. The subtle differences, which occur as a result of this strict selection, are illustrated in Figure 7.4. The residual signal, which remains after the filtering of the tidal frequencies, might therefore still contain tidal movements.

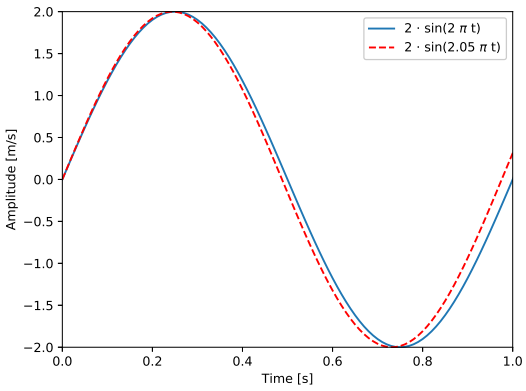

Figure 7.4: Plot of two sine functions with slightly different periods, indicating the difference between an elevation [m/s], which is characterised as a tidal constituent in an FFT (blue), and a movement that is not (red).

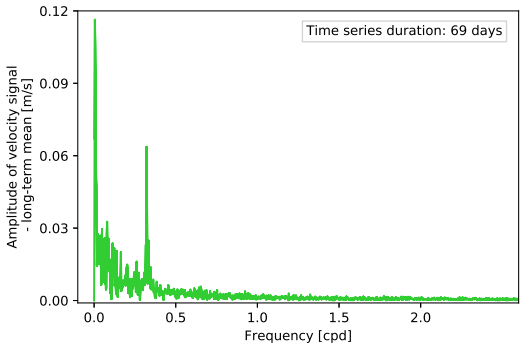

Figure 7.5: Zoom of the frequency spectrum of the flow velocity [m/s] from measurements by BODC (2018).

On the other hand, the output from the 3D DCSM-FM might not contain all physical processes, such as shelf waves, as the characteristic frequency of these waves is visible in spectra from other sources, see Figure 7.5. This spectrum is based on the flow velocity measurements at a depth of 150 meters by BODC (2018). A clear peak can be observed around 0.35 cpd, which is the characteristic frequency of shelf waves around the Shetland Islands. However, it should be noted that the duration of the underlying time series is 69 days, which is relatively short, compared to the output from the 3D DCSM-FM. Moreover, the spectrum does not indicate the presence of the diurnal and semi-diurnal tidal constituents, which makes the spectrum less reliable.

Chapter 8

Conclusions and recommendations

In this chapter the conclusions and recommendations of this study are described. Section 8.1 contains the conclusions, followed by the recommendations in Section 8.2.

8.1. Conclusions

The data analysis presented in this thesis has provided more insight in the prevailing conditions during the working and non-working intervals of the SRI vessels around the Shetland Islands. This has resulted in a better understanding and awareness of the potential causes of the interruption of the working activities of an SRI vessel.

The following six hydrodynamic processes my contribute to the presence of non-working intervals in the area around the Shetland Islands. The ocean gyre, called the NAC, which flows from south-west to north-east through the Faroe-Shetland Channel, is the largest observed phenomenon. In the North Sea, the dominant tidal constituent is the M_2-component, which is also governing for the internal tide. Furthermore, the four types of waves that might affect the workability of the SRI vessels are swell, internal waves, inertial waves and shelf waves. It is also possible that one or multiple of these processes occur in combination with one of the other processes. An example of such a combined process is seasonal circulation on the continental shelf or tidal mixing.

These processes have been assessed by analysing output from the hydrodynamic model of the Dutch Continental Shelf by Zijl et al. (2016). This is the most suitable model for the simulation of the oceanic conditions around the Shetland Islands as both tidal and baroclinic processes are included. Other ocean models simulate only one of these aspects. Moreover, the 3D DCSM-FM provides output on an interval of one hour and consists of twenty equidistant layers, which results in a proper representation of the entire water column. However, the inclusion of the baroclinic processes, such as the internal tide or internal waves, in the 3D DCSM-FM is not yet fully developed and correctly simulated in the area around the Shetland Islands. Therefore, it is impossible to properly assess the characteristics of the baroclinic processes in this area.

The data from the 3D DCSM-FM is combined with information from the DPRs and the AIS, in order to identify patterns in the appearance of the non-working intervals. From the analysis of the overview plots of the different tracks follow two correlations between variables and the presence of a non-working interval. First, in case the tidal flow is oriented to the east or east-northeast in the bottom part of the water column at Location 2, it is highly likely that the working activities are interrupted. This conclusion follows from a flow rose of the dataset. The rose indicates that tidal flow to the east results in non-working conditions in 100% of the cases, whereas tidal flow oriented to the east-northeast has a probability of 88%. Secondly, for values of the turbulent vertical eddy viscosity in the bottom layer of the water column higher than 10^{-2} m^2/s, the chance on non-working conditions at Location 2 increases significantly. The probability increases from 12% for a value of 0.01 m^2/s, to 39% for a value of 0.0146 m^2/s and 82% for a value of 0.028 m^2/s. A similar percentual distribution yields for the turbulent kinetic energy and the turbulent energy dissipation.

As the tide seems to play a significant role in the area around the Shetland Islands, the characteristics are quantified by an FFT of the flow velocities. The filtered tidal signal explains 80% of the variance, whereas the value for the residual signal is 20%. However, the amplitude of the residual flow velocity signal still has approximately the same value as the original signal. As the major part of the energy in the residual spectrum is centred around a frequency of 1.7 cpd it can be assumed that this frequency dominates the residual movement. This is most likely caused by the presence of inertial waves, which have a frequency of 1.72 cpd in the area of the Shetland Islands. Nevertheless, the residual flow velocity signal is relatively constant in time, so no correlation with the working or non-working intervals can be identified.

The logged SRI vessel data has been compared to the time ranges and locations of the working and non-working intervals. This is done for seven of the ten tracks for five different variables, namely the orientation, deviation, velocity, horizontal power and motions of the ROV. These variables are combined or compared to data from the 3D DCSM-FM. The analysis indicates that the average distance between the ROV and the moonpool, which is the launching platform of the ROV, is similar for working and non-working intervals. Moreover, the maximum deviation of the ROV is larger for working intervals. During working intervals, the distance between the moonpool and the pipeline is approximately twice the distance between the ROV and the pipeline. For the non-working intervals, the deviation of the ROV is two-thirds of the deviation of the moonpool.

Furthermore, scatter plots of the turbulent vertical eddy viscosity and both the roll and the pitch of the ROV indicate that a high value of the pitch or roll (2°-3°) does not immediately lead to an interruption of the working activities. Therefore, it is assumed that both the roll and the pitch of the ROV are not singularly responsible for the downtime of the SRI vessel. For the other variables, such as the velocity and the horizontal power, no clear correlation between the behaviour over time and the presence of a working or a non-working interval is found.

After different types of analysis are applied to the available data, the cause of the interruption of the working activities around the Shetland Islands could not be assigned to one specific hydrodynamic process. It is highly likely to be a combination of the tide and a baroclinic process, such as internal tide or internal waves. An alternative hypothesis is that the problems are caused by a combination of the hydrodynamic conditions and the characteristics of the SRI vessel and the fallpipe in particular. For example, the eigenfrequency of the fallpipe can be relevant, as oscillations might be induced by the (short) appearance of a hydrodynamic phenomenon.

8.2. Recommendations

The recommendations are split in two different categories, namely the recommendations for further research into this topic (Section 8.2.1) and the more 'practical' advices for Van Oord as a company, described in Section 8.2.2.

8.2.1. Further research

Validation of turbulent structures

Since the turbulent vertical eddy viscosity turns out to be correlated to the interruption of the working activities, it is interesting to study the behaviour over depth and time in more detail. The behaviour of this variable is linked to the tide, as can be observed in Figure 8.1. It will be interesting to validate the turbulent vertical eddy viscosity in the 3D DCSM-FM by means of a small size Delft3D model containing 1000 layers, for example. The flow velocity measurements by BODC (2018) or the values from the 3D DCSM-FM can be used as input for such a model. The results of the Delft3D model can be used to assess the turbulent structures in the 3D DCSM-FM as the software is calibrated on four advanced turbulence models (Deltares, 2016). Moreover, it will provide additional insight into the turbulent structures at the bottom specifically, since one layer will represent approximately half a meter of the water column instead of the 25 meters in the 3D DCSM-FM.

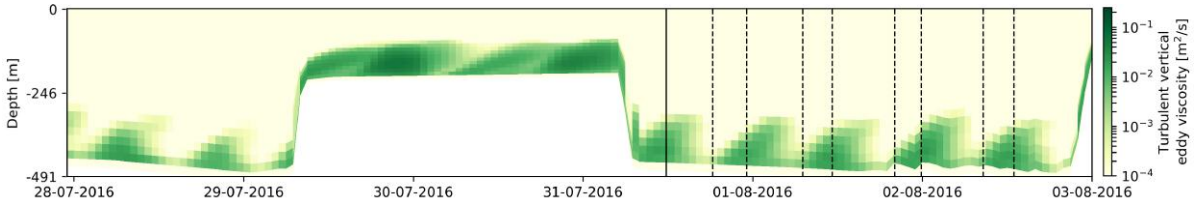

Figure 8.1: Colour plot of the turbulent vertical eddy viscosity [m^2/s] of Track N4 based on data from the 3D DCSM-FM by Zijl et al. (2016). The black lines indicate the start and end times of the non-working intervals.

Theoretical Ekman spiral

Chapter 4 describes the shear and veering profiles over the water column around the Shetland Islands. For these phenomena no correlation is found between the high values and the presence of a non-working interval. However, a difference in magnitude or direction of the flow remains a possible cause of the problems. Therefore, it is interesting to look into the dynamic Ekman spiral at the surface and bottom, which exists as a result of flow in the water column and the Coriolis force. In Figure 8.2, a theoretical surface Ekman spiral is depicted, which can, under certain conditions, extend until 140 meters in the water column (Pietrzak, 2014). This might affect the dynamic position of the fallpipe and the ROV and thus the working conditions. The article by Prandle (1982) describes a method for the determination of the vertical flow velocity profiles over depth. This method is based on two dimensionless parameters, which have the tidal frequency, vertical eddy viscosity and depth averaged flow velocity as main input variables. The vertical profiles that result from these computations can be used to compose the Ekman spiral at Location 1 and 2 around the Shetland Islands.

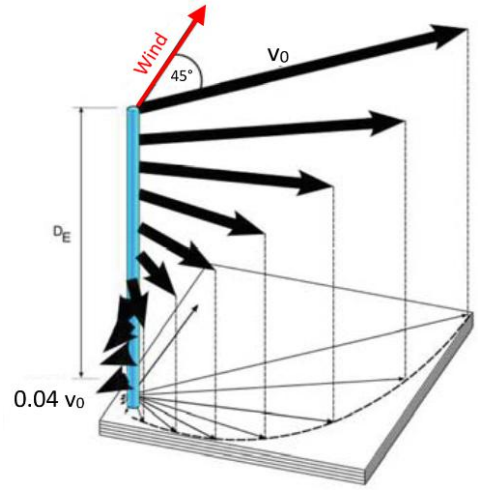

Figure 8.2: Theoretical profile of a surface Ekman spiral indicating the magnitude [m/s] and direction [°] of the flow velocity over depth as a result of the direction of the wind, adapted from Pietrzak (2014).

Workability analysis

In this study, the correlations between certain variables, which determine the oceanic conditions, have been identified by visual comparisons. In order to investigate these relations in more depth, it will be interesting to perform a workability analysis for the area around the Shetland Islands by means of logistic regression. This method determines for a certain variable, such as the flow velocity, flow direction or turbulent vertical eddy viscosity, whether working is possible (1) or impossible (0). Figure 8.3 contains an example of simplified logistic regression applied to the turbulent vertical eddy viscosity and the flow velocity. A detailed overview of the workability is obtained by combining the results of all the different variables that play a role in the determination of the working conditions. The logged data from the SRI vessels and output from the 3D DCSM-FM by Zijl et al. (2016) should be used for this analysis.

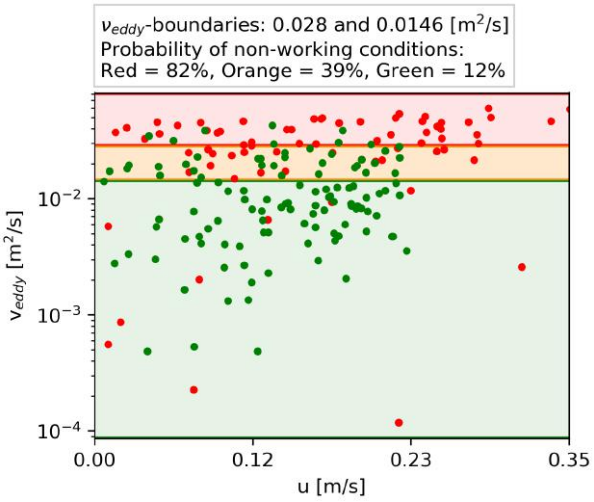

Figure 8.3: A simplified type of logistic regression applied to the relation between the turbulent vertical eddy viscosity [m^2/s] and the flow velocity [m/s] at Location 2 from the 3D DCSM-FM by Zijl et al. (2016).

Eigenfrequency of the fallpipe

Investigate the influence of Stokes Drift or swell waves on the orbital movement of the vessel-fallpipe combination. One of these hydrodynamic phenomena might induce a movement of the fallpipe with a frequency which is equal to the eigenfrequency of the fallpipe. Figure 8.4 depicts the theoretical eigenfrequencies of the fallpipe for different modes and a varying water depth. Appendix B contains the computations of these frequencies and the underlying assumptions. The lines in Figure 8.4 indicate that the eigenfrequency of the fallpipe varies significantly over depth. A dynamic model based on differential equations might proof whether or not the vessel-fallpipe combination is affected by hydrodynamic phenomena.

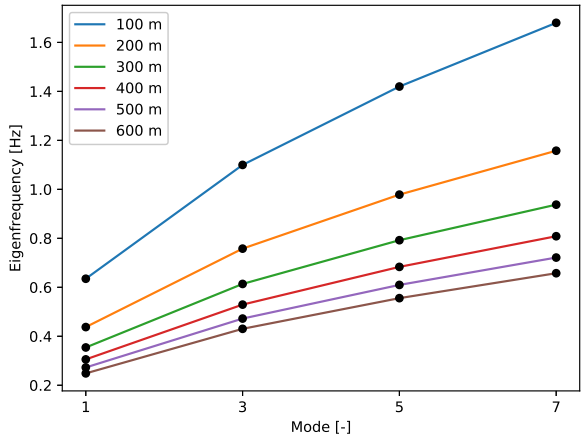

Figure 8.4: Plot of the theoretical eigenfrequency (f_0) [Hz] of the fallpipe for different modes and a varying water depth.

Alternative data sources

Investigate data sources, which are not used during this research, for additional model validation or a more complete picture of the ocean conditions. Three examples of these sources are the Nederlands Instituut voor Onderzoek der Zee (NIOZ), the Dutch Royal Marine or the National Oceanographic Center (NOC). The NIOZ, for example, filters the tide from their measurements, which can possibly emphasise other processes, such as the internal tide or internal waves.

Rotary spectrum analysis

Liu et al. analysed a dataset, containing thirty days of ADCP flow velocity measurements from the Yellow Sea, by applying the rotary spectrum method. This method generates a frequency spectrum similar to the one resulting from an FFT. However, the rotary spectrum takes into account the rotational rate and direction of

the flow velocity. It turns out that barotropic and baroclinic tidal currents rotate in ellipses, but in a different direction: counter-clockwise and clockwise, respectively (Liu et al., 2007). Moreover, Liu et al. proved that the bottom topography has a significant effect on the cross-isobath baroclinic motions. In case flow velocity measurements and a detailed local topography of the area around the Shetland Islands are available, this analysis could also be performed on that data. Potentially, this leads to new insights or correlations.

8.2.2. Van Oord

Working method SRI vessels

The analysis of the hydrodynamic data in relation to the working and non-working intervals at Location 2 shows that in case the water is flowing to the east or east-northeast, the chance on non-working conditions increases significantly. The variability of the flow direction is dominated by the tide in the area around the Shetland Islands. In order to avoid the adverse flow direction, which occurs twice a day, the current working method could de adapted. This new method is depicted in Figure 8.5, which shows to different phases within one tidal cycle.

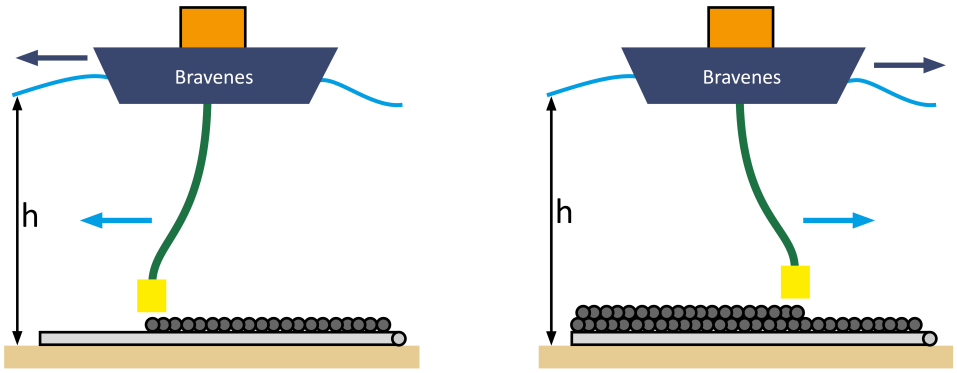

(a) Phase 1 (b) Phase 2

Figure 8.5: Schematic overview of (a) Phase 1 and (b) Phase 2 of a proposed working method for an SRI vessel. Figure not drawn to scale.

In the first phase, the flow is directed to the west, which does not cause problems for the SRI vessel, see Figure 8.5a. The thickness of the rock layer on top of the pipeline is half of the final thickness. During the second phase, the flow has changed direction and is now oriented to the east, see Figure 8.5b. Previously, this led to an interruption of the activities, as an SRI vessel has difficulties working in the opposite direction of the flow. Therefore, the vessel turns around and starts sailing to the east, as well. The second layer of rocks is now placed on top of the initial layer. After the second phase, the SRI vessel sails to a new pipeline section, where the cycle starts over. In general, the working direction is adapted to the flow direction, resulting in less downtime. It should be noted that the height and direction of the prevailing waves are not incorporated in this method.

ROV measuring equipment

For the collection of data from the area around the Shetland Islands, it will be useful to attach an ADCP to the ROV, store the data and send it to the office in Rotterdam or Gorinchem for analysis. In the ideal situation, one ADCP is measuring the area above the ROV and another one is measuring the area beneath the ROV. In this way, information from both the bottom layer and the lower part of the water column is collected. This can result in additional insight into the flow conditions during working and non-working intervals. Moreover, a Motion Reference Unit (MRU) can be connected to the middle of the fallpipe in order to measure the motions of the fallpipe.

Oceanic measuring equipment

In order to obtain flow velocity measurements throughout the water column in the area around the Shetland Islands, one can consider to deploy a drifting buoy in the Atlantic Ocean. This is an expensive investment, but in cooperation with other parties working in that area, it might be beneficial for future projects.

Bibliography

Andersson, M., Orvik, K., Lacasce, J., Koszalka, I., and Mauritzen, C. Variability of the Norwegian Atlantic Current and associated eddy field from surface drifters. *Journal of Geophysical Research: Oceans*, 116(8): 1–16, 2011.

Apel, J. Principles of Ocean Physics. *Academic Press*, 1987.

Beer, T. Environmental Oceanography. *CRC Press*, 1997.

Berx, B., Hansen, B., and Osterhus, S. Is the Transport of Atlantic Water in the Faroe Shetland Channel changing? - A summary of 20 years of observations. *Ocean Science*, 9:639–654, 2013.

Blaas, M. and de Swart, H. Vertical structure of residual slope circulation driven by JEBAR and tides: An idealised model. *Continental Shelf Research*, 22(18-19):2687–2706, 2002.

BODC. Metadata Report for BODC Series. *British Oceanographic Data Centre*, 2018.

Bosboom, J. and Stive, M. Coastal Dynamics I - Lecture Notes CIE4305. *Delft University of Technology*, 2015.

Broadbridge, M. and Toumi, R. Deep Faroe-Shetland Channel Circulation. *Journal of Geophysical Research: Oceans*, 120:5983–5996, 2015.

Charnock, H. Wind stress on a water surface. *Quarterly Journal of the Royal Meteorological Society*, 81(350): 639–640, 1955.

CMEMS. Atlantic-European North West Shelf - Ocean Physics Reanalysis from Metoffice (1985-2014). *Copernicus - Marine Environment Monitoring Service*, 2018.

Csanady, G. Ocean Currents over the Continental Slope. *Advances in Geophysics*, 30:95–203, 1988.

Cutchin, D. L. and Smith, R. L. Continental Shelf Waves: Low-Frequency Variations in Sea Level and Currents Over the Oregon Continental Shelf. *Journal of Physical Oceanography*, 3(1):73–82, 1973.

Deltares. Delft3D Flexible Mesh Suite - User Manual. *Deltares*, 2016.

EMODnet. Sea Level Measurements at Lerwick. *European Marine Observation and Data Network*, 2017.

EMODnet. Bathymetry - Understanding the topography of the European seas. *European Marine Observation and Data Network*, 2018.

Farrell, J. and Barth, M. The Global Positioning System and Inertial Navigation. *McGraw Hill Professional*, 1999.

Fu, L.-L. Observations and models of inertial waves in the deep ocean. *Massachusetts Institute of Technology*, 1980.

García Lafuente, J. and Lucaya, N. Inertial waves in the Ibiza Channel. *Journal of Marine Systems*, 5:445–459, 1994.

Gieskes, J., Culkin, F., and Fofonoff, N. Tenth Report of the Joint Panel on Oceanographic Tables and Standards. *Unesco*, 1981.

Gill, A. and Schumann, E. The Generation of Long Shelf Waves by the Wind. *Journal of Physical Oceanography*, 4:83–90, 1974.

Hansen, B. and Østerhus, S. Faroe Bank Channel Overflow 1995-2005. *Progress in Oceanography*, 75(4):817–856, 2007.

Holt, J. and Proctor, R. The seasonal circulation and volume transport on the northwest European continental shelf: A fine-resolution model study. *Journal of Geophysical Research: Oceans*, 113(6), 2008.

Holthuijsen, L. Waves in Oceanic and Coastal Waters. *Cambridge University Press*, 2007.

IADC. Facts about Subsea Rock Installation. *International Association of Dredging Companies*, 3:15–16, 2012.

Kinect. Production begins at two new gas fields off the coast of the Shetland Islands. *Kinect Energy Group*, 2017.

Kleptsova, O. Unstructured Orthogonal Meshes for Modeling Coastal and Ocean Flows. *Delft University of Technology*, 2013.

Kroon, A., van den Boomgaard, M., and van Leeuwen, B. Wave and Current Climate Orkney to Mainland Scotland - Along planned SSE cable route. *Svašek Hydraulics*, 2013.

Les, B. and Laukens, M. RTOFS surface current temperature and level forecast. *Svašek Hydraulics and MeteoGroup*, 2016.

Liu, Z., Hu, D., Tang, X., and Wei, E. Rotary spectrum analysis of tidal current in the southern Yellow Sea. *Chinese Journal of Oceanology and Limnology*, 25(3):286–291, 2007.

Longuet-Higgins, M. Double Kelvin waves with continuous depth profiles. *Journal of Fluid Mechanics*, 34: 49–80, 1968.

Molenaar, W. and Voorendt, M. Manual Hydraulic Structures. *Delft University of Technology*, 2016.

Mork, K. and Skagseth, Ø. A quantitative description of the Norwegian Atlantic Current by combining altimetry and hydrography. *Ocean Science*, 6(4):901–911, 2010.

Otto, L., Zimmerman, J., Furnes, G., Mork, M., Saetre, R., and Becker, G. Review of the physical oceanography of the North Sea. *Netherlands Journal of Sea Research*, 26(2-4):161–238, 1990.

Pearson. Monthy Tides – the Influence of the Sun and Moon. *Pearson Prentice Hall Incorporation*, 2004.

Pietrzak, J. An Introduction to Oceanography for Civil and Offshore Engineers. *Delft University of Technology*, 2014.

Pietrzak, J. Class Notes for CIE5302: An Introduction to Stratified Flows for Civil and Offshore Engineering. *Delft University of Technology*, 2015.

Prandle, D. The vertical structure of tidal currents and other oscillatory flows. *Continental Shelf Research*, 1 (2):191–207, 1982.

Qian, H., Shaw, P., and Ko, D. Generation of internal waves by barotropic tidal flow over a steep ridge. *Deep-Sea Research Part I: Oceanographic Research Papers*, 57(12):1521–1531, 2010.

Quante, M. and Colijn, F. North Sea Region Climate Change Assessment. *Regional Climate Studies*, 2016.

Ravelli, F. Improving the efficiency of a flexible fallpipe vessel: An experimental study on the spreading of rock in an impinging plane jet. *Delft University of Technology*, 2012.

Rodhe, J., Tett, P., and Wulf, F. The Baltic and the North Seas: a regional review of some important physical-chemical-biological interaction processes. *The Sea*, 14:1029–1072, 2004.

Sager, G. Fachbuckverslag. *Gezeiten und Schiffahrt*, 1959.

Schulz, W. J., Mied, R. P., and Snow, C. M. Continental Shelf Wave Propagation in the Mid-Atlantic Bight: A General Dispersion Relation. *Journal of Physical Oceanography*, 42(4):558–568, 2012.

Sherwin, T. Evidence of a deep internal tide in the Faroe-Shetland Channel. In: Tidal Hydrodynamics by B.B. Parker. *John Wiley and Sons, Inc.*, 1991.

Van Oord. Technical Details Stornes. *Van Oord Dredging and Marine Contractors*, 2015.

Van Oord. Equipment: Subsea Rock Installation Vessel - Bravenes. *Van Oord Dredging and Marine Contractors*, 2016.

Van Oord. Allernieuwste vloot van valpijpschepen. *Van Oord*, 2018.

Walters, R. A. and Heston, C. Removing Tidal-Period Variations from Time-Series Data Using Low-Pass Digital Filters. *Journal of Physical Oceanography*, 12(1):112–115, 1982.

Willis, A. The Ocean Floor, Continental Slope, Volcanic Island and Continental Shelf. *The Ocean Floor*, 2016.

Zhao, Z. Propagation of the Semidiurnal Internal Tide: Phase Velocity Versus Group Velocity. *Geophysical Research Letters*, 44(23):11,942–11,950, 2017.

Zijl, F., Verlaan, M., Gerritsen, H., and Sumihar, J. Hydrodynamic modeling on the Northwest European Shelf and North Sea: New opportunities with Delft3D Flexible Mesh. *Deltares*, 2016.

Zijl, F. and Veenstra, J. Setup and validation of 3D DCSM-FM. *Deltares*, 2018.

Zijl, F., Verlaan, M., and Gerritsen, H. Improved water-level forecasting for the Northwest European Shelf and North Sea through direct modelling of tide, surge and non-linear interaction. *Ocean Dynamics*, 63(7): 823–847, 2013.

Zijl, F., Sumihar, J., and Verlaan, M. Application of data assimilation for improved operational water level forecasting on the northwest European shelf and North Sea. *Ocean Dynamics*, 65(12):1699–1716, 2015.

Zou, S., Lozier, S., Zenk, W., Bower, A., and Johns, W. Observed and modeled pathways of the Iceland Scotland Overflow Water in the eastern North Atlantic. *Progress in Oceanography*, 159:211–222, 2017.

Appendix A

Background information SRI vessel

This appendix provides a description of the characteristics and the functioning of an SRI vessel of Van Oord. Figure A.1 depicts a general view of the Bravenes, whereas Figures A.2 and A.3 provide a side view and a top view of the vessel. Table A.1 summarises the specific properties of the Bravenes, such as deadweight, total installed power and the installation modus.

Figure A.1: Subsea Rock Installation vessel owned by Van Oord, called the Bravenes (Van Oord, 2016).

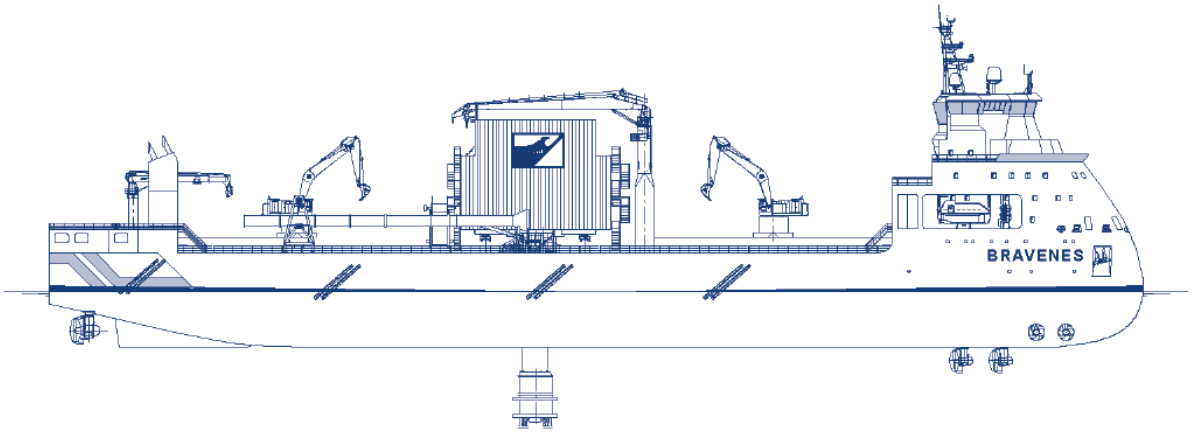

Figure A.2: Side view of the Bravenes, indicating two cranes and the fallpipe tower in the middle (Van Oord, 2016).

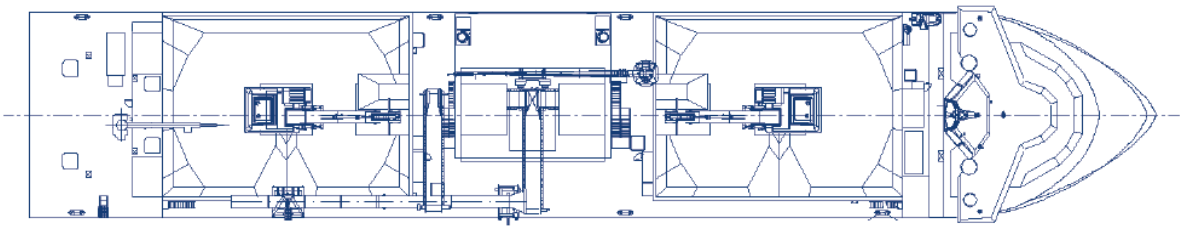

Figure A.3: Top view of the Bravenes, indicating two storage areas located next to the fallpipe tower (Van Oord, 2016).

Table A.1: Specific properties of the Bravenes (Van Oord, 2016).

	Properties	
Name	Bravenes	
Type	Subsea Rock Installation vessel	
Classification	Bureau Veritas	
Year of construction	2017	
Dimensions	Length overall	154.40 m
	Breadth moulded	28.00 m
	Moulded depth	13.30 m
	Draught	8.00 m
Deadweight	15,500 tons	
Speed loaded	12 knots	
Propulsion	6,200 kW	
Bow thrusters	2 x 1,500 kW	
Retractable thrusters	2 x 2,000 kW	
Total power installed	16,394 kW	
Dynamic positioning	DP Class 3	
Accommodation	60 persons	
Bunkers	Heavy fuel oil	1,500 m^3
	Marine gas oil	500 m^3
	Fresh water	170 m^3
Flexible fallpipe	⊘ 1.5 m	
Remotely Operated Vehicle	At the end of the fallpipe	6 x 75 kW
Installation modus	Fallpipe through moonpool, fallpipe over the side, tremie over the side	
Installation depth	Up to 1,000 m	
Installation capacity	Up to 2,000 t/h	
Handling large track	Up to 500 kilograms	

Functioning vessel-fallpipe combination

Before the SRI vessel can start working at a project location, it has to sail to a quarry in order to load rocks in the storage areas aboard. As soon as the vessel arrives at the assigned section of the pipeline, where the rocks have to be dumped, the thrusters at the bow are activated. These thrusters make sure that the vessel can hold its dynamic position above the pipeline, as the speed during the working activities is approximately 0.07 m/s. The ROV is launched via the moonpool to perform a pre-survey, which is necessary to obtain information about the current status of the seabed and the pipeline. After that, the fallpipe, consisting of a sequence of buckets, is launched and the rocks are transported from the storage areas to the fallpipe by conveyor belts. Via the fallpipe the rocks land on the seabed, forming a protective layer on top of the pipeline. If the section of the pipeline is finished, the buckets are recovered and the ROV performs a post-survey, in order to double check whether or not the work is executed properly. The information in this section is obtained from printed matters published by Van Oord (2016).

Fallpipe composition

Figure A.4 and Table A.2 provide a visual overview and numbers regarding the composition of the flexible fallpipe when its working at a depth of 400 meters.

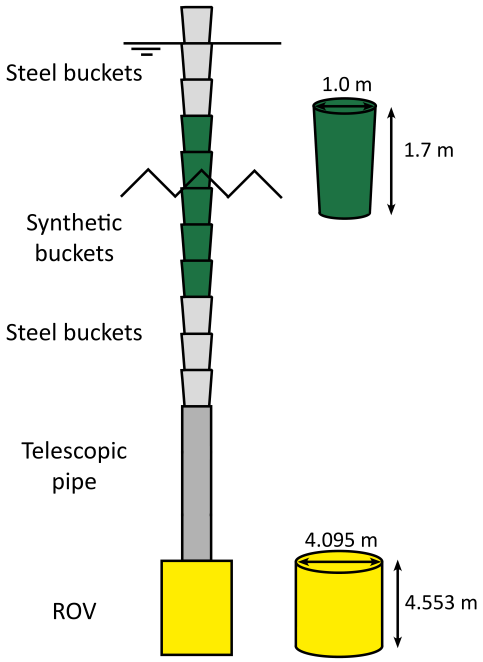

Figure A.4: The composition of a flexible fallipe system and the dimensions of a bucket and the ROV, adapted from Ravelli (2012). Figure not drawn to scale.

Table A.2: Overview of the amount and length of the different parts of the fallpipe for working at a depth of 400 meters (Van Oord, 2015).

Fallpipe setup (example)		
Name	**Number [-]**	**Length [m]**
Top steel buckets	10	8.3
Plastic buckets	140	242.0
Additional steel buckets	50	86.0
Bottom steel buckets	20	30.2
Telescopic pipe	1	10.5
ROV	1	4.0
Total		**381.0**

Appendix B

Theoretical characteristics of an SRI vessel

This appendix contains the details of the computation of two theoretical characteristics of an SRI vessel. In Section B.1, a simplified force model is set up to determine the horizontal distance between the moonpool and the ROV for various water depths and flow velocities. Section B.2 elaborates on the eigenfrequency of the fallpipe over depth.

B.1. Deviation of the ROV

The theoretical distance between the ROV and the moonpool ($d_{M,ROV}$) is obtained from a simplified force model, in which the fallpipe is considered as a solid cylinder. The following forces are included in the model: the gravitational force (F_Z), the buoyancy force (F_B) and the drag force (F_D), which is the force that is exerted by the flowing water on both the fallpipe and the ROV, see Figure B.1. The exact expressions of these forces are given in Equations B.1 to B.6 and Table B.1 contains the representative values of the parameters used in the formulas. The balance of the six forces around point M is considered for water depths varying from 0 to 600 meters and flow velocities ranging from 0 to 1 m/s. Furthermore, the density of the fallpipe is assumed to be identical to the density of the water and the angle between the moonpool and the fallpipe (α) is supposed to be small. Lastly, for these calculations, the bottom of the SRI vessel is assumed to be positioned on top of the water surface, see Figure B.1.

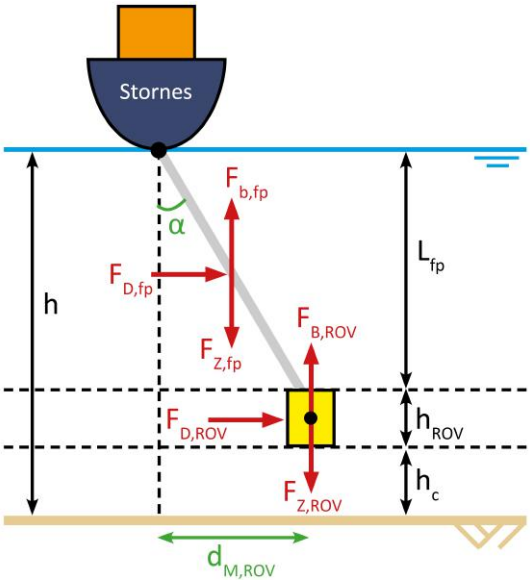

Figure B.1: Overview of the forces, depicted in red, which are part of the simplified force model of the distance between the moonpool and the ROV ($d_{M,ROV}$) [m]. The black lines indicate relevant dimensions. Figure not drawn to scale.

$$F_{Z,fp} = \rho_{fp} \cdot \frac{1}{4} \cdot d_{fp}^2 \cdot \pi \cdot L_{fp} \cdot g \tag{B.1}$$

$$F_{Z,ROV} = m_{ROV} \cdot g \tag{B.2}$$

$$F_{B,fp} = \rho_w \cdot \frac{1}{4} \cdot d_{fp}^2 \cdot \pi \cdot L_{fp} \cdot g \tag{B.3}$$

$$F_{B,ROV} = \rho_w \cdot \frac{1}{4} \cdot d_{ROV}^2 \cdot \pi \cdot h_{ROV} \cdot g \tag{B.4}$$

$$F_{D,fp} = \frac{1}{2} \cdot \rho_w \cdot u^2 \cdot C_{D,fp} \cdot L_{fp} \cdot d_{fp} \tag{B.5}$$

$$F_{D,ROV} = \frac{1}{2} \cdot \rho_w \cdot u^2 \cdot C_{D,ROV} \cdot h_{ROV} \cdot d_{ROV} \tag{B.6}$$

Where:			
	$F_{Z,fp}$	[N]	Gravity force on the fallpipe
	$F_{Z,ROV}$	[N]	Gravity force on the ROV
	$F_{B,fp}$	[N]	Buoyancy force on the fallpipe
	$F_{B,ROV}$	[N]	Buoyancy force on the ROV
	$F_{D,fp}$	[N]	Drag force on the fallpipe
	$F_{D,ROV}$	[N]	Drag force on the ROV
	ρ_{fp}	[kg/m^3]	Density of the fallpipe
	ρ_w	[kg/m^3]	Density of sea water
	d_{fp}	[m]	Diameter of the fallpipe
	L_{fp}	[m]	Length of the fallpipe
	g	[m/s^2]	Gravitational constant on Earth = 9.81
	m_{ROV}	[kg]	Mass of the ROV
	d_{ROV}	[m]	Diameter of the ROV
	h_{ROV}	[m]	Height of the ROV
	$C_{D,fp}$	[-]	Drag coefficient of the fallpipe
	$C_{D,ROV}$	[-]	Drag coefficient of the ROV

Table B.1: Overview of the magnitude of the parameters used in the computation of the deviation of the ROV ($d_{M,ROV}$).

Parameter	Unit	Magnitude
h_c	m	5.0
h_{ROV}	m	4.553
L_{fp}	m	h-h_c-h_{ROV}
d_{ROV}	m	4.095
d_{fp}	m	1.0
m_{ROV}	kg	17,000
ρ_w	kg/m^3	1,025
g	m/s^2	9.81

According to Molenaar and Voorendt (2016), the expression of the drag force contains a drag coefficient (C_D), which depends on the magnitude of the Reynolds number, and therefore on the flow velocity. The exact expression of the Reynolds number is given in Equation B.7. For both the fallpipe and the ROV, the drag coefficients are determined based on Figure B.2, see Tables B.2 and B.3. The deviation of the ROV is calculated for a varying drag coefficient, based on these tables, and for a constant drag coefficient of 0.6.

$$Re_{fp} = \frac{u \cdot d_{fp}}{\nu} \quad \text{or} \quad Re_{ROV} = \frac{u \cdot d_{ROV}}{\nu} \tag{B.7}$$

Where:			
	Re_{fp}	[-]	Reynolds number of the fallpipe
	Re_{ROV}	[-]	Reynolds number of the ROV
	ν	[m^2/s]	Kinematic eddy viscosity = 10^{-6}

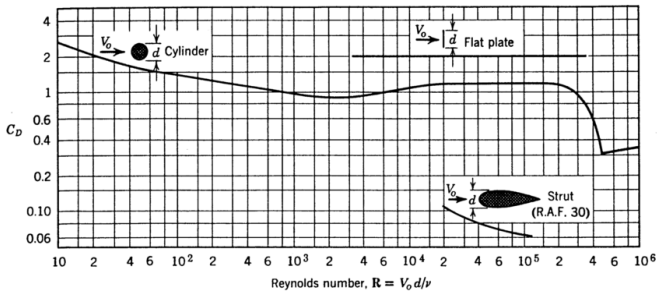

Figure B.2: Drag coefficient [-] of a flat plate, strut and cylinder for different values of the Reynolds number (Molenaar and Voorendt, 2016).

Table B.2: Assigned drag coefficients for the fallpipe based on Figure B.2.

Fallpipe	
Re	**C_D**
100,000	1.200
200,000	1.200
300,000	1.000
400,000	0.600
500,000	0.310
600,000	0.325
700,000	0.333
800,000	0.340
900,000	0.345
1,000,000	0.350

Table B.3: Assigned drag coefficients for the ROV based on Figure B.2.

ROV	
Re	**C_D**
400,000	0.600
500,000	0.310
600,000	0.325
700,000	0.333
800,000	0.340
900,000	0.345
1,000,000	0.350
2,000,000	0.353
3,000,000	0.355
4,000,000	0.357

Figure B.3a depicts the solution for a constant value of the drag coefficient, whereas the plot in Figure B.3b shows the theoretical lines for a varying drag coefficient. In both graphs, the dark blue line indicates the deviation of the ROV, which is used in practice, based on a rule of thumb. This rule prescribes a maximum horizontal distance that is equal to 10% of the water depth. Theoretically, working activities are possible as long as one is positioned on the left side of this line in the graph. It turns out that a constant drag coefficient results in a smaller 'safe' area, for which working activities can be performed properly. Therefore, this is the more conservative choice.

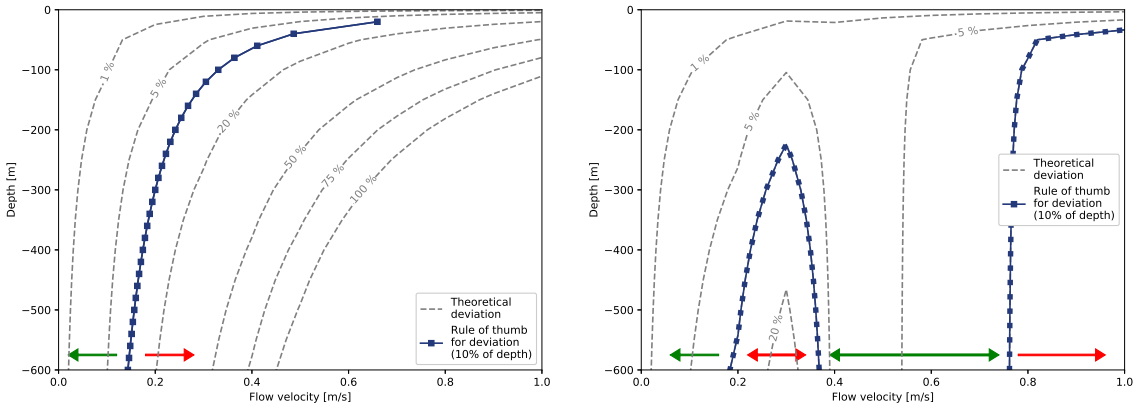

(a) Constant drag coefficient

(b) Varying drag coefficient

Figure B.3: Theoretical deviation of the ROV ($d_{M,ROV}$) as a percentage of the total water depth for different values of the water depth [m] and the flow velocity [m/s], in which the drag coefficient (a) remains constant and (b) varies with the magnitude of the flow velocity. The green arrow indicates the combinations of the water depth and the velocity for which working is possible, whereas the red arrow indicates the opposite.

B.2. Eigenfrequency of the fallpipe

A hydrodynamic process, such as swell, might unintentionally lead to an oscillation of the vessel-fallpipe combination. In case these movements have a frequency which is equal to the eigenfrequency of the fallpipe, damping does not play a role. Therefore, these frequencies might compromise the dynamic position of the fallpipe, and thus the ROV. In order to obtain more insight in the magnitude of these eigenfrequencies, the fallpipe is considered as a mass spring system with an extremely small bending stiffness. At the same time, the fallpipe is assumed to have the same behaviour as a simple gravity pendulum.

Theoretically, the fallpipe can bend into an unlimited amount of modes, as it is unbreakable. However, in this analysis only the first eight modes are considered, see Figure B.4. From this figure can be concluded that the ROV is not positioned straight beneath the vessel in the uneven modes. For these modes and a varying depth, the eigenfrequency (f_0) is computed based on Equations B.8 and B.9. The exact length of the fallpipe

depends on the depth, see Table B.1. As the mass of the fallpipe or the ROV is not included in these formulas, no distinction is made between working conditions and non-working conditions, as during the latter the buckets are filled with rocks.

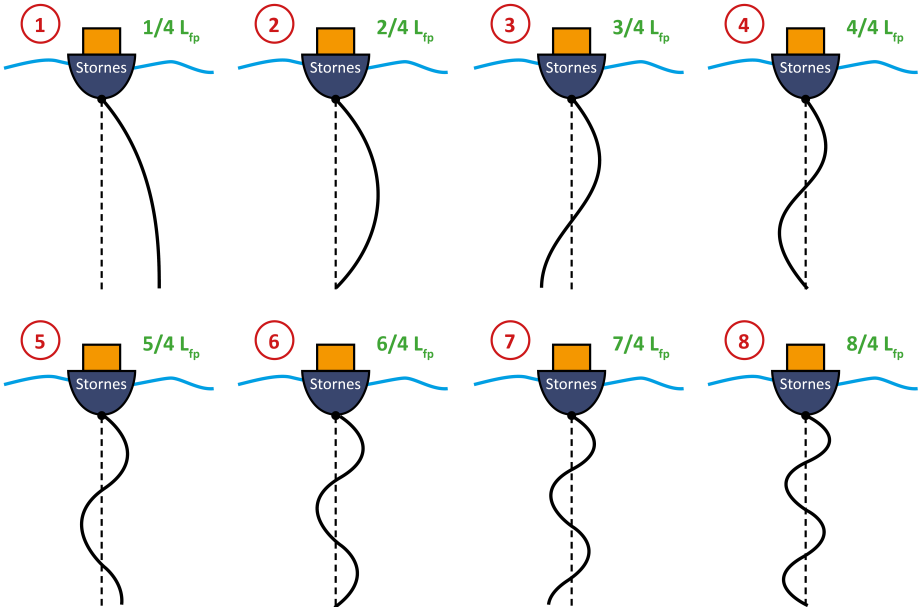

Figure B.4: Overview of the eight theoretical modes of the vessel-fallpipe combination, which can be induced by different flow conditions. Figure not drawn to scale.

$$f_0 = \frac{1}{T_0} \tag{B.8}$$

$$T_0 = 2\pi \cdot \sqrt{\frac{L_{\text{fp}}}{g}} \tag{B.9}$$

Where: f_0 [Hz] Eigenfrequency of the fallpipe
T_0 [s] Eigenperiod of the fallpipe

The results of these computations can be observed in Figure B.5. Since the eigenfrequency and eigenperiod are inversely proportional, a higher eigenperiod results in a lower eigenfrequency. For a depth varying from 100 to 600 meters, the eigenfrequency ranges from 0.01 to 0.07 Hz. This is smaller than the characteristic frequency of swell (0.1 Hz), for example.

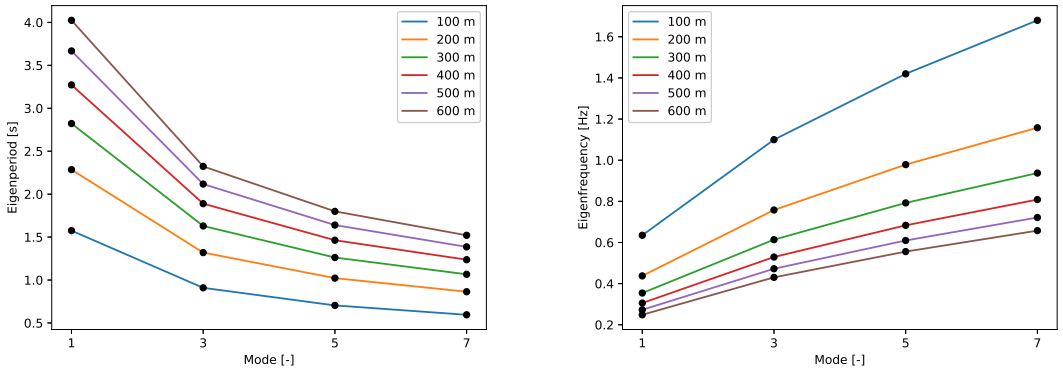

(a) Eigenperiod (T_0) (b) Eigenfrequency (f_0)

Figure B.5: Plot of (a) the eigenperiod (T_0) [s] and (b) the eigenfrequency (f_0) [Hz] of the fallpipe for different modes and a varying water depth.

Appendix C

Additional literature

This appendix contains additional literature for background on the topics discussed in Chapter 2. Section C.1 describes the general aspects of the tide and Section C.2 provides the formulas of the internal and external phase velocity. Also, the theoretical background of a Fast Fourier Transform (FFT) is explained in Section C.3.

C.1. Tides

The tide is prevailing in the major part of the water bodies on Earth, such as the North Sea, where it alters the coastline, mixes water masses and dissipates energy (Quante and Colijn, 2016). The existence of the tide is explained by Newton's 'Equilibrium Theory of Tides', in which the differential pull is identified as the tide-generating force (Bosboom and Stive, 2015). Differential pull results from the difference in gravitational pull, which is an attracting force, at every location on Earth. Before the net effect of gravitational pull is examined, the definition and characteristics of this phenomenon are discussed.

According to Bosboom and Stive (2015), gravitational pull consists of the centripetal forces of the Moon and the Sun on the water bodies at planet Earth. The centripetal force ensures the rotation of the Earth around the Moon. The magnitude of this pulling force on 1 kilogram mass of the Earth differs for the Sun and the Moon and is presented in Equation C.1. The magnitude and direction also vary over the locations on Earth due to a different angle to the centre of the Moon or the Sun, see Figure C.1a. As the Earth orbits the Sun, the gravitational pull is larger than the attracting force of the Moon. However, the contribution of the Moon to the actual tidal amplitude is larger than that of the Sun: 69% versus 31%.

$$a_S = G \cdot \frac{M_S}{{d_S}^2} = 6.0 \cdot 10^{-4} g \qquad a_M = G \cdot \frac{M_M}{{d_M}^2} = 3.4 \cdot 10^{-4} g \tag{C.1}$$

Where:	a_S	[m/s^2]	Gravitational pull of the Sun on 1 kg of mass of the Earth
	a_M	[m/s^2]	Gravitational pull of the Moon on 1 kg of mass of the Earth
	G	[Nm^2/kg]	Universal gravitational constant = $6.6 \cdot 10^{-11}$
	M_S	[kg]	Mass of the Sun = $1.99 \cdot 10^{30}$
	M_M	[kg]	Mass of the Moon = $7.35 \cdot 10^{22}$
	d_S	[km]	Distance between Sun and Earth = $150 \cdot 10^{6}$
	d_M	[km]	Distance between Earth and Moon = $384 \cdot 10^{3}$

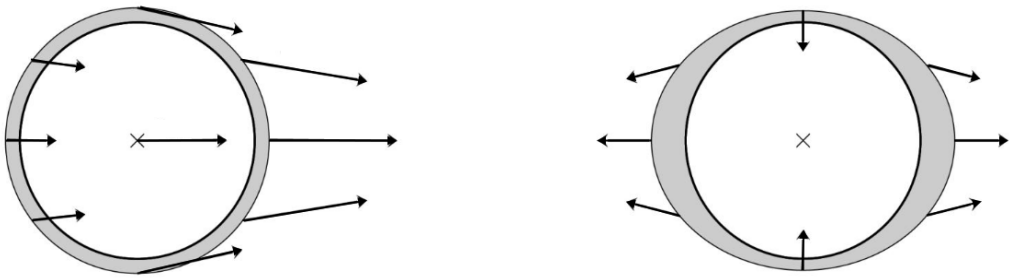

(a) Gravitational pull (b) Differential pull

Figure C.1: Attracting forces working on planet Earth: (a) gravitational pull and (b) differential pull, adapted from Bosboom and Stive (2015).

The dissimilarity in contribution to the tidal amplitude is caused by the difference in gravitational pull, called differential pull ($\Delta a = a_S - a_M$), as discussed before. As mentioned in the book by Bosboom and Stive (2015), this differential pull is proportional to M/d^3, so a larger distance between two planets will result in a smaller net attracting force. In the end, this results in the forces displayed in Figure C.1b, which have a normal and a tangential component. The normal components can be neglected, but the tangential forces shift the water to the outer sides of the planet, creating the shape of a rugby ball. The Earth rotates underneath the rugby ball, resulting in a semi-diurnal tide, consisting of two high and two low waters (Bosboom and Stive, 2015).

During a lunar month, the relative and absolute position of the Moon, Earth and Sun change. The actual location in relation to each other predominantly influences the tide. This results in two phenomena, called spring and neap tide, which are visually explained in Figure C.2. In fact spring tide means that for a new moon or a full moon, the tidal effect is reinforced, whereas for neap tide the Moon is at its first or third quarter and the impact is damped. The ratio between spring tide and neap tide can be 2.7:1 in open oceans (Bosboom and Stive, 2015).

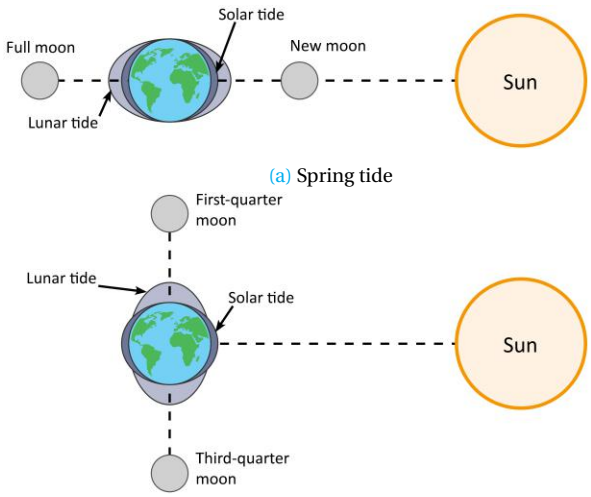

(a) Spring tide

(b) Neap tide

Figure C.2: Overview of the (a) spring and (b) neap mechanisms that occur both twice per lunar month, adapted from Pearson (2004).

The tide consists of multiple tidal constituents, indicated by a letter and a number, for example, M2. This code represents the influence of the Moon that occurs twice per day. There are several main diurnal, semi-diurnal and long-term constituents that contribute to the tidal amplitude. For a complete list of all tidal constituents the reader is referred to Apel (1987). The speed of the tide depends on the water depth, in case friction can be neglected. The formula that describes this relation is given in Equation C.2.

$$c = \sqrt{g \cdot h} \tag{C.2}$$

Where: c [m/s] Wave propagation speed

The last aspects of the tide that are discussed in this section are the effect of Coriolis and the presence of land masses on the tidal motion. Since the wave length of a tidal wave exceeds the threshold of a long wave, the effect of Coriolis cannot be neglected Bosboom and Stive (2015). Therefore, tidal waves are deflected to the right at the Northern Hemisphere and to the left at the Southern Hemisphere. The land masses of different continents block these deflections, resulting in rotating waves in ocean basins. Such a wave is part of a so-called amphidromic system consisting of nodes (zero vertical tide) and antinodes (maximum vertical tide). A node is also known as an amphidromic point.

C.2. Internal and external waves

Equations C.3 and C.4 represent the external and internal phase velocity, respectively. The physical meaning of the different parameters in these equations can be found in the left part of Figure 2.11a.

$$c_e = \frac{h_1 \cdot u_1 + h_2 \cdot u_2}{h} \pm \sqrt{g \cdot h} \tag{C.3}$$

$$c_i = \frac{h_1 \cdot u_2 + h_2 \cdot u_1}{h} \pm \sqrt{\frac{h_1 \cdot h_2}{h} \cdot [\epsilon g h - \Delta u^2]} \tag{C.4}$$

$$\epsilon_\rho = \frac{\rho_2 - \rho_1}{\rho_1} \tag{C.5}$$

Where:			
	c_e	[m/s]	Propagation speed of an external wave
	c_i	[m/s]	Propagation speed of an internal wave
	h_1	[m]	Water depth of the upper layer
	h_2	[m]	Water depth of the lower layer
	u_1	[m/s]	Flow velocity in the upper layer
	u_2	[m/s]	Flow velocity in the lower layer
	Δu	[m/s]	Difference in velocity between the upper and lower layer
	ϵ_ρ	[-]	Relative density difference
	ρ_1	[kg/m^3]	Density of the upper layer
	ρ_2	[kg/m^3]	Density of the lower layer

C.3. Theoretical background Fast Fourier Transform

As mentioned in Chapter 5, a Fast Fourier Transform (FFT) is a mathematical method, which filters frequencies from a recorded signal of the sea surface elevation or the flow velocity, for example (Holthuijsen, 2007). This is done by means of the two Fourier integrals, see Equation C.6 and C.7, applied to the flow velocity signal from the 3D DCSM-FM (Zijl et al., 2016). These integrals can be considered as filters, which remove the component with frequency i from the signal.

$$A_i = \frac{2}{D} \int \eta(t) \cdot \cos(2\pi \cdot f_i \cdot t) \mathrm{d}t \tag{C.6}$$

$$B_i = \frac{2}{D} \int \eta(t) \cdot \sin(2\pi \cdot f_i \cdot t) \mathrm{d}t \tag{C.7}$$

Where:			
	A_i	[m]	Amplitude of component i of the signal
	B_i	[m]	Amplitude of the component i of the signal
	D	[s]	Duration of the recorded signal
	$\eta(t)$	[m/s]	Recorded velocity signal
	f_i	[rad/s]	Frequency of component i of the signal
	t	[t]	Time of the recorded signal

Appendix D

Model characteristics 3D DCSM-FM

In the first section of this appendix, a general description of the 3D Dutch Continental Shelf Model (3D DCSM-FM) is provided. Section D.2 contains a list of model and user artifacts, which are phenomena that should be taken into account at any time, especially for the interpretation of the model results. Section D.3 describes the dataset, which was used during this study, whereas the last section contains the details of the ocean model by CMEMS (2018).

D.1. Model description

DCSM-FM is a 3D hydrodynamic model of the Dutch continental shelf, developed by Zijl et al. (2016) in order to increase the accuracy of water level forecasting in water bodies in the Netherlands. The model covers an area ranging from 43°N to 64°N and 15°W to 13°E, see Figure D.1. The grid cell sizes are uniform in east-west direction and in north-south direction (1/40° and 1/60° respectively). This is approximately equal to a grid cell size of one by one nautical mile, resulting in 10^6 computational cells. However, the grid resolution is increased for certain areas in the model, such as the Wadden Sea and Dutch estuaries. Other relevant features of the model are listed below and are retrieved from Zijl et al. (2013), Zijl et al. (2015) and Zijl and Veenstra (2018).

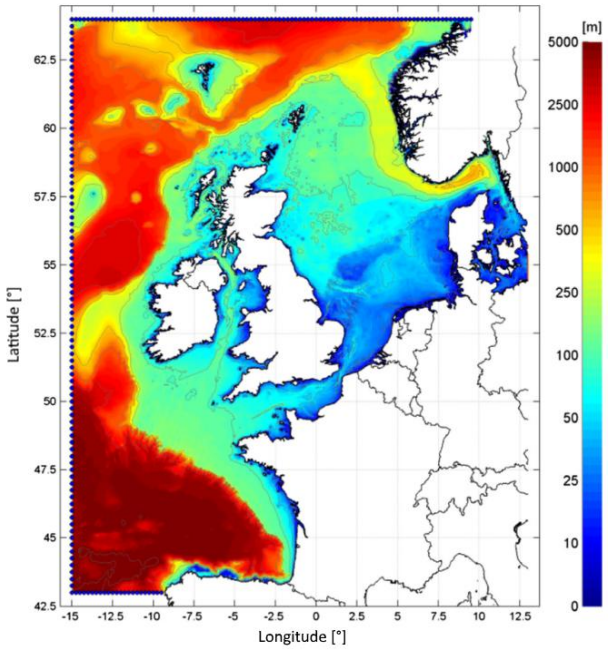

Figure D.1: Overview of the model area of the 3D DCSM-FM, containing the north-western part of the European continental shelf, adapted from Zijl et al. (2015).

- The model contains open water level boundaries, including 22 amplitudes and phases of harmonic constituents, located at the northern, western and southern side of the model domain;
- The wind speed and air pressure are retrieved from the Numerical Weather Prediction (NWP) and the High-Resolution Limited Area Model (HiRLAM);
- For the translation of the wind speed to surface stresses, the drag coefficient is computed using the Charnock formulation (Charnock, 1955). The Charnock coefficient is chosen to be 0.025, which is in line with the value used in the HiRLAM model;
- Baroclinicity is included in the model as the vertical dimension of the model consists of twenty equidistant σ-layers and a k-ϵ turbulence model is incorporated as well.

D.2. Model and user artifacts

Figures D.2a, D.2b and D.2c contain parts of the overview plot, discussed in Chapter 4. Each of these figures shows a model or user artifact (indicated by a red oval), which is an error in the representation of information. In this case, the model itself did not indicate an error in the processes, but as the output data is plotted, certain odd phenomena are observed. This should be kept in mind while interpreting the overview plots.

- **Model artifact 1** (Figure D.2a): transition from deep to shallow areas and vice versa. The magnitude of a variable, such as the salinity, differs systematically for deeper and shallower areas. In shallow areas, the water is relatively dense, as less convection and mixing takes place.
- **Model artifact 2** (Figure D.2b): non-hydrostaticity of the model. In the model, water can move through the water column, as the water depth is subdivided over twenty layers. At locations close to a (steep) ridge, more water is moved up than physically possible, resulting in non-realistic situations.
- **User Artifact 1** (Figure D.2c): appearance of unexpected values. Due to the application of interpolation in time and space to the dataset, the magnitude of certain variables is averaged or assigned to another location or moment in time. This results in unexpected (high) values in a certain layer, for example, the bottom layer.

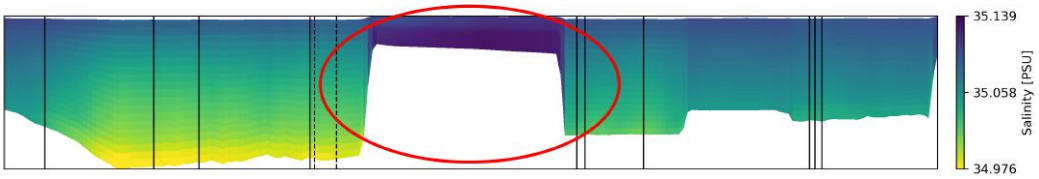

(a) **Model artifact 1**: transition from deep to shallow areas and vice versa. The salinity profile [PSU] over depth of Track S8.

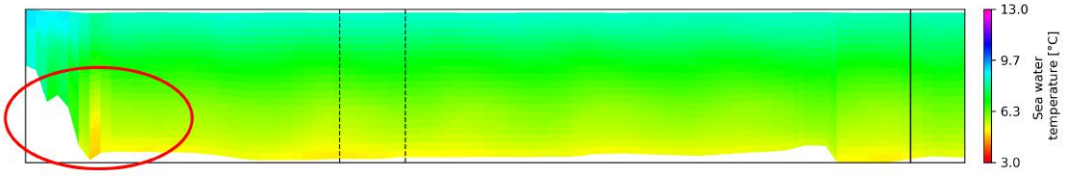

(b) **Model artifact 2**: non-hydrostaticity of the model. A depth profile of the sea water temperature [°C] of Track $S6_1$.

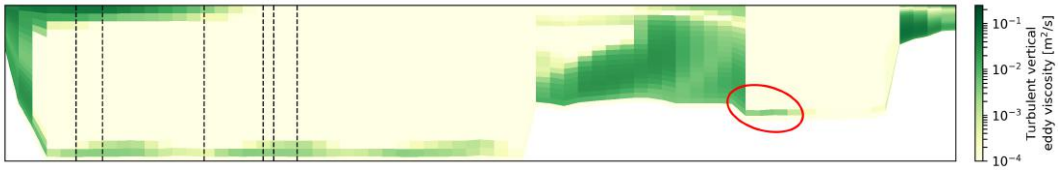

(c) **User artifact 1**: appearance of unexpected increasing values. A depth profile of the turbulent vertical eddy viscosity [m^2/s] of Track S11.

Figure D.2: Two model artifacts and one user artifact of the 3D DCSM-FM by Zijl et al. (2016). Time scales and depth profile information is not included in this figures.

D.3. Model dataset

The dataset, which is used in this study, consists of the 3D DCSM-FM output of a five year simulation, of which one year is considered as spin-up. The different variables are listed in Table D.1.

Table D.1: Characteristics of the dataset from the 3D DCSM-FM by Zijl et al. (2016), which was used in this study.

Variable	Unit
Atmospheric pressure	N/m^2
Bottom level	m
Flow velocity in x-direction	m/s
Flow velocity in y-direction	m/s
Flow velocity in z-direction	m/s
Salinity	PSU
Sea water temperature	°C
Station x-coordinate	°E
Station y-coordinate	°N
Time	Seconds since 22-12-2011
Turbulent energy dissipation	m^2/s^3
Turbulent kinetic energy	m^2/s^2
Turbulent vertical eddy viscosity	m^2/s
Vertical coordinate at centre layer	m above MSL
Vertical coordinate at layer interface	m above MSL
Water level	m above MSL
Wind in x-direction	m/s
Wind in y-direction	m/s

D.4. Ocean model by CMEMS (2018)

The data from CMEMS (2018) is a reanalysis of the Forecasting Ocean Assimilation Model, 7km Atlantic Margin Model and the Nucleus for European Modelling of the Ocean model code. The model is located on the Northwest European continental shelf, ranging from 40°N, 20°W to 65°N, 13°E (CMEMS, 2018). The grid is regular and the longitudinal resolution is 1/9° and the latitudinal resolution is 1/15°.

Appendix E

Details overview plots

This appendix contains detailed information of the overview plots discussed in Chapter 4. Section E.1 provides an explanation of the different aspects of the overview plot and Section E.2 contains the overview plot of each track individually.

E.1. Description overview plots

Figure 4.2 in Chapter 4 shows the overview for track N4 and the different aspects of this plot are described below by means of the matching numbers in the list.

1. A map of the area around the Shetland Islands, including contour lines of the depth and the path sailed by the vessel. An orange coloured dot indicates the location of the problems with the working activities, whereas the dark blue lines represent the remaining activities of the vessel.

2. The working schedule of the vessel during the track, where a distinction is made between working intervals (green), non-working intervals due to the conditions in the water column (red) and any other activity of the vessel (grey).

3. These graphs show the elevation of the water level (ζ) and the wind speed (u_w) over time. The wind speed consists of components both in x-direction and y-direction, see Equation E.1.

$$u_w = \sqrt{u_{w,x}^2 + u_{w,y}^2} \tag{E.1}$$

Where:

u_w	[m/s]	Wind speed
$u_{w,x}$	[m/s]	Wind speed in x-direction
$u_{w,y}$	[m/s]	Wind speed in y-direction

4. This is a colour plot of the magnitude of the flow velocity over depth and time, in which white tints indicate low flow velocities and red colours represent high flow velocities. The flow velocity consists of components both in x-direction and y-direction, see Equation E.2.

$$u = \sqrt{u_x^2 + u_y^2} \tag{E.2}$$

Where:

u_x	[m/s]	Flow velocity in x-direction
u_y	[m/s]	Flow velocity in y-direction

5. The direction of the flow is indicated by a colour plot of the four main wind directions: north, east, south and west. In case the flow direction is east, the water is flowing to the east.

6. The turbulent vertical eddy viscosity is plotted on a log-scale to indicate the difference between smaller values (10^{-4}) and larger values (10^{-2}), ranging from lighter yellow to green. These values represent regular flow situations and turbulent circumstances, respectively.

7. The density of the sea water around the track of the vessel near the Shetland Islands is based on the temperature of the sea water and the salinity. The relation between the temperature, salinity and density is called the Equation of State and for this colour plot, the one described by Gieskes et al. (1981) is used to calculate the density for each time step and every location over depth. The formulas for this Equation of State are given in Equations E.3 to E.6. The subscript zero in Equation E.3 represents the pressure of one standard atmosphere.

$$\rho_w = \rho_{w,0} + B \cdot S + C \cdot S^{3/2} + 4.8314 \cdot 10^{-4} S^2 \tag{E.3}$$

$$\rho_{w,0} = 999.842594 + 6.793952 \cdot 10^{-2} T + -9.095290 \cdot 10^{-3} T^2 + 1.001685 \cdot 10^{-4} T^3 + \\ - 1.120083 \cdot 10^{-6} T^4 + 6.536332 \cdot 10^{-9} T^5 \tag{E.4}$$

$$B = 8.24493 \cdot 10^{-1} + -4.0899 \cdot 10^{-3} T + 7.6438 \cdot 10^{-3} T^2 + -8.2467 \cdot 10^{-7} T^3 + 5.3875 \cdot 10^{-9} T^4 \tag{E.5}$$

$$C = -5.72466 \cdot 10^{-3} + 1.0227 \cdot 10^{-4} T + -1.6546 \cdot 10^{-6} T^2 \tag{E.6}$$

Where:

S	[PSU]	Salinity
T	[°C]	Sea water temperature
B	[kg/m^3]	Coefficient for the Equation of State
C	[kg/m^3]	Coefficient for the Equation of State

8. The Richardson number, given in Equation E.7, is a criterion for the stability of a fluid (Pietrzak, 2014). In case this number is larger than 1/4, the fluid is stable and stratified, whereas a value between 0 and 1/4 indicates an unstable fluid in which mixing processes take place. The scale of this colour plot is adapted to this range, to point out the unstable areas.

$$\mathrm{Ri} = -\frac{\frac{g}{\rho} \cdot \frac{\partial \rho_w}{\partial z}}{\left|\frac{\partial u}{\partial z}\right|^2} \tag{E.7}$$

Where:

z	[m]	depth

9. This plot represents the spring-neap cycle for a period of four months, including the time range of the vessel track. The elevation of the water level is measured at Lerwick, a station at the south east side of the Shetland Islands (EMODnet, 2017). The reference level for the sea level is Ordnance Datum.

10. These plots depict a depth profile averaged over time per non-working interval for the following four variables: flow velocity, flow direction, turbulent vertical eddy viscosity and the density.

11. The four legends contain clarifying information for the different plots.

E.2. Overview plot per track

This section contains a full-scale overview plot of each of the selected tracks (N4, N13, S4, S6$_1$, S6$_2$, S7, S8, S9, S10 and S11).

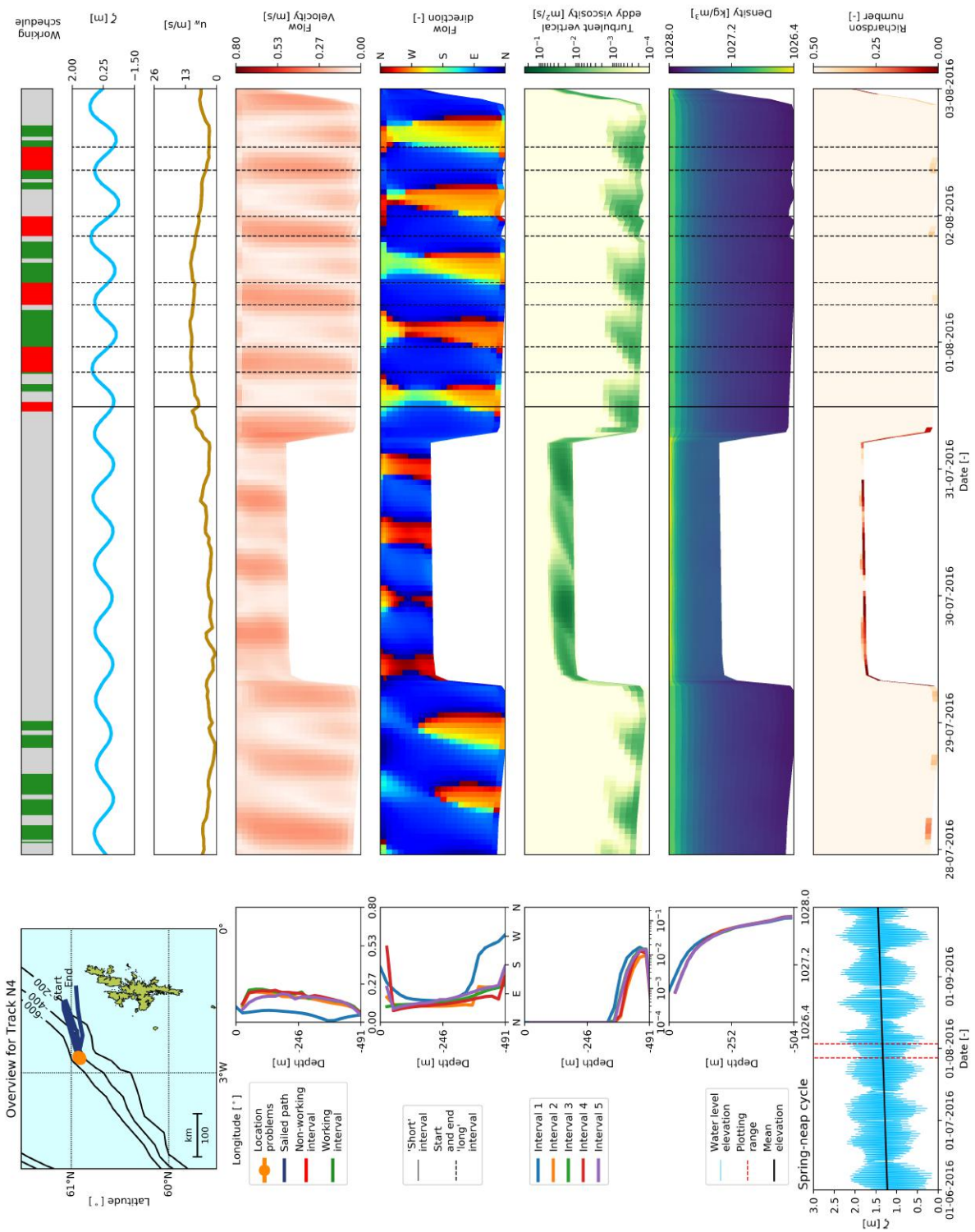

Figure E.1: Overview plot of the data from the 3D DCSM-FM by Zijl et al. (2016), combined with the data from the DPRs of the Nordnes for the period ranging from 28-07-2016 to 03-08-2016 (Track N4). In the upper left corner, a map of the area around the Shetland Islands is presented. The blue track represents the sailed path of the SRI vessel. On the right side a couple of variables are plotted over time. From top to bottom: the working schedule, the water level elevation [m], the wind speed [m/s], the flow velocity [m/s], the flow direction [-], the turbulent vertical eddy viscosity [m^2/s], the density [kg/m^3] and the Richardson number [-]. For the flow velocity, flow direction, turbulent vertical eddy viscosity and the density, a depth profile averaged over time per non-working interval is plotted on the left side of the figure. On the bottom left part, the water level elevation over four months, retrieved from EMODnet (2017), is plotted, indicating the spring-neap cycle.

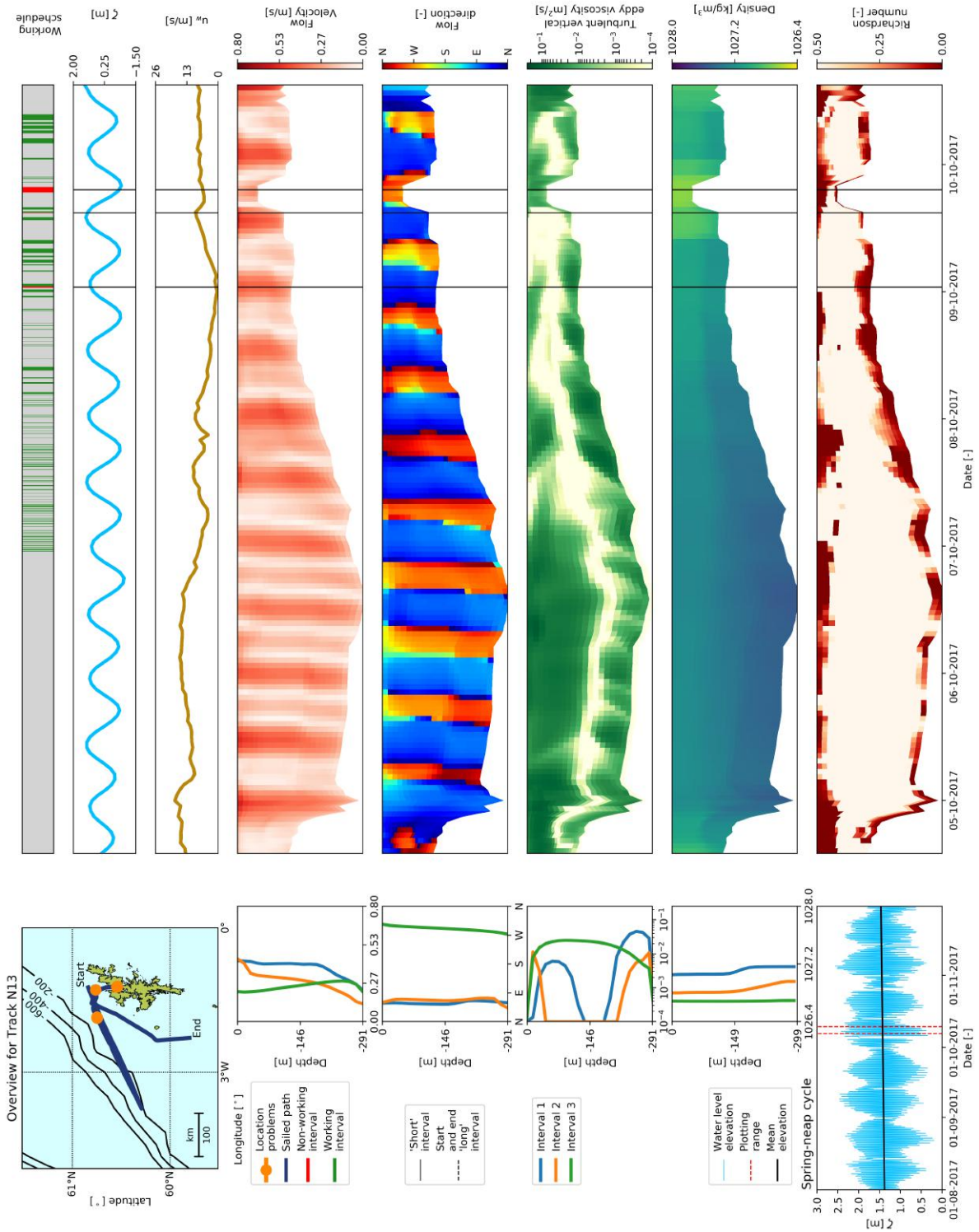

Figure E.2: Overview plot of the data from the 3D DCSM-FM by Zijl et al. (2016), combined with the data from the DPRs of the Nordnes for the period ranging from 05-10-2017 to 10-10-2017 (Track N13). In the upper left corner, a map of the area around the Shetland Islands is presented. The blue track represents the sailed path of the SRI vessel. On the right side a couple of variables are plotted over time. From top to bottom: the working schedule, the water level elevation [m], the wind speed [m/s], the flow velocity [m/s], the flow direction [-], the turbulent vertical eddy viscosity [m^2/s], the density [kg/m^3] and the Richardson number [-]. For the flow velocity, flow direction, turbulent vertical eddy viscosity and the density, a depth profile averaged over time per non-working interval is plotted on the left side of the figure. On the bottom left part, the water level elevation over four months, retrieved from EMODnet (2017), is plotted, indicating the spring-neap cycle.

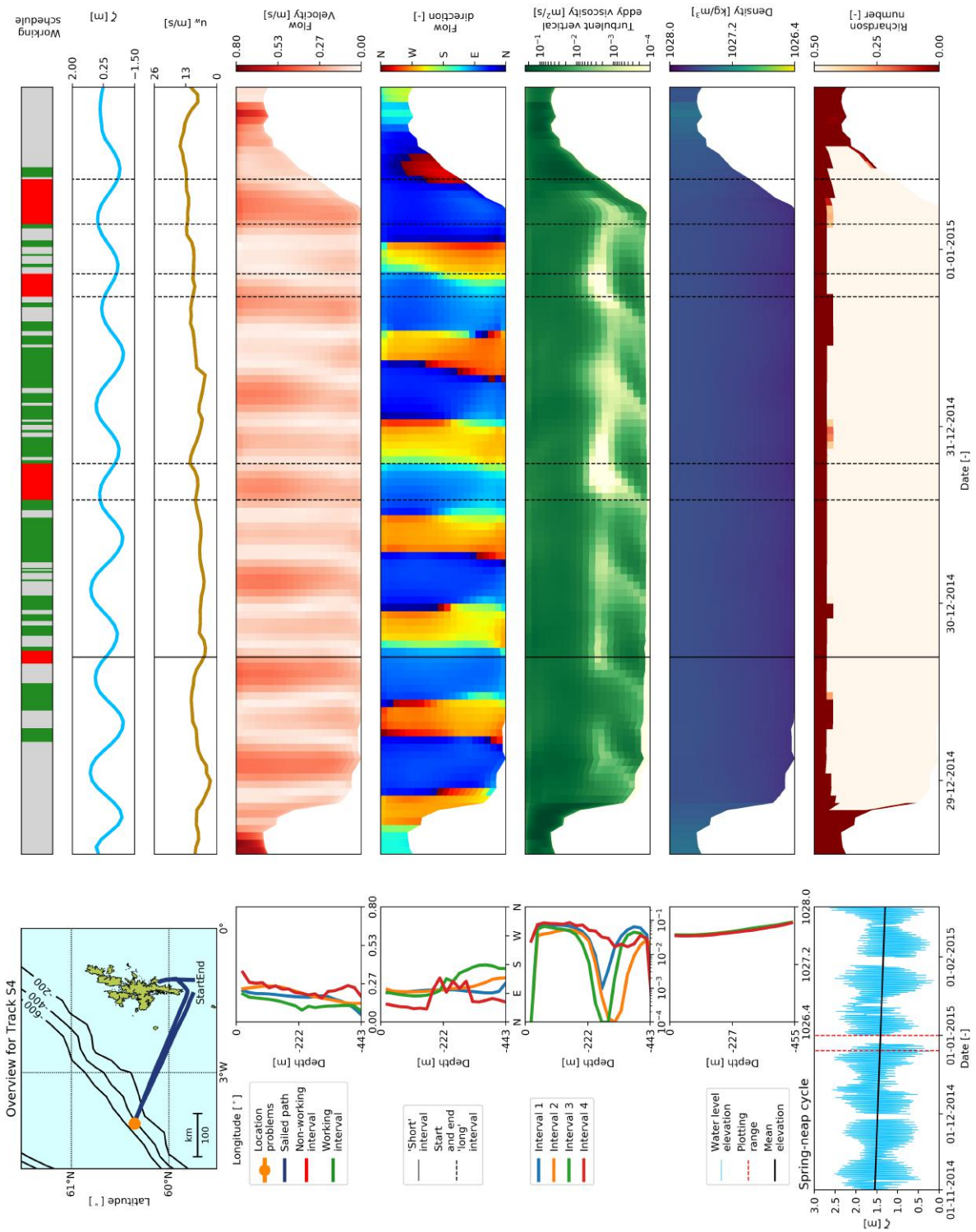

Figure E.3: Overview plot of the data from the 3D DCSM-FM by Zijl et al. (2016), combined with the data from the DPRs of the Nordnes for the period ranging from 29-12-2014 to 01-01-2015 (Track S4). In the upper left corner, a map of the area around the Shetland Islands is presented. The blue track represents the sailed path of the SRI vessel. On the right side a couple of variables are plotted over time. From top to bottom: the working schedule, the water level elevation [m], the wind speed [m/s], the flow velocity [m/s], the flow direction [-], the turbulent vertical eddy viscosity [m^2/s], the density [kg/m^3] and the Richardson number [-]. For the flow velocity, flow direction, turbulent vertical eddy viscosity and the density, a depth profile averaged over time per non-working interval is plotted on the left side of the figure. On the bottom left part, the water level elevation over four months, retrieved from EMODnet (2017), is plotted, indicating the spring-neap cycle.

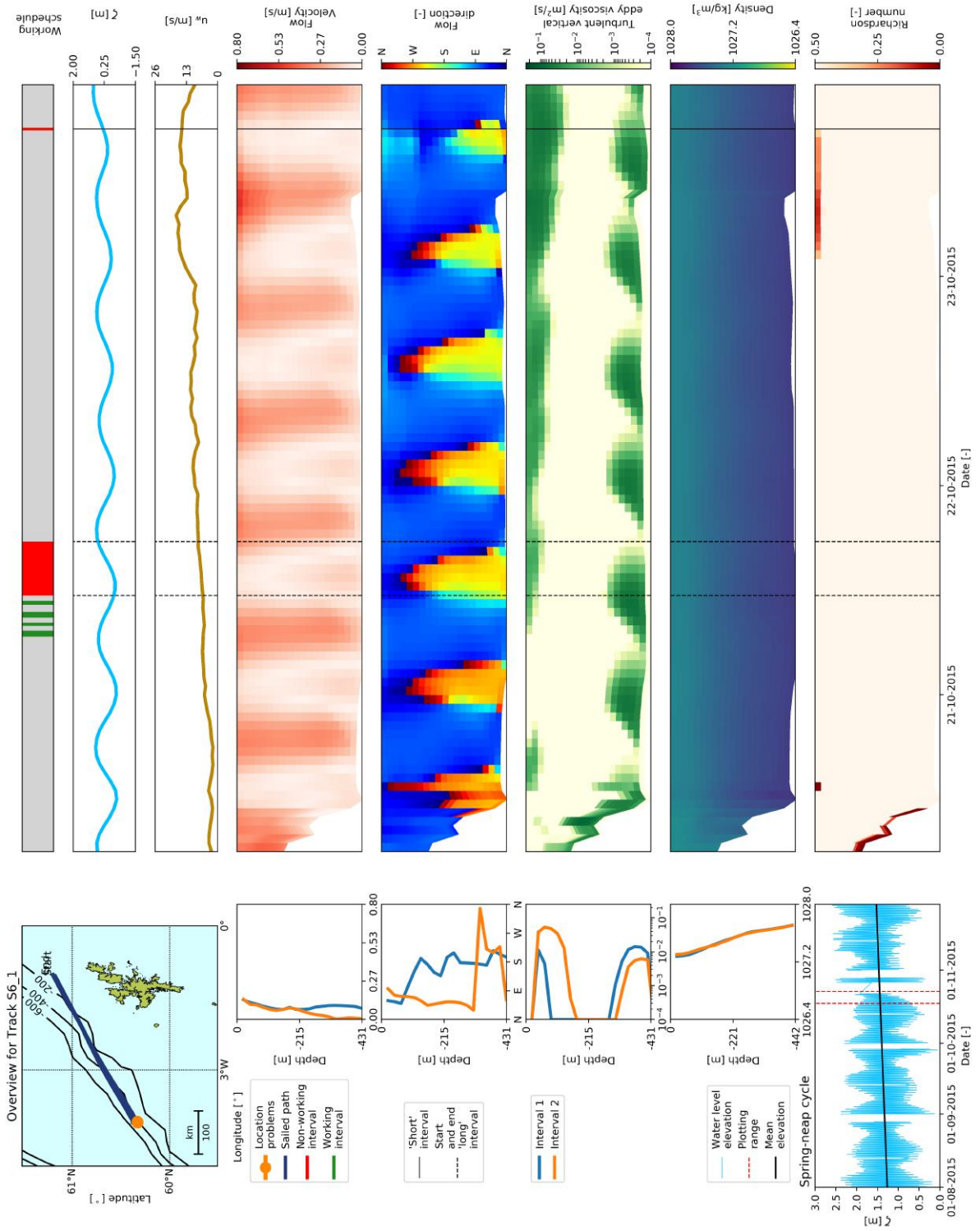

Figure E.4: Overview plot of the data from the 3D DCSM-FM by Zijl et al. (2016), combined with the data from the DPRs of the Nordnes for the period ranging from 21-10-2015 to 23-10-2015 (Track S6$_1$). In the upper left corner, a map of the area around the Shetland Islands is presented. The blue track represents the sailed path of the SRI vessel. On the right side a couple of variables are plotted over time. From top to bottom: the working schedule, the water level elevation [m], the wind speed [m/s], the flow velocity [m/s], the flow direction [-], the turbulent vertical eddy viscosity [m^2/s], the density [kg/m^3] and the Richardson number [-]. For the flow velocity, flow direction, turbulent vertical eddy viscosity and the density, a depth profile averaged over time per non-working interval is plotted on the left side of the figure. On the bottom left part, the water level elevation over four months, retrieved from EMODnet (2017), is plotted, indicating the spring-neap cycle.

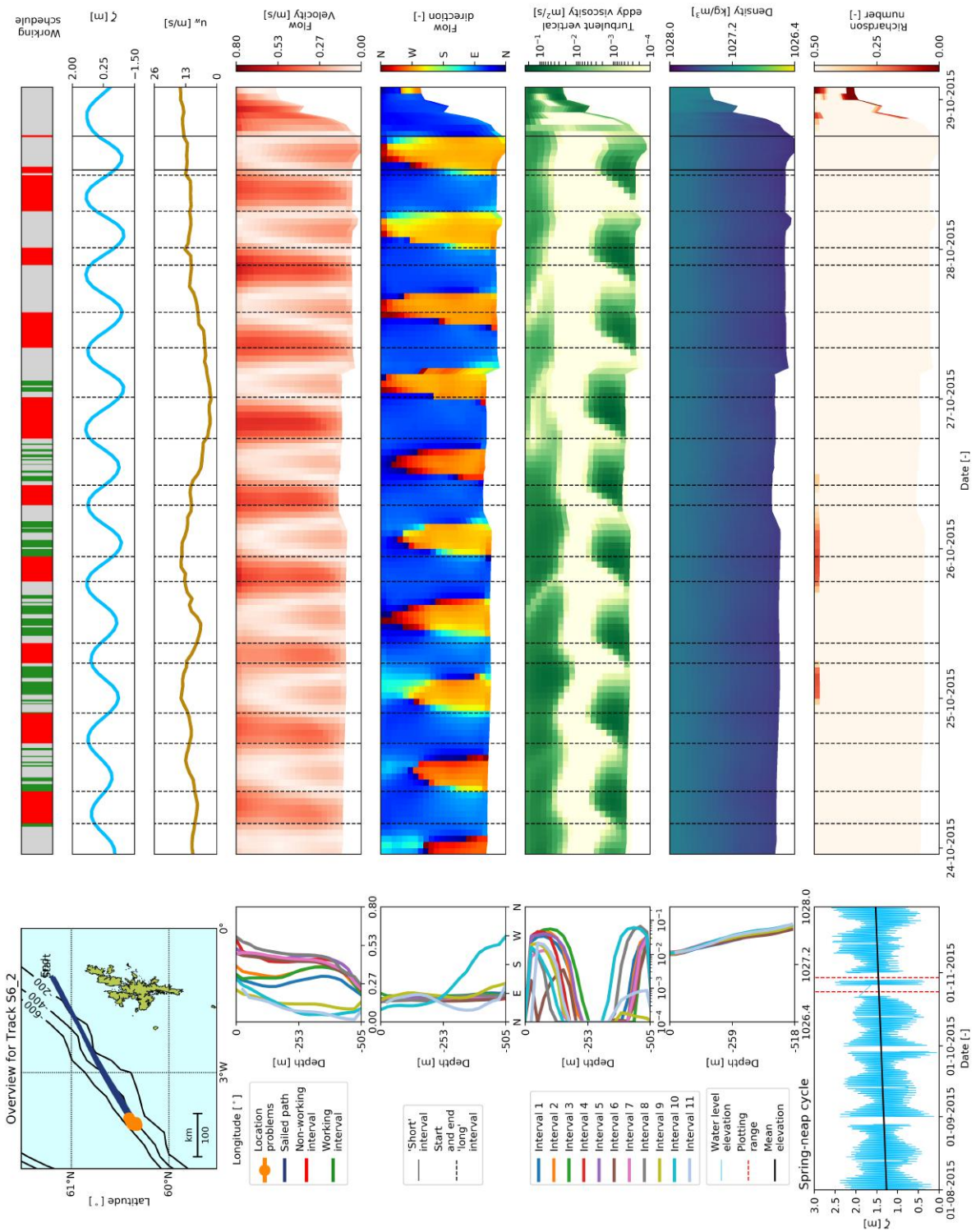

Figure E.5: Overview plot of the data from the 3D DCSM-FM by Zijl et al. (2016), combined with the data from the DPRs of the Nordnes for the period ranging from 24-10-2015 to 29-10-2015 (Track $S6_2$). In the upper left corner, a map of the area around the Shetland Islands is presented. The blue track represents the sailed path of the SRI vessel. On the right side a couple of variables are plotted over time. From top to bottom: the working schedule, the water level elevation [m], the wind speed [m/s], the flow velocity [m/s], the flow direction [-], the turbulent vertical eddy viscosity [m^2/s], the density [kg/m^3] and the Richardson number [-]. For the flow velocity, flow direction, turbulent vertical eddy viscosity and the density, a depth profile averaged over time per non-working interval is plotted on the left side of the figure. On the bottom left part, the water level elevation over four months, retrieved from EMODnet (2017), is plotted, indicating the spring-neap cycle.

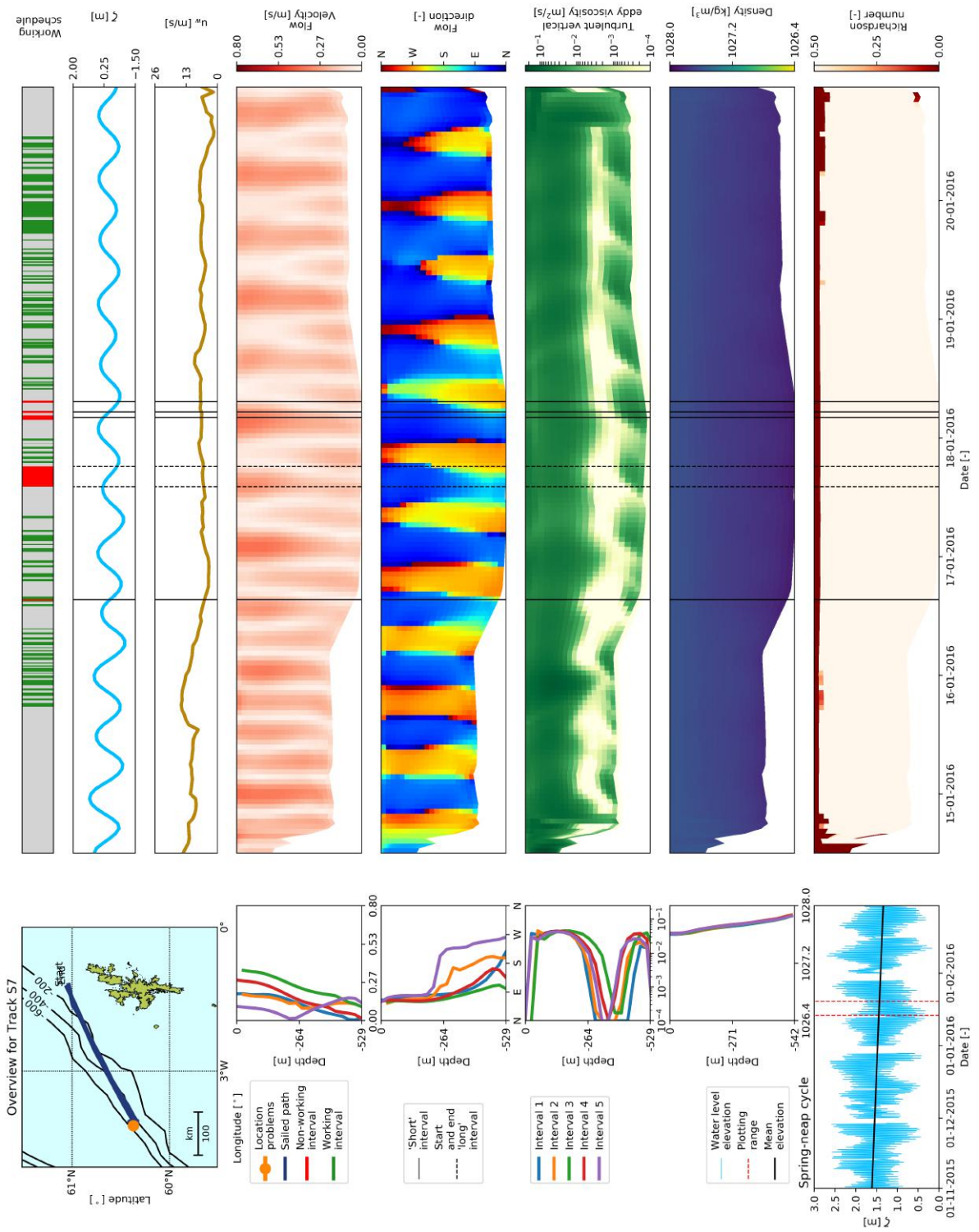

Figure E.6: Overview plot of the data from the 3D DCSM-FM by Zijl et al. (2016), combined with the data from the DPRs of the Nordnes for the period ranging from 15-01-2016 to 20-01-2016 (Track S7). In the upper left corner, a map of the area around the Shetland Islands is presented. The blue track represents the sailed path of the SRI vessel. On the right side a couple of variables are plotted over time. From top to bottom: the working schedule, the water level elevation [m], the wind speed [m/s], the flow velocity [m/s], the flow direction [-], the turbulent vertical eddy viscosity [m^2/s], the density [kg/m^3] and the Richardson number [-]. For the flow velocity, flow direction, turbulent vertical eddy viscosity and the density, a depth profile averaged over time per non-working interval is plotted on the left side of the figure. On the bottom left part, the water level elevation over four months, retrieved from EMODnet (2017), is plotted, indicating the spring-neap cycle.

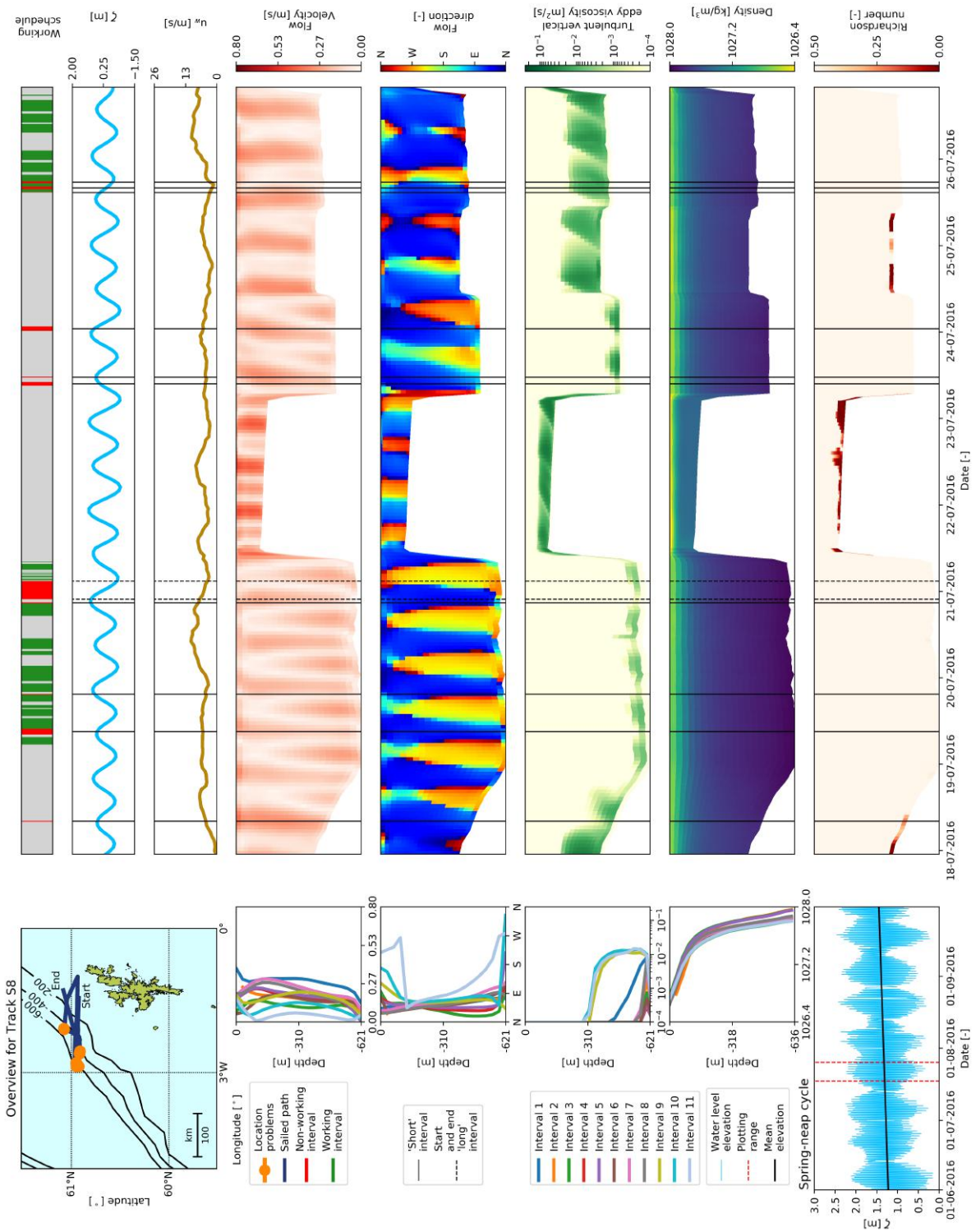

Figure E.7: Overview plot of the data from the 3D DCSM-FM by Zijl et al. (2016), combined with the data from the DPRs of the Nordnes for the period ranging from 18-07-2016 to 26-07-2016 (Track S8). In the upper left corner, a map of the area around the Shetland Islands is presented. The blue track represents the sailed path of the SRI vessel. On the right side a couple of variables are plotted over time. From top to bottom: the working schedule, the water level elevation [m], the wind speed [m/s], the flow velocity [m/s], the flow direction [-], the turbulent vertical eddy viscosity [m^2/s], the density [kg/m^3] and the Richardson number [-]. For the flow velocity, flow direction, turbulent vertical eddy viscosity and the density, a depth profile averaged over time per non-working interval is plotted on the left side of the figure. On the bottom left part, the water level elevation over four months, retrieved from EMODnet (2017), is plotted, indicating the spring-neap cycle.

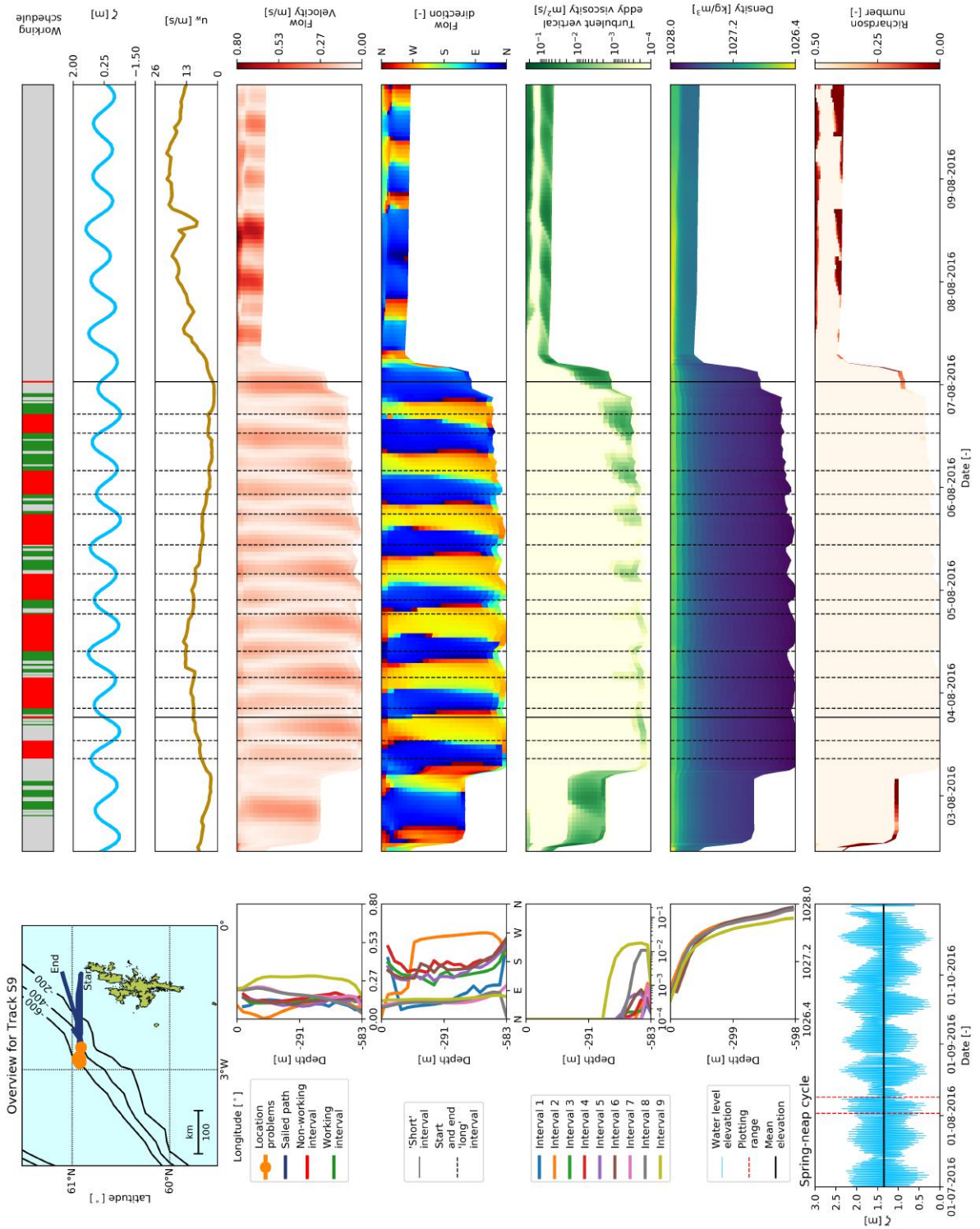

Figure E.8: Overview plot of the data from the 3D DCSM-FM by Zijl et al. (2016), combined with the data from the DPRs of the Nordnes for the period ranging from 03-08-2016 to 09-08-2016 (Track S9). In the upper left corner, a map of the area around the Shetland Islands is presented. The blue track represents the sailed path of the SRI vessel. On the right side a couple of variables are plotted over time. From top to bottom: the working schedule, the water level elevation [m], the wind speed [m/s], the flow velocity [m/s], the flow direction [-], the turbulent vertical eddy viscosity [m^2/s], the density [kg/m^3] and the Richardson number [-]. For the flow velocity, flow direction, turbulent vertical eddy viscosity and the density, a depth profile averaged over time per non-working interval is plotted on the left side of the figure. On the bottom left part, the water level elevation over four months, retrieved from EMODnet (2017), is plotted, indicating the spring-neap cycle.

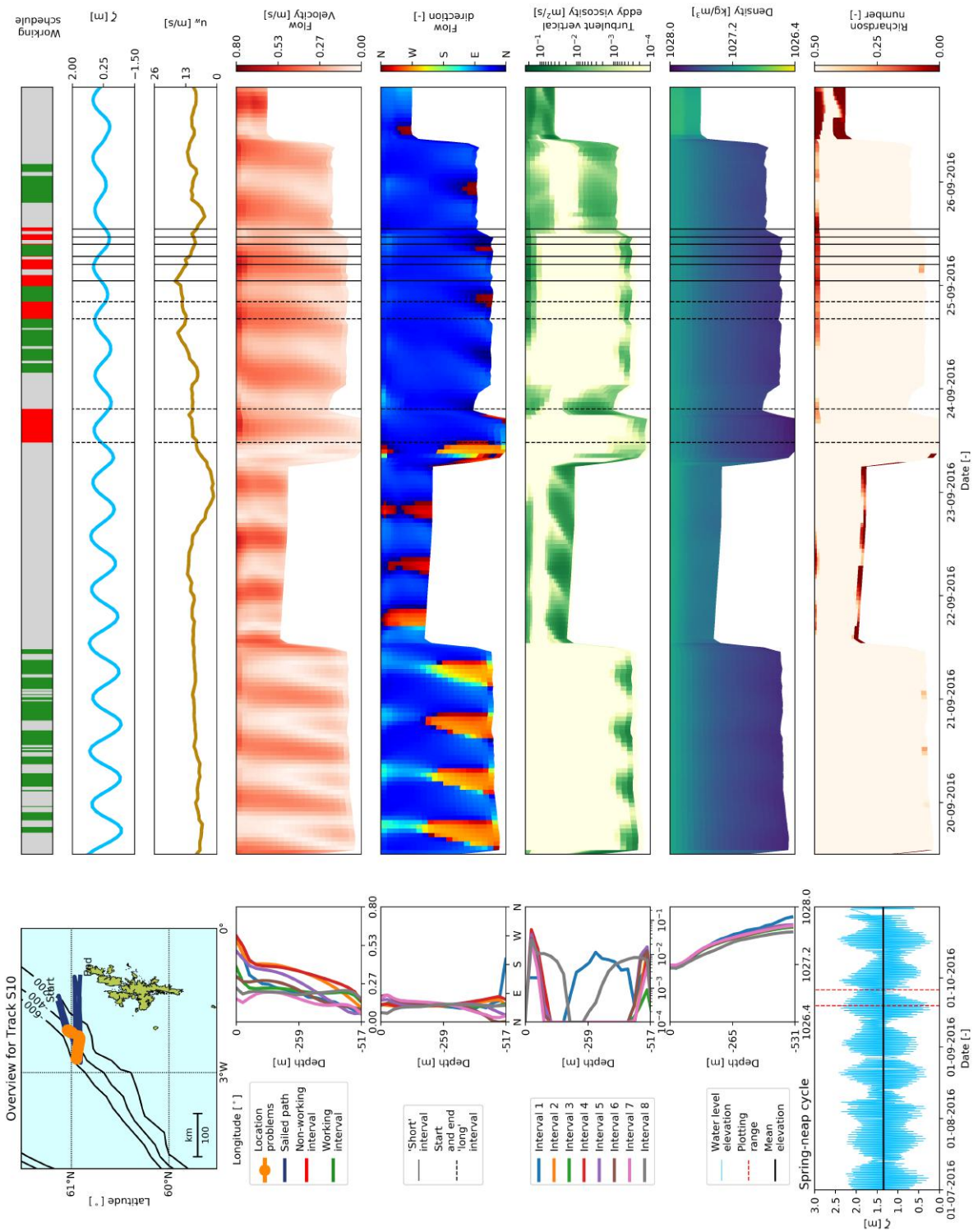

Figure E.9: Overview plot of the data from the 3D DCSM-FM by Zijl et al. (2016), combined with the data from the DPRs of the Nordnes for the period ranging from 20-09-2016 to 26-09-2016 (Track S10). In the upper left corner, a map of the area around the Shetland Islands is presented. The blue track represents the sailed path of the SRI vessel. On the right side a couple of variables are plotted over time. From top to bottom: the working schedule, the water level elevation [m], the wind speed [m/s], the flow velocity [m/s], the flow direction [-], the turbulent vertical eddy viscosity [m^2/s], the density [kg/m^3] and the Richardson number [-]. For the flow velocity, flow direction, turbulent vertical eddy viscosity and the density, a depth profile averaged over time per non-working interval is plotted on the left side of the figure. On the bottom left part, the water level elevation over four months, retrieved from EMODnet (2017), is plotted, indicating the spring-neap cycle.

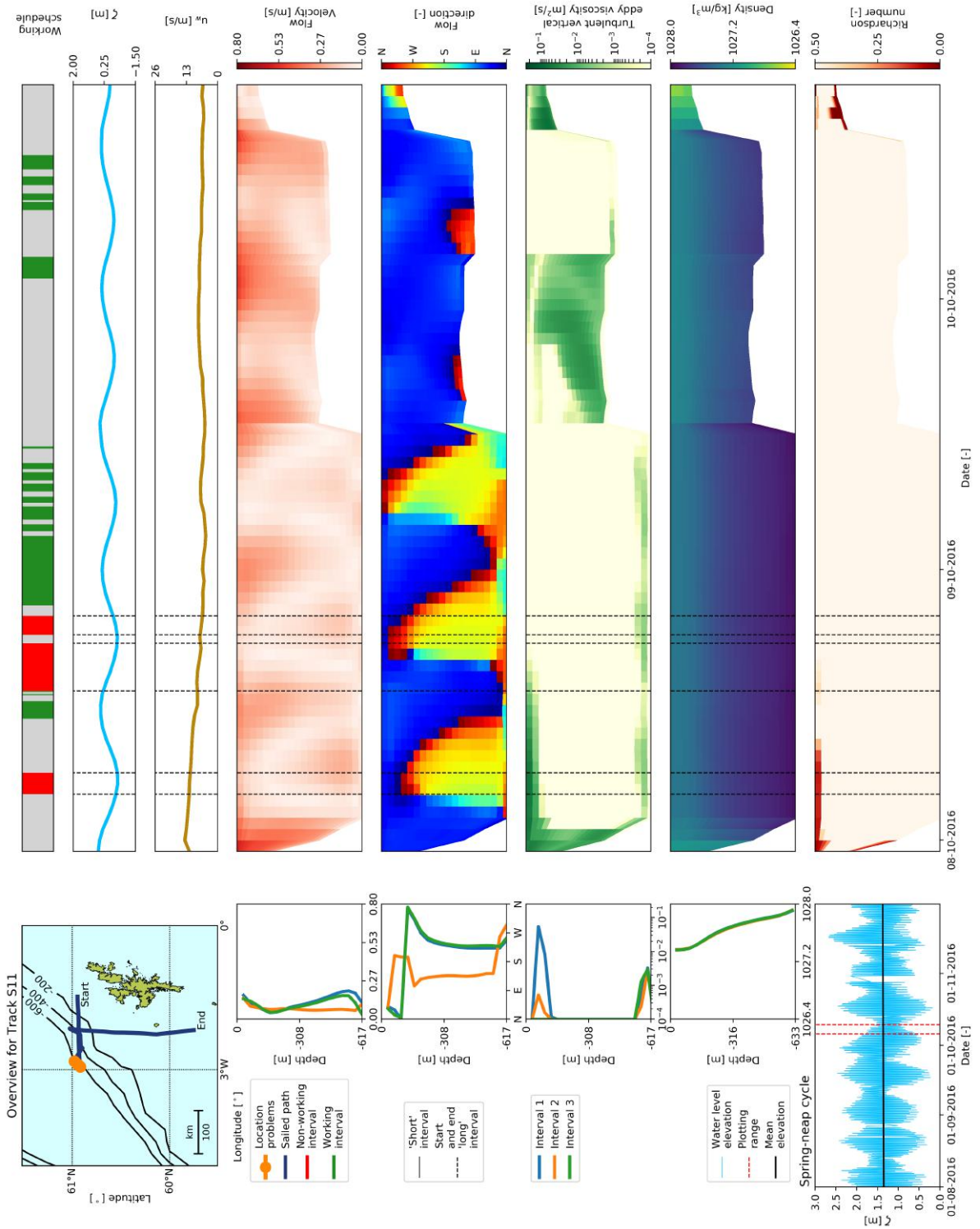

Figure E.10: Overview plot of the data from the 3D DCSM-FM by Zijl et al. (2016), combined with the data from the DPRs of the Nordnes for the period ranging from 08-10-2016 to 10-10-2016 (Track S11). In the upper left corner, a map of the area around the Shetland Islands is presented. The blue track represents the sailed path of the SRI vessel. On the right side a couple of variables are plotted over time. From top to bottom: the working schedule, the water level elevation [m], the wind speed [m/s], the flow velocity [m/s], the flow direction [-], the turbulent vertical eddy viscosity [m^2/s], the density [kg/m^3] and the Richardson number [-]. For the flow velocity, flow direction, turbulent vertical eddy viscosity and the density, a depth profile averaged over time per non-working interval is plotted on the left side of the figure. On the bottom left part, the water level elevation over four months, retrieved from EMODnet (2017), is plotted, indicating the spring-neap cycle.

Appendix F

Additional plots

This appendix contains additional plots of different variables discussed in Chapters 3, 4 and 6. First, the temperature and salinity profiles over depth are presented, followed by the wind roses and roses of the flow. Subsequently, scatter plots of the turbulence properties are depicted and lastly, a couple of plots of the shear and veering profiles over depth are included.

F.1. Temperature and salinity profiles

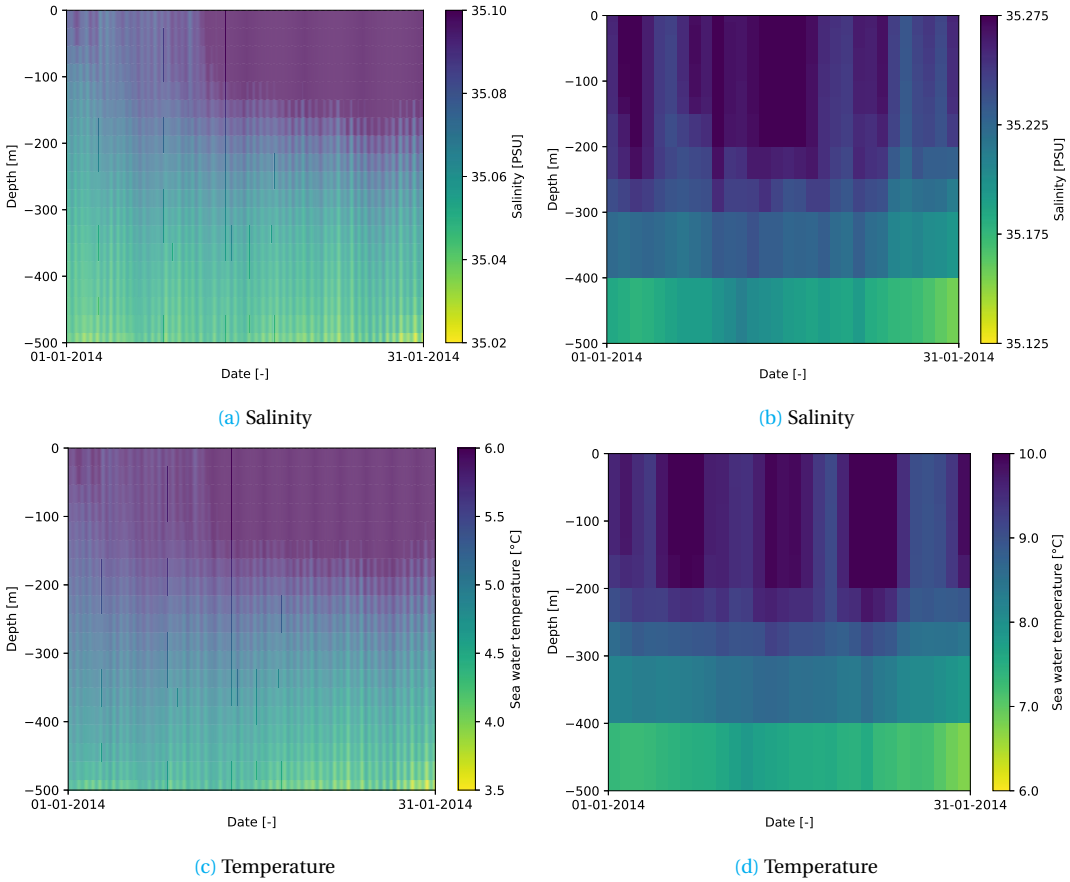

(a) Salinity

(b) Salinity

(c) Temperature

(d) Temperature

Figure F.1: Plot of the salinity [PSU] and temperature [°C] profiles at Location 1 over depth and time for (a) and (c) the 3D DCSM-FM by Zijl et al. (2016) and (b) and (d) the ocean model by CMEMS (2018).

F.2. Wind roses

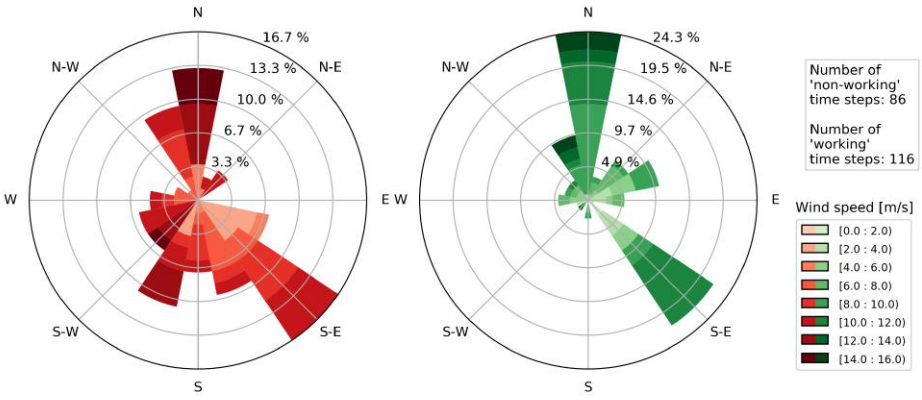

(a) Location 1

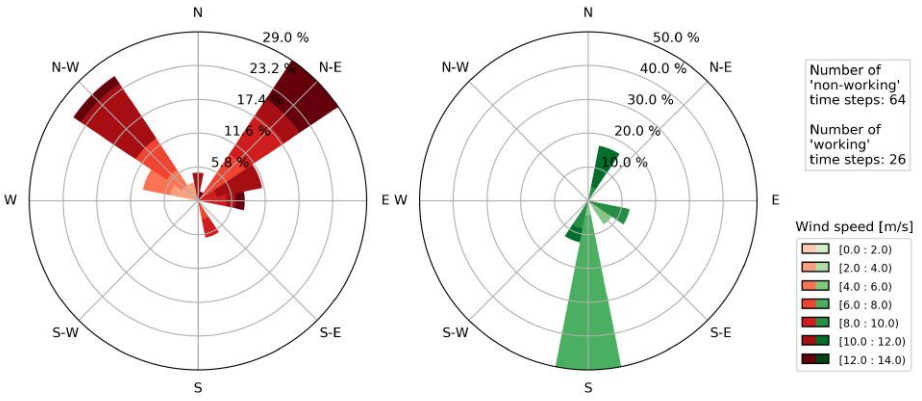

(b) Location 2

Figure F.2: Wind rose of the magnitude [m/s] and the direction [°] of the wind at (a) Location 1 and (b) Location 2 for all the available working (green) and non-working (red) intervals assembled. Data retrieved from the 3D DCSM-FM by Zijl et al. (2016).

F.3. Roses of the flow

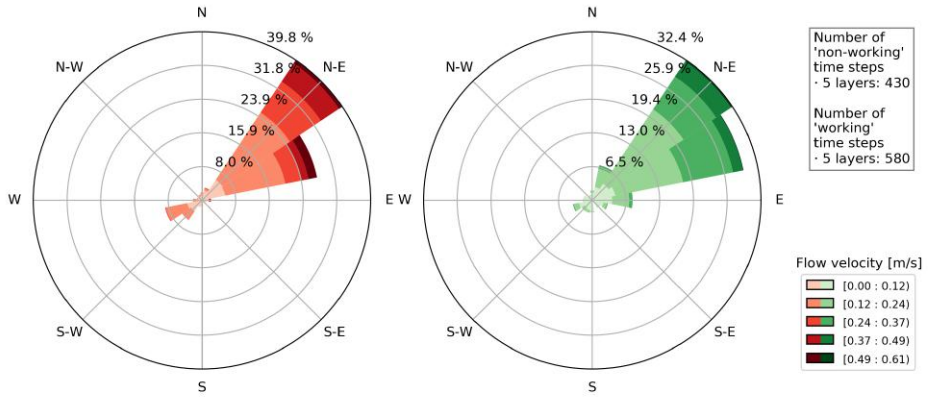

(a) Top part

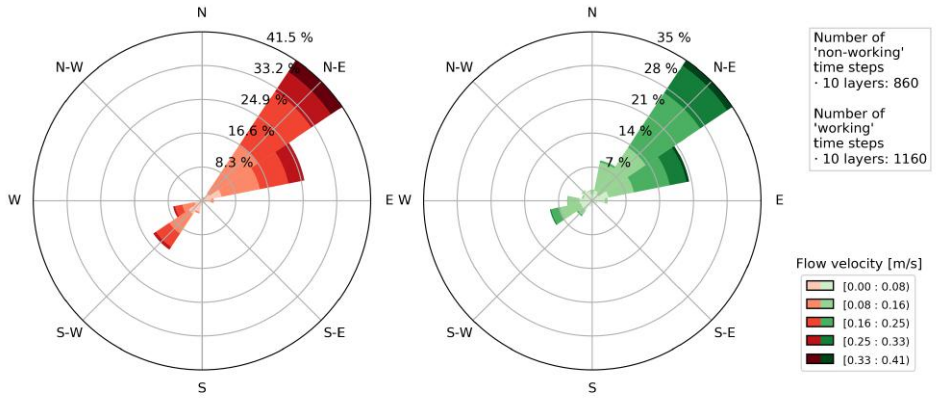

(b) Middle part

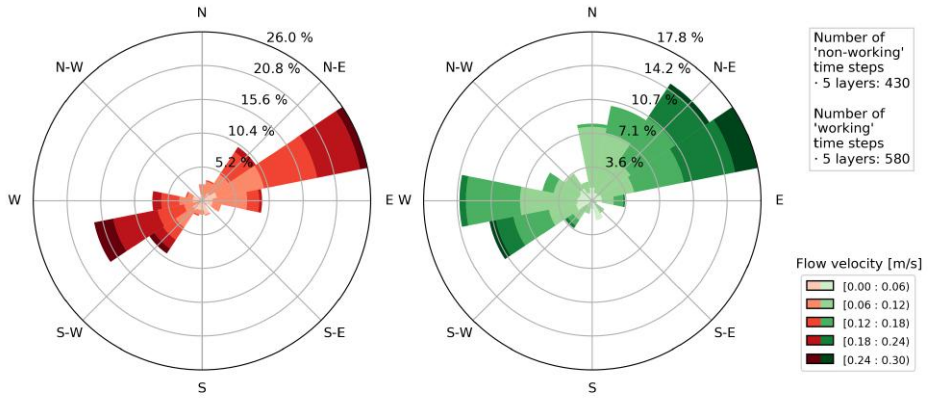

(c) Bottom part

Figure F.3: Rose of the magnitude [m/s] and the direction [°] of the flow in the (a) top part, (b) middle part and (c) bottom part of the water column at Location 1 for all the available working (green) and non-working (red) intervals assembled. Data retrieved from the 3D DCSM-FM by Zijl et al. (2016).

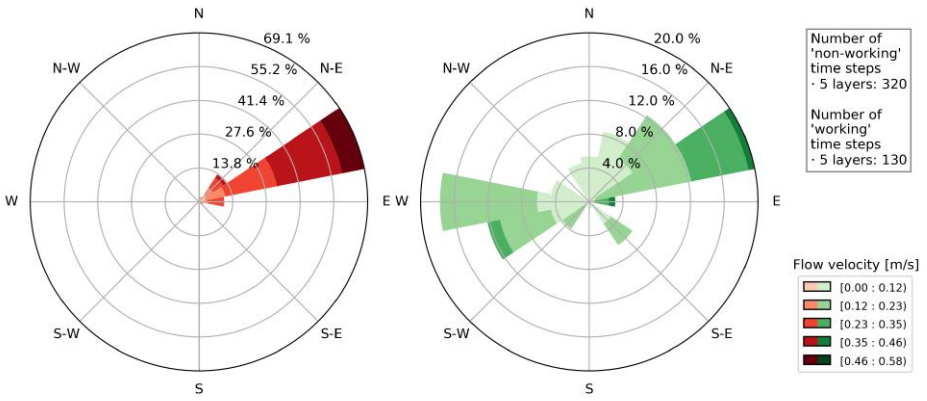

(a) Top part

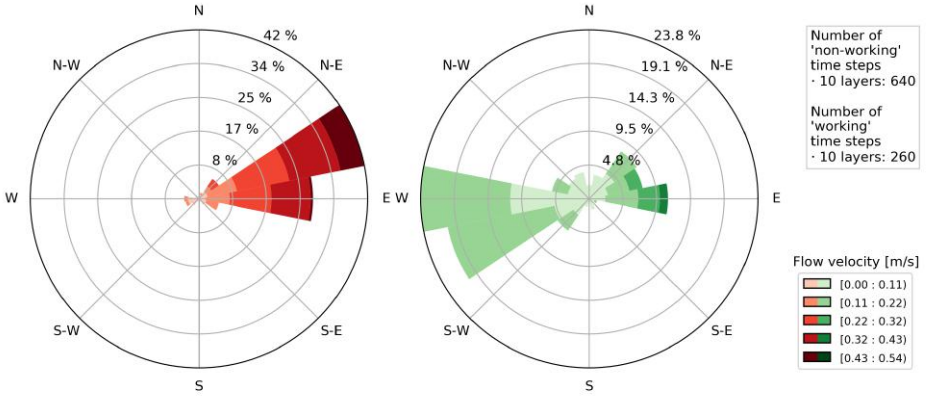

(b) Middle part

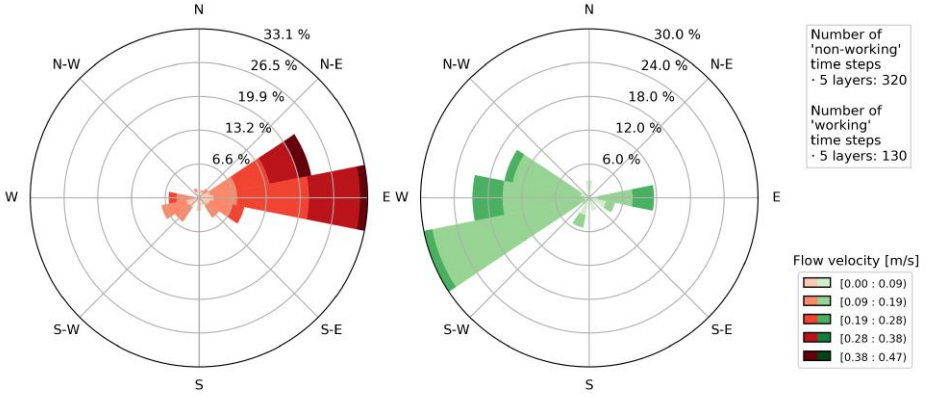

(c) Bottom part

Figure F.4: Rose of the magnitude [m/s] and the direction [°] of the flow in the (a) top part, (b) middle part and (c) bottom part of the water column at Location 2 for all the available working (green) and non-working (red) intervals assembled. Data retrieved from the 3D DCSM-FM by Zijl et al. (2016).

Table F.1: Overview of the percentages of time that the flow was directed to each of the sixteen flow directions (FD) during working and non-working intervals in the top part of the water column at Location 1. The number of time steps per direction (#) is included to indicate the contribution to the total number of data points from the 3D DCSM-FM by Zijl et al. (2016), which is 1010.

Location 1 - Top part															
FD	●	●	**#**	**FD**	●	●	**#**	**FD**	●	●	**#**	**FD**	●	●	**#**
N	42%	58%	19	E	17%	87%	54	S	32%	68%	19	W	47%	53%	19
NNE	25%	75%	53	ESE	18%	88%	22	SSW	33%	67%	21	WNW	33%	67%	15
NE	48%	52%	359	SE	33%	67%	15	SW	63%	37%	38	NW	44%	56%	9
ENE	41%	59%	291	SSE	50%	50%	4	WSW	63%	37%	60	NNW	50%	50%	12

Table F.2: Overview of the percentages of time that the flow was directed to each of the sixteen flow directions (FD) during working and non-working intervals in the middle part of the water column at Location 1. The number of time steps per direction (#) is included to indicate the contribution to the total number of data points from the 3D DCSM-FM by Zijl et al. (2016), which is 2020.

Location 1 - Middle part															
FD	●	●	**#**	**FD**	●	●	**#**	**FD**	●	●	**#**	**FD**	●	●	**#**
N	4%	96%	28	E	40%	60%	63	S	53%	47%	15	W	2%	98%	62
NNE	7%	93%	108	ESE	41%	59%	22	SSW	68%	32%	40	WNW	4%	96%	27
NE	47%	53%	767	SE	40%	60%	20	SW	73%	27%	169	NW	3%	97%	32
ENE	48%	52%	461	SSE	46%	54%	13	WSW	37%	63%	167	NNW	4%	96%	26

Table F.3: Overview of the percentages of time that the flow was directed to each of the sixteen flow directions (FD) during working and non-working intervals in the bottom part of the water column at Location 1. The number of time steps per direction (#) is included to indicate the contribution to the total number of data points from the 3D DCSM-FM by Zijl et al. (2016), which is 1010.

Location 1 - Bottom part															
FD	●	●	**#**	**FD**	●	●	**#**	**FD**	●	●	**#**	**FD**	●	●	**#**
N	19%	81%	58	E	67%	33%	60	S	64%	36%	14	W	29%	71%	114
NNE	19%	81%	73	ESE	81%	19%	16	SSW	56%	44%	18	WNW	26%	74%	42
NE	33%	67%	129	SE	31%	69%	13	SW	68%	32%	62	NW	9%	91%	22
ENE	52%	48%	215	SSE	45%	55%	22	WSW	53%	47%	137	NNW	20%	80%	15

Table F.4: Overview of the percentages of time that the flow was directed to each of the sixteen flow directions (FD) during working and non-working intervals in the top part of the water column at Location 2. The number of time steps per direction (#) is included to indicate the contribution to the total number of data points from the 3D DCSM-FM by Zijl et al. (2016), which is 450.

Location 2 - Top part															
FD	●	●	**#**	**FD**	●	●	**#**	**FD**	●	●	**#**	**FD**	●	●	**#**
N	42%	58%	12	E	89%	11%	37	S	0%	100%	1	W	0%	100%	23
NNE	39%	61%	18	ESE	100%	0%	6	SSW	-	-	0	WNW	0%	100%	6
NE	73%	27%	59	SE	11%	89%	9	SW	0%	100%	5	NW	100%	0%	2
ENE	89%	11%	247	SSE	0%	100%	1	WSW	0%	100%	16	NNW	25%	75%	8

Table F.5: Overview of the percentages of time that the flow was directed to each of the sixteen flow directions (FD) during working and non-working intervals in the middle part of the water column at Location 2. The number of time steps per direction (#) is included to indicate the contribution to the total number of data points from the 3D DCSM-FM by Zijl et al. (2016), which is 900.

Location 2 - Middle part															
FD	●	●	**#**	**FD**	●	●	**#**	**FD**	●	●	**#**	**FD**	●	●	**#**
N	44%	56%	9	E	87%	13%	215	S	50%	50%	4	W	28%	72%	86
NNE	53%	47%	19	ESE	92%	8%	36	SSW	63%	37%	8	WNW	30%	70%	20
NE	65%	35%	60	SE	85%	15%	13	SW	46%	54%	26	NW	18%	82%	11
ENE	93%	7%	295	SSE	56%	44%	9	WSW	29%	71%	75	NNW	29%	71%	14

Table F.6: Overview of the percentages of time that the flow was directed to each of the sixteen flow directions (FD) during working and non-working intervals in the bottom part of the water column at Location 2. The number of time steps per direction (#) is included to indicate the contribution to the total number of data points from the 3D DCSM-FM by Zijl et al. (2016), which is 450.

Location 2 - Bottom part															
FD	●	●	**#**	**FD**	●	●	**#**	**FD**	●	●	**#**	**FD**	●	●	**#**
N	33%	67%	6	E	88%	12%	121	S	89%	11%	9	W	41%	59%	46
NNE	83%	17%	6	ESE	83%	17%	35	SSW	30%	70%	10	WNW	0%	100%	20
NE	88%	12%	8	SE	94%	6%	16	SW	90%	10%	20	NW	33%	67%	3
ENE	100%	0%	72	SSE	63%	37%	8	WSW	38%	62%	63	NNW	86%	14%	7

F.4. Scatter plots turbulence

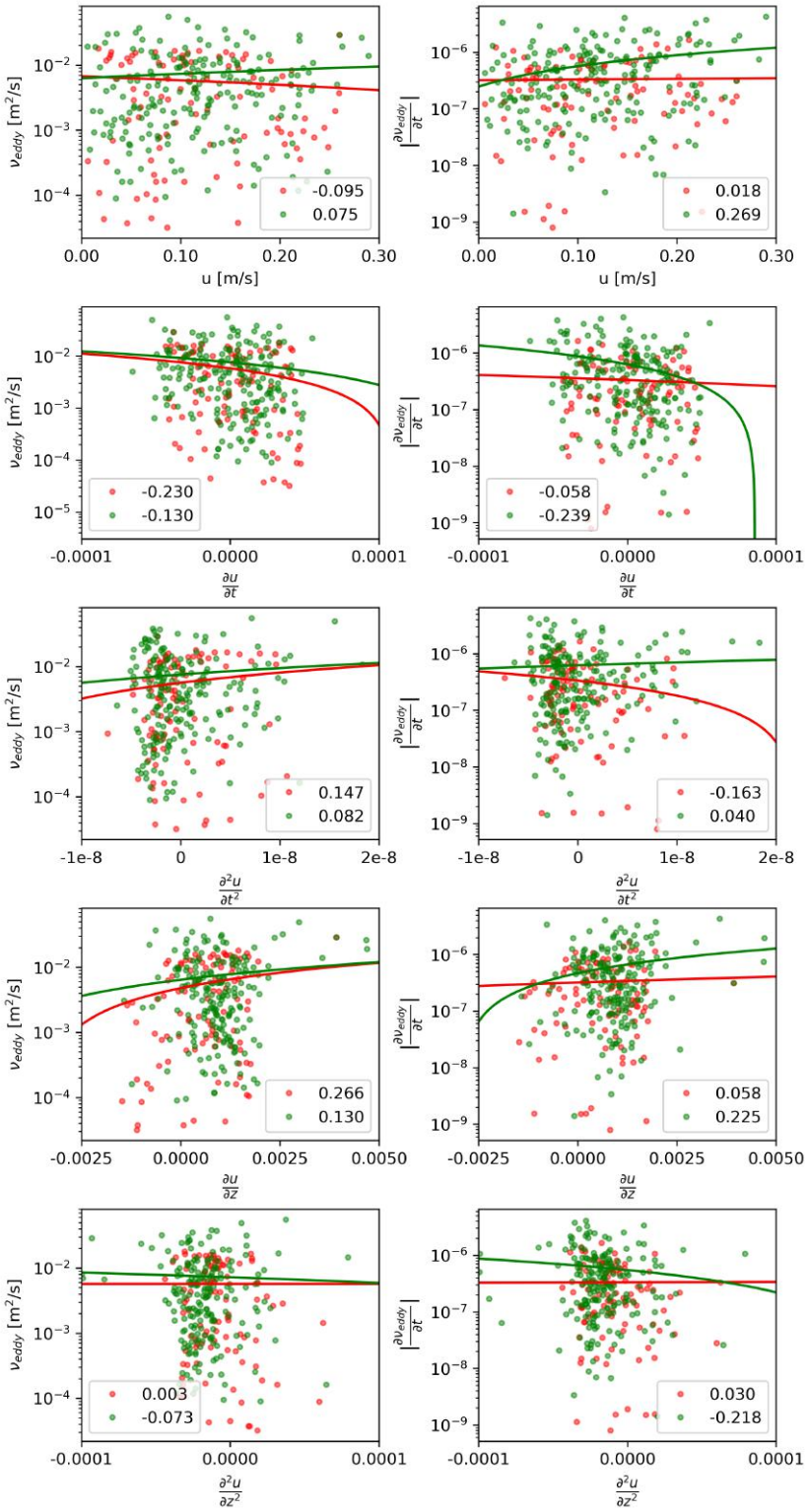

Figure F.5: Scatter plot of the turbulent vertical eddy viscosity (ν_{eddy}) [m^2/s] and the first derivative in time of the turbulent vertical eddy viscosity ($\frac{\partial \nu_{\text{eddy}}}{\partial t}$) versus five different variables related to the velocity (u) in the bottom layer of the water column at Location 1. The green dots indicate working intervals and the red dots indicate non-working intervals. Data retrieved from the 3D DCSM-FM by Zijl et al. (2016).

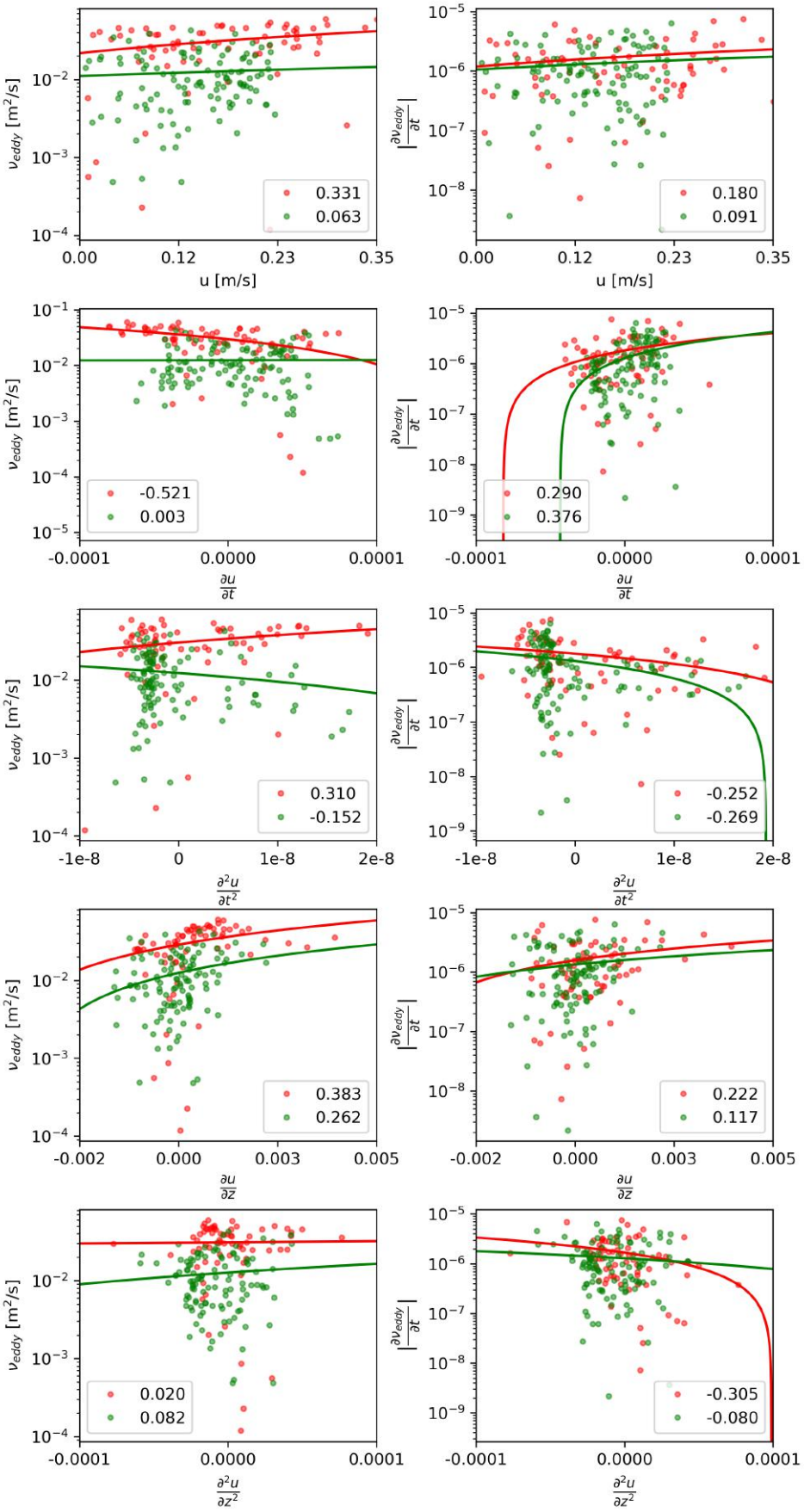

Figure F.6: Scatter plot of the turbulent vertical eddy viscosity (ν_{eddy}) [m^2/s] and the first derivative in time of the turbulent vertical eddy viscosity ($\frac{\partial \text{veddy}}{\partial t}$) versus five different variables related to the velocity (u) in the bottom layer of the water column at Location 2. The green dots indicate working intervals and the red dots indicate non-working intervals. Data retrieved from the 3D DCSM-FM by Zijl et al. (2016).

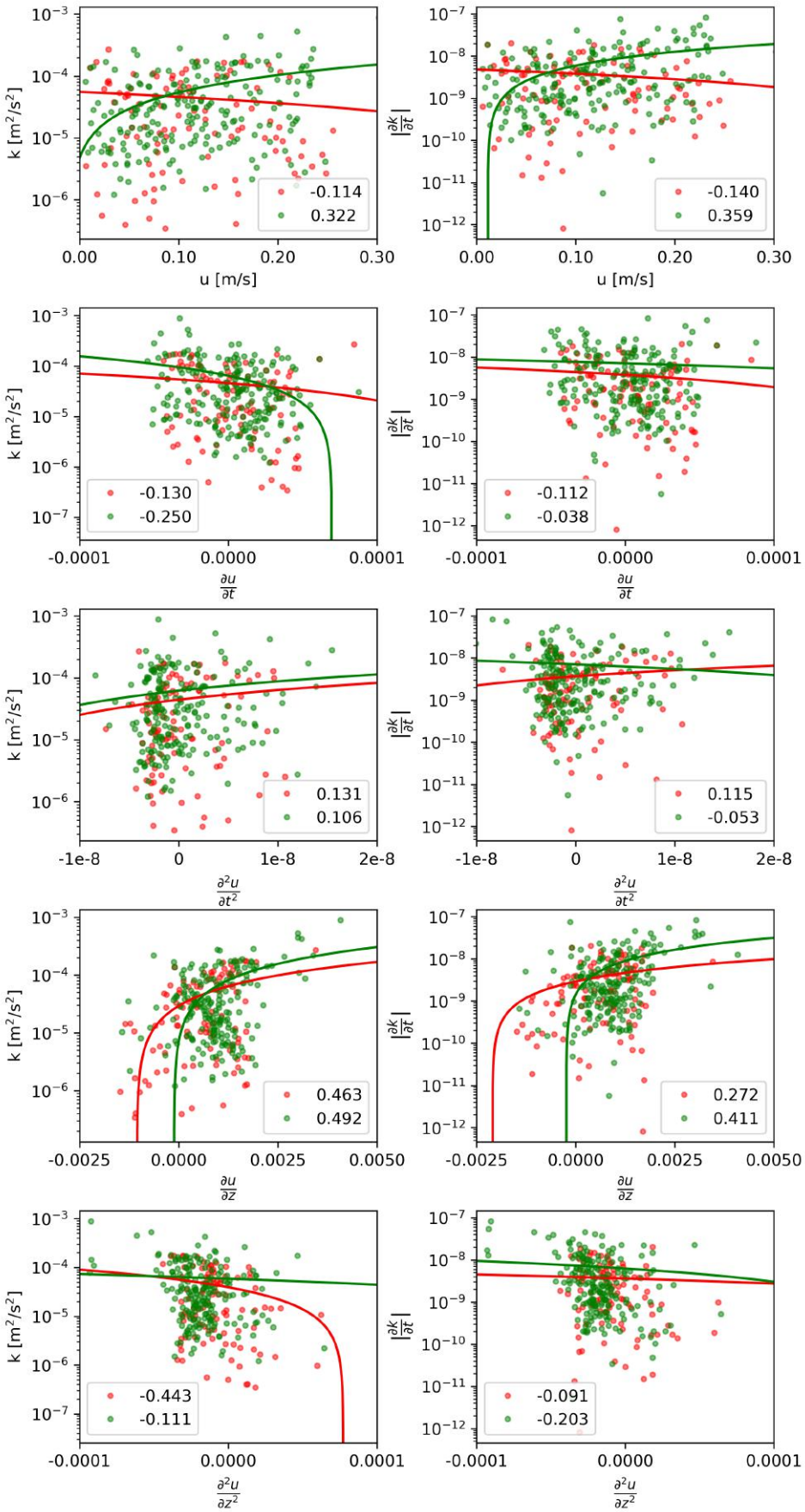

Figure F.7: Scatter plot of the turbulent kinetic energy (k) [m^2/s^2] and the first derivative in time of the turbulent kinetic energy ($\frac{\partial k}{\partial t}$) versus five different variables related to the velocity (u) in the bottom layer of the water column at Location 1. The green dots indicate working intervals and the red dots indicate non-working intervals. Data retrieved from the 3D DCSM-FM by Zijl et al. (2016).

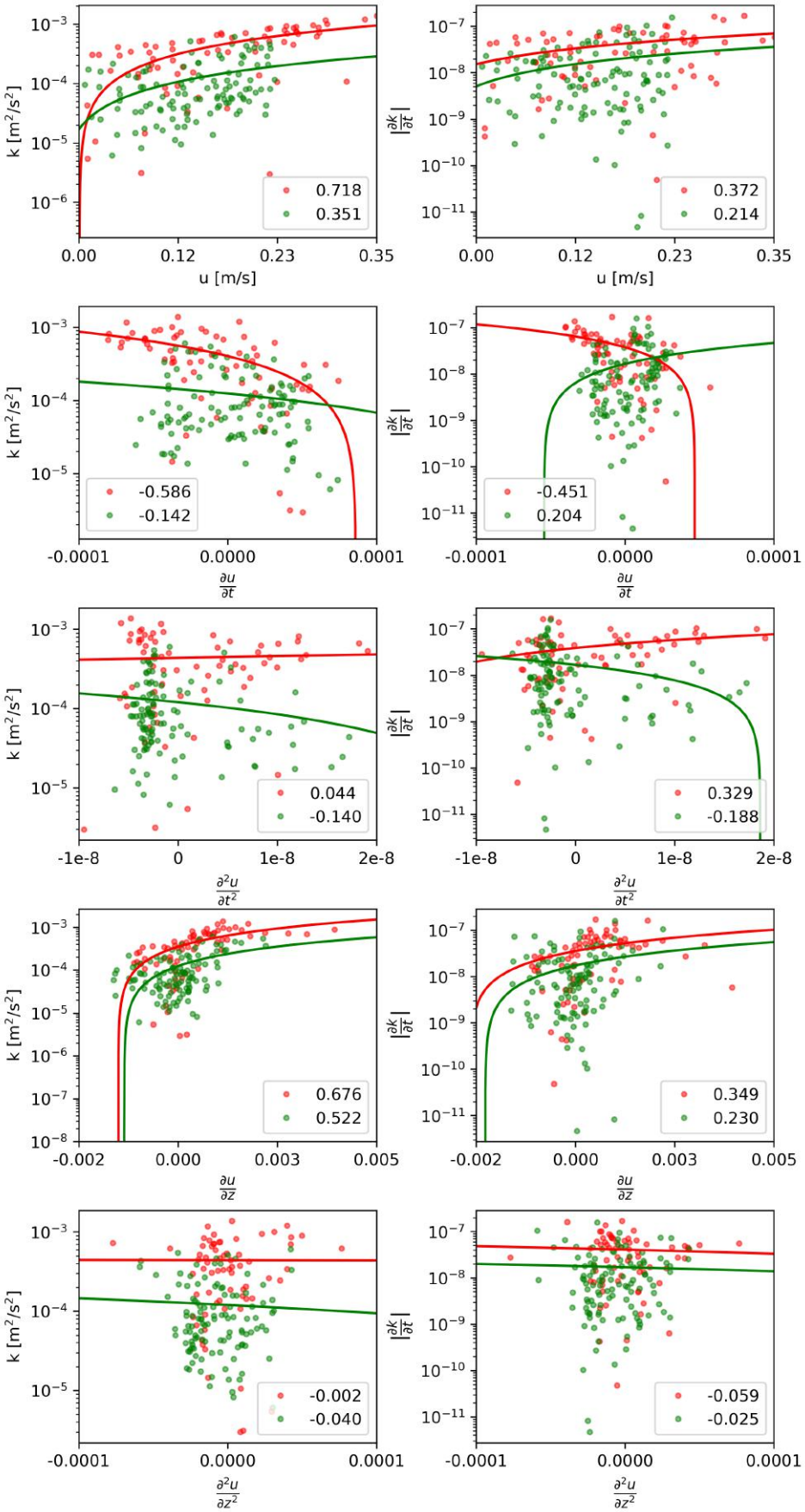

Figure F.8: Scatter plot of the turbulent kinetic energy (k) [m^2/s^2] and the first derivative in time of the turbulent kinetic energy ($\frac{\partial k}{\partial t}$) versus five different variables related to the velocity (u) in the bottom layer of the water column at Location 2. The green dots indicate working intervals and the red dots indicate non-working intervals. Data retrieved from the 3D DCSM-FM by Zijl et al. (2016).

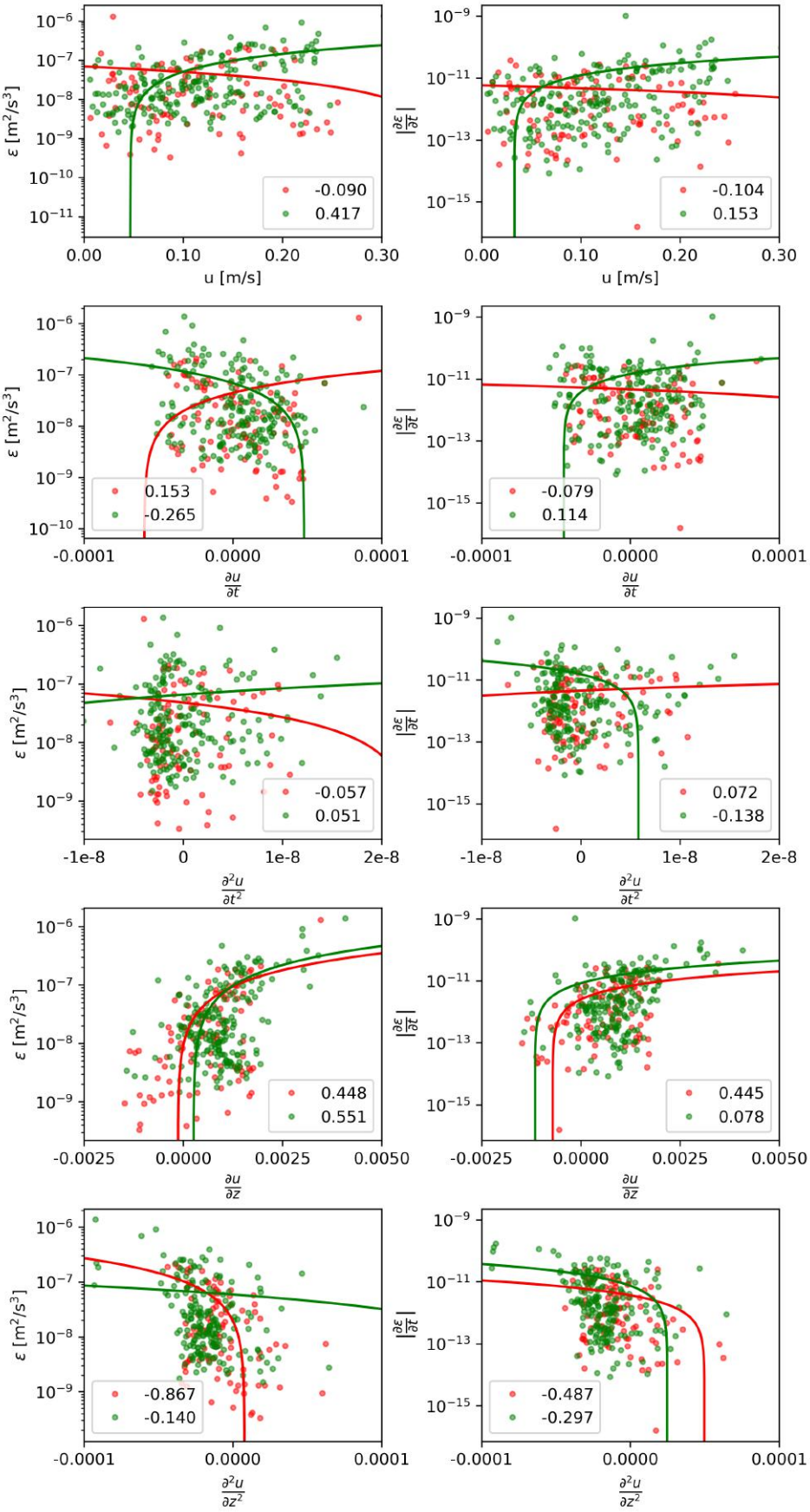

Figure F.9: Scatter plot of the turbulent energy dissipation (ϵ) [m^2/s^3] and the first derivative in time of the turbulent energy dissipation ($\frac{\partial \epsilon}{\partial t}$) versus five different variables related to the velocity (u) in the bottom layer of the water column at Location 1. The green dots indicate working intervals and the red dots indicate non-working intervals. Data retrieved from the 3D DCSM-FM by Zijl et al. (2016).

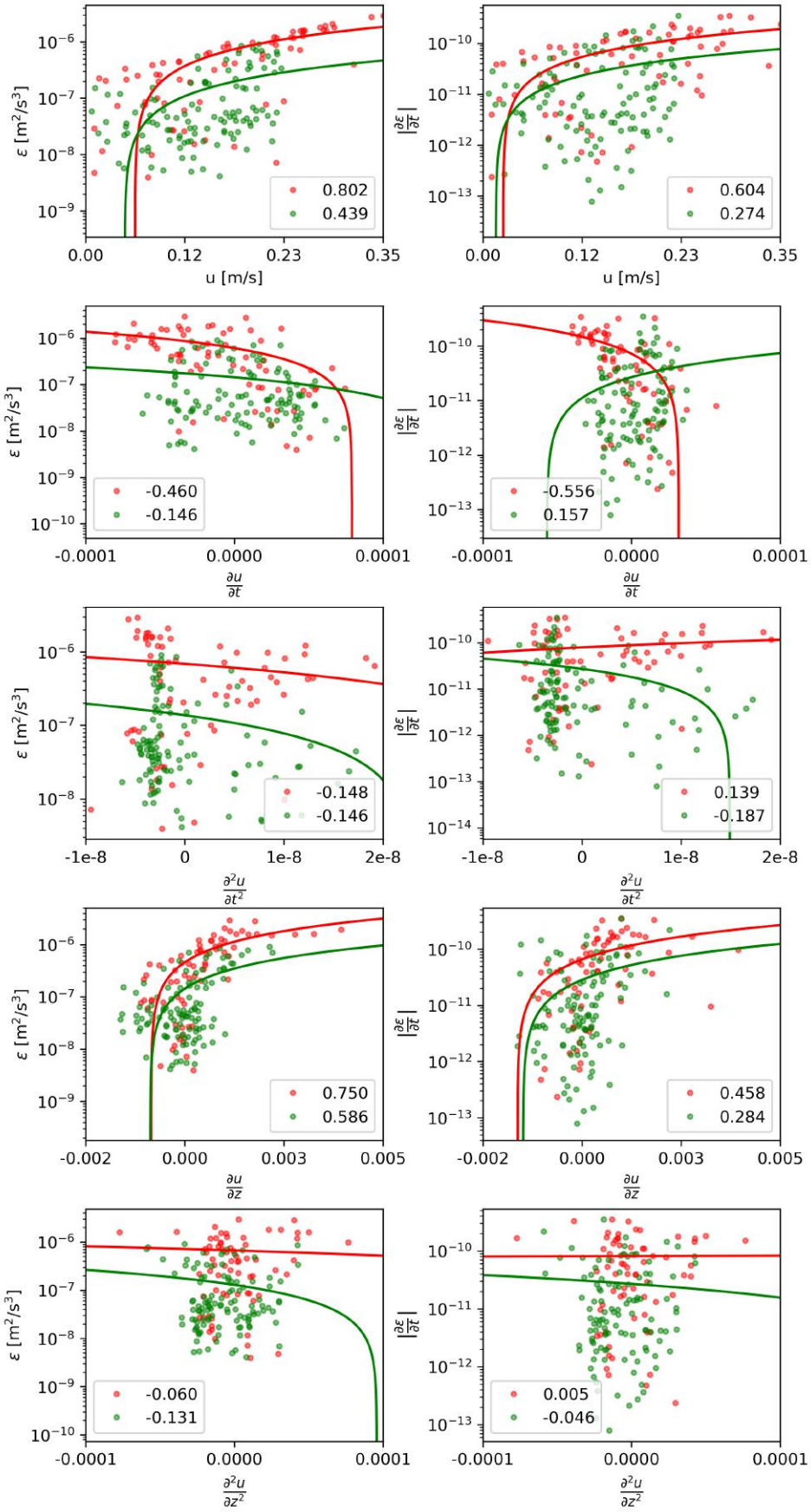

Figure F.10: Scatter plot of the turbulent energy dissipation (ϵ) [m^2/s^3] and the first derivative in time of the turbulent energy dissipation ($\frac{\partial \epsilon}{\partial t}$) versus five different variables related to the velocity (u) in the bottom layer of the water column at Location 2. The green dots indicate working intervals and the red dots indicate non-working intervals. Data retrieved from the 3D DCSM-FM by Zijl et al. (2016).

Table F.7: Overview of the correlation coefficients of the three turbulence variables (ν_{eddy}, k and ϵ) and five different flow velocity variables at Location 1. The coefficients are obtained from from Figures F.5, F.7 and F.9.

Turbulence variable	u	$\frac{\partial u}{\partial t}$	$\frac{\partial^2 u}{\partial t^2}$	$\frac{\partial u}{\partial z}$	$\frac{\partial^2 u}{\partial z^2}$
ν_{eddy}					
Working intervals (●)	0.075	-0.130	0.082	0.130	-0.073
Non-working intervals (●)	-0.095	-0.230	0.147	0.266	0.003
k					
Working intervals (●)	0.322	-0.250	0.106	0.492	-0.111
Non-working intervals (●)	-0.114	-0.130	0.131	0.463	-0.443
ϵ					
Working intervals (●)	0.417	-0.265	0.051	0.551	-0.140
Non-working intervals (●)	-0.090	0.153	-0.057	0.448	-0.867

Table F.8: Overview of the correlation coefficients of the three turbulence variables (ν_{eddy}, k and ϵ) and five different flow velocity variables at Location 2. The coefficients are obtained from from Figures F.6, F.8 and F.10.

Turbulence variable	u	$\frac{\partial u}{\partial t}$	$\frac{\partial^2 u}{\partial t^2}$	$\frac{\partial u}{\partial z}$	$\frac{\partial^2 u}{\partial z^2}$
ν_{eddy}					
Working intervals (●)	0.063	0.003	-0.152	0.262	0.082
Non-working intervals (●)	0.331	-0.521	0.310	0.383	0.020
k					
Working intervals (●)	0.351	-0.142	-0.140	0.522	-0.040
Non-working intervals (●)	0.718	-0.586	0.044	0.676	-0.002
ϵ					
Working intervals (●)	0.439	-0.146	-0.146	0.586	-0.131
Non-working intervals (●)	0.802	-0.460	0.148	0.750	-0.060

F.5. Shear and veering

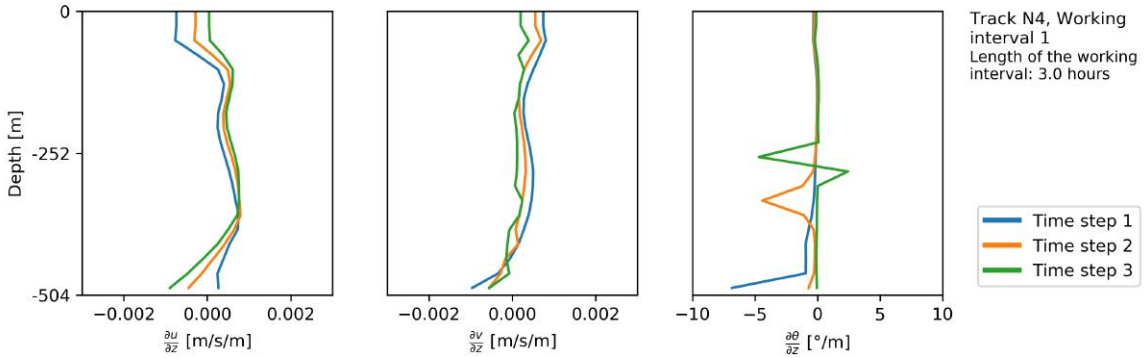

(a) Working interval

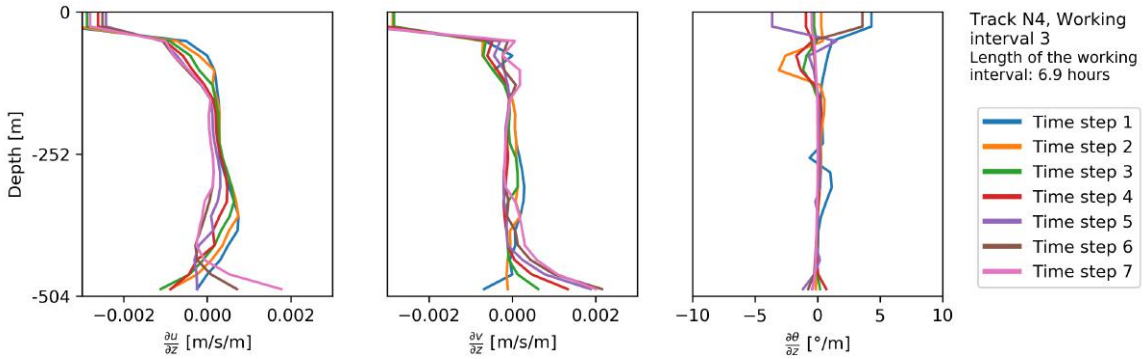

(b) Working interval

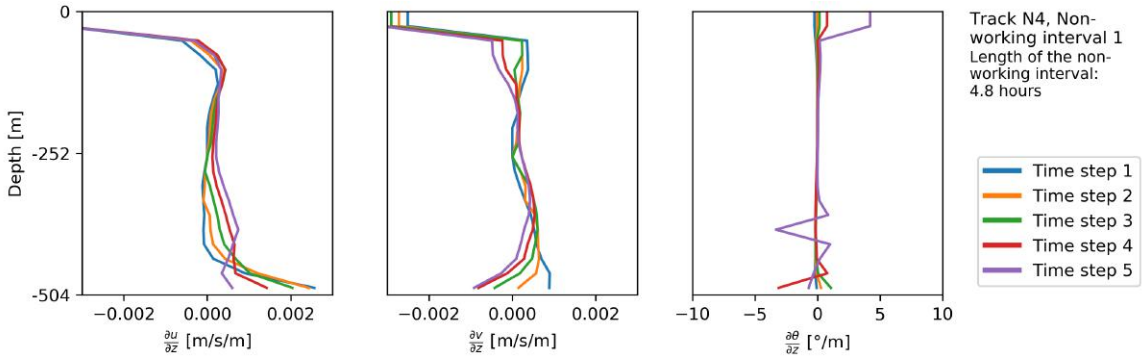

(c) Non-working interval

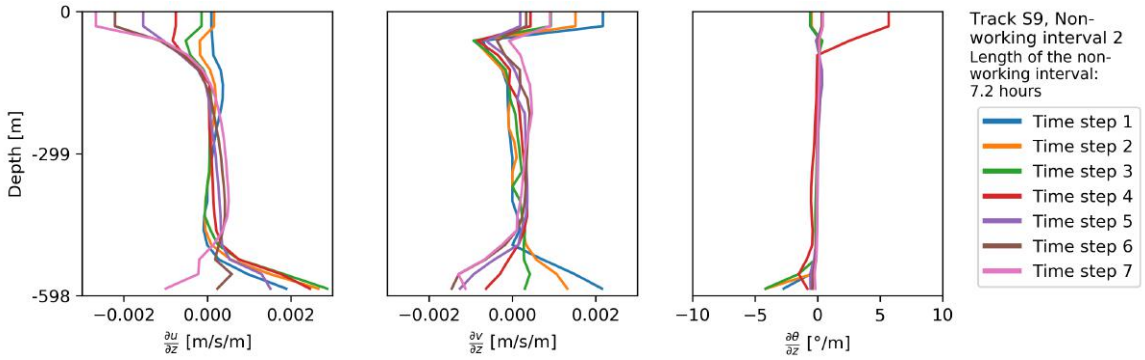

(d) Non-working interval

Figure F.11: Plot of the shear in x-direction [m/s/m] (left), the shear in y-direction [m/s/m] (middle) and the veering [°/m] (right) in the water column for (a) and (b) a working interval and (c) and (d) a non-working interval. Data retrieved from the 3D DCSM-FM by Zijl et al. (2016).

Appendix G

Additional information FFT

This appendix contains additional information for the Fast Fourier Transform (FFT) performed in Chapter 5.

Functioning FFT

In order to assess the proper functioning of the FFT Python package, a combination of two straightforward sinus functions is used as input signal for the analysis, see Figure G.1a. The differences between both sinus functions are a larger amplitude and a shorter period. The frequency spectrum corresponding to this signal, can be found in Figure G.1b. The two peaks indicate the two frequencies, which are included in the total signal. The part of the signal that has an amplitude larger than 0.5 meter is filtered out, resulting in the orange pattern in Figure G.2. The filtered signal is equal to Signal 2 in Figure G.1a, which completes this short test analysis.

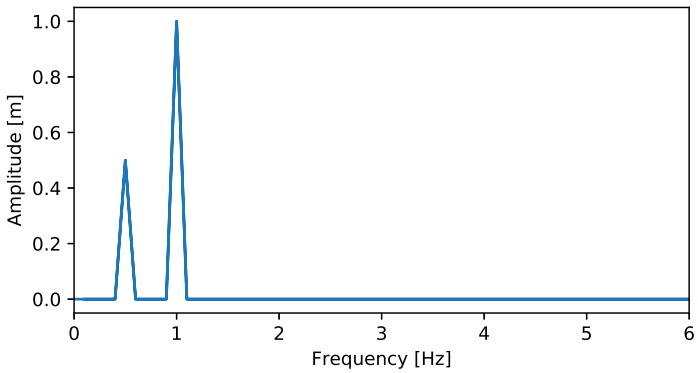

(a) Total sinusoidal signal

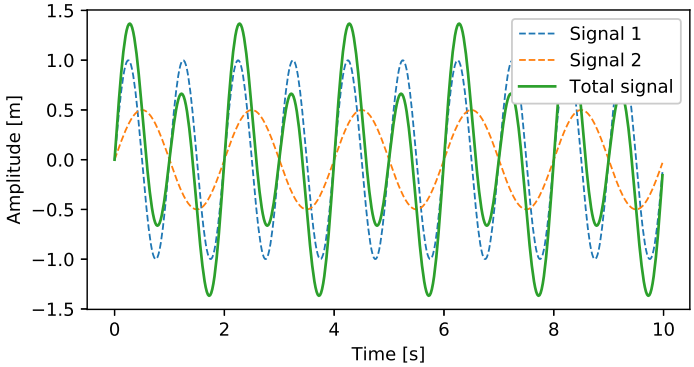

(b) Frequency spectrum

Figure G.1: Overview of two plots that depict the functioning of the FFT: (a) signal of the combination of two sinus functions and (b) the frequency spectrum corresponding to the total signal [m].

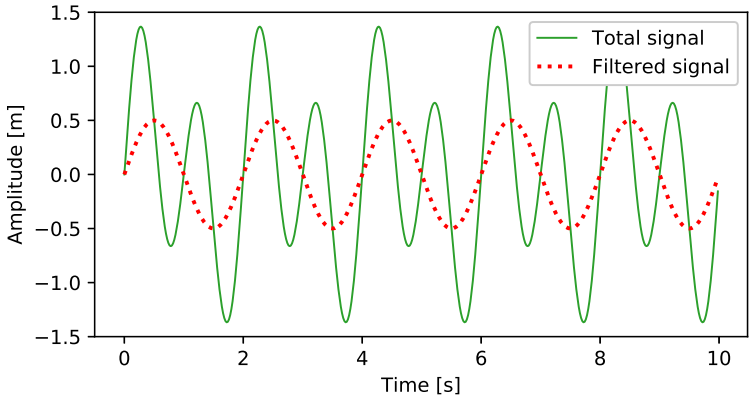

Figure G.2: Plot of the filtered signal [m], from which the part with an amplitude larger than 0.5 meter is removed.

Theoretical characteristics of tidal constituents

The tidal constituents mentioned in Table G.1 are filtered from the flow velocity signal output from the 3D DCSM-FM by Zijl et al. (2016). The presence of these components in the original frequency spectrum can be observed in Figure G.4.

Table G.1: Overview of the characteristics of the main tidal constituents, which are filtered from the velocity signal, retrieved from Apel (1987).

Tidal constituent	**Name [-]**	**Period [hours]**	**Period [days]**	**Frequency [Hz]**	**Frequency [cpd]**
Semi-diurnal					
Principal lunar	M_2	12.42	1.932	$2.237 \cdot 10^{-5}$	1.93
Principal solar	S_2	12.00	2.000	$2.315 \cdot 10^{-5}$	2.00
Lunar elliptical	N_2	12.66	1.896	$2.194 \cdot 10^{-5}$	1.90
Lunar-solar declinational	K_2	11.97	2.005	$2.321 \cdot 10^{-5}$	2.01
Diurnal					
Lunar-solar declinational	K_1	23.93	1.003	$1.161 \cdot 10^{-5}$	1.00
Principal lunar	O_1	25.82	0.930	$1.076 \cdot 10^{-5}$	0.93
Principal solar	P_1	24.07	0.997	$1.154 \cdot 10^{-5}$	1.00
Lunar elliptical	Q_1	26.87	0.893	$1.034 \cdot 10^{-5}$	0.89
Smaller lunar elliptic diurnal	M_1	24.84	0.966	$1.118 \cdot 10^{-5}$	0.97
Long period					
Fortnightly	M_f	327.90	0.073	$8.471 \cdot 10^{-7}$	0.07
Monthly	M_m	661.30	0.036	$4.200 \cdot 10^{-7}$	0.04
Semi-annual	S_{sa}	4383.00	0.005	$6.338 \cdot 10^{-8}$	0.01
Shallow water overtides					
Principal lunar	M_4	6.21	3.865	$4.473 \cdot 10^{-5}$	3.86
Principal lunar	M_6	4.14	5.797	$6.710 \cdot 10^{-5}$	5.80

Frequency spectra

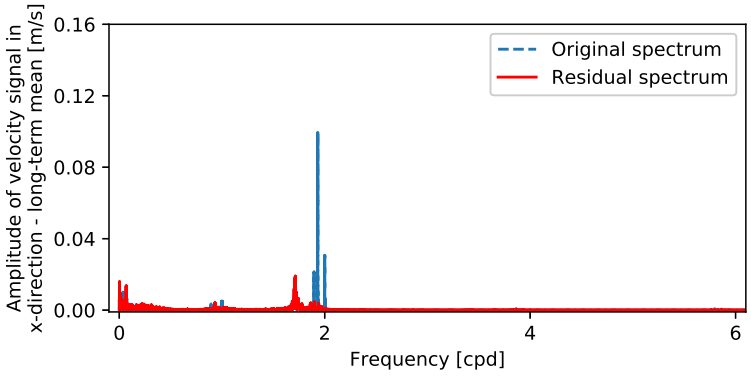

(a) Regular FFT

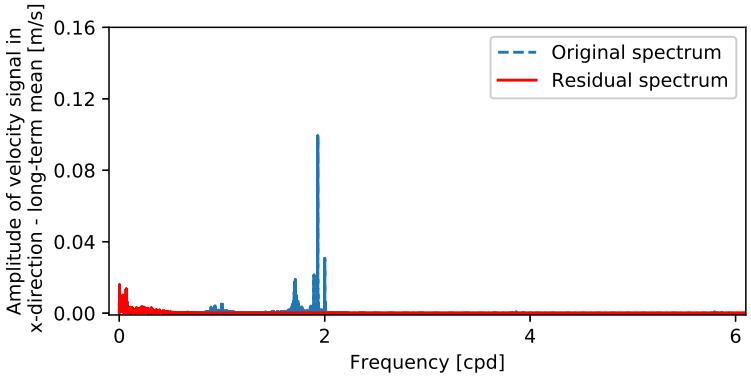

(b) TAPPY FFT

Figure G.3: Frequency spectrum of flow velocity [m/s] in x-direction at Location 1 for (a) a regular FFT and (b) the TAPPY FFT. The original (blue) and residual (red) frequency spectrum are depicted for Layer 14 of the 3D DCSM-FM by Zijl et al. (2016).

Table G.2: Overview of the amplitude [m/s] in x-direction, y-direction and total of the different tidal constituents identified in the TAPPY FFT, see Figures G.3b and 5.1b.

Name	Amplitude [m/s]		
	x-direction	y-direction	Total
M_2	0.1094	0.0758	0.1331
S_2	0.0366	0.0257	0.0447
N_2	0.0244	0.0149	0.0286
K_2	0.0116	0.0079	0.0140
K_1	0.0063	0.0116	0.0132
O_1	0.0044	0.0100	0.0109
P_1	0.0054	0.0050	0.0074
Q_1	0.0040	0.0015	0.0042
M_1	-	-	-
M_f	0.0106	0.0058	0.0121
Mm	0.0091	0.0054	0.0106
S_{sa}	0.0044	0.0022	0.0049
M_4	0.0009	0.0018	0.0021
M_6	0.0008	0.0011	0.0013

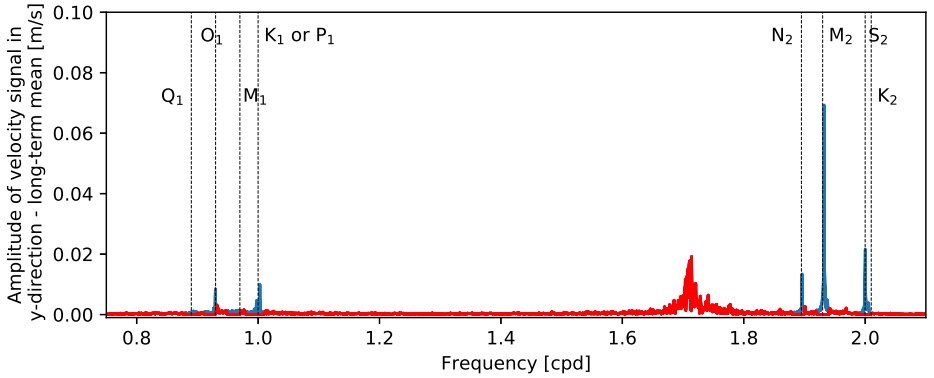

(a) Diurnal and semi-diurnal

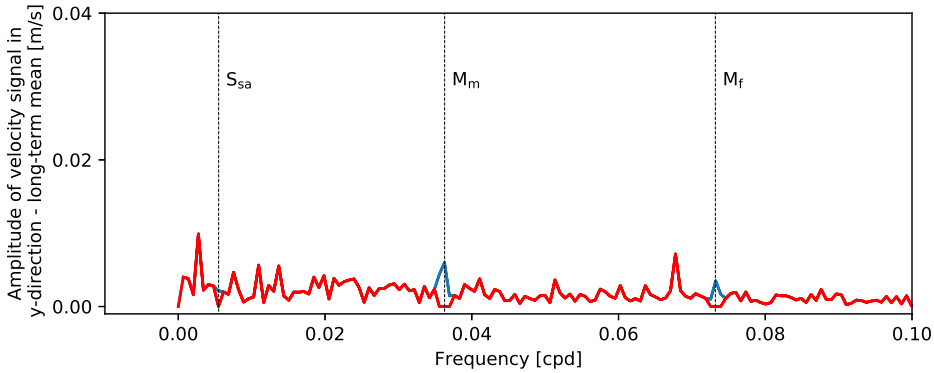

(b) Long period

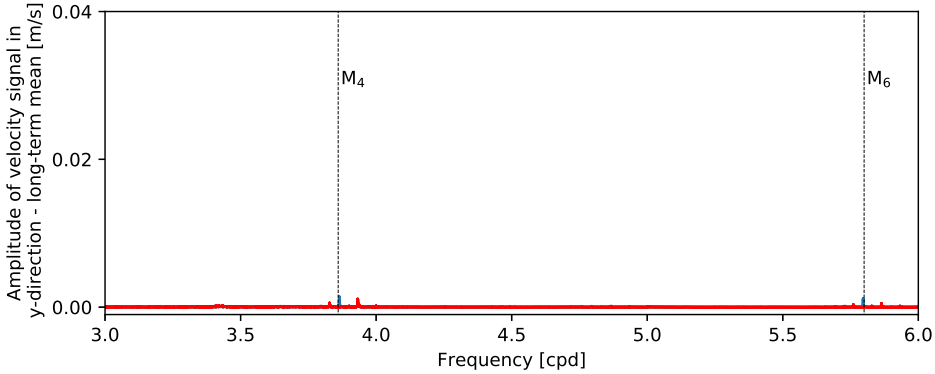

(c) Shallow water overtides

Figure G.4: Presence of the tidal components [m/s] in both the original (blue) and filtered (red) frequency spectrum for (a) the diurnal and semi diurnal components, (b) the components with a larger period and (c) the shallow water overtides. The spectrum is presented for the flow velocity in y-direction in Layer 14 of the 3D DCSM-FM by Zijl et al. (2016).

Details BODC measuring locations

The British Oceanographic Data Centre (BODC) has a database, which contains time series of, amongst others, the flow velocity, flow direction and the sea water temperature in the ocean, collected at different measuring stations. For the validation of the output of the 3D DCSM-FM by Zijl et al. (2016) in Chapter 3, the data from these measuring stations is used. In total, 21 time series are available around the Shetland Islands. Ten of these series are selected based on their duration and depth. The characteristics of the selected time series can be found in Table G.3 and Figure G.5. A plot of the velocity signal from Station 5 can be found in Figure G.6.

Table G.3: Overview of the characteristics of the time series from BODC (2018). The location of each station can be found in Figure G.5.

Time series	Station	Year	Duration [days]	Depth [m]
1	1	1982	80	79
2	2	1994	69	512
3	2	1994	69	150
4	2	1994	69	329
5	3	1982	82	385
6	3	1982	13	272
7	4	1982	164	39
8	5	1972	27	133
9	6	1987	74	96
10	6	1988	103	101

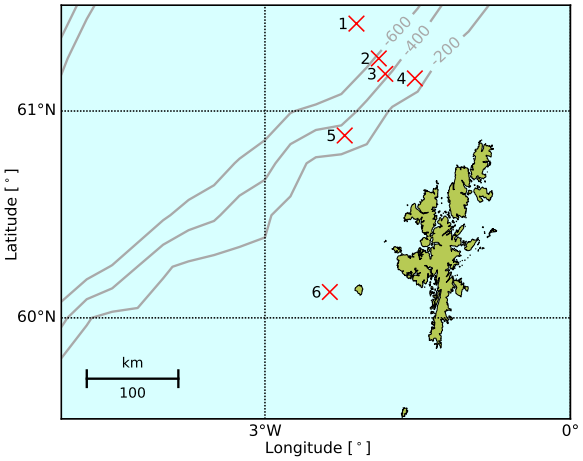

Figure G.5: Overview of the six measuring stations (1 to 6) of BODC (2018) around the Shetland Islands.

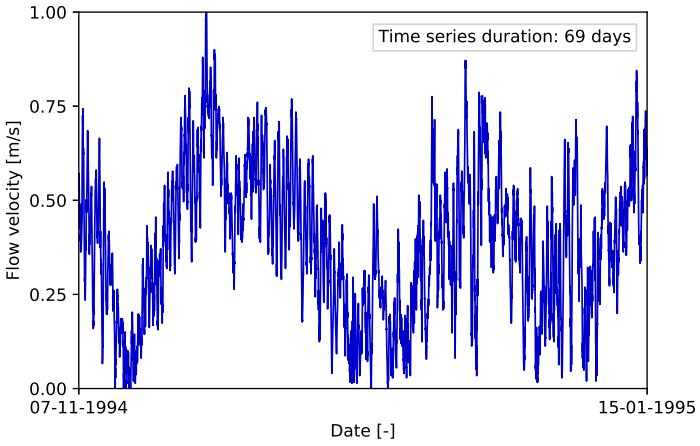

Figure G.6: Plot of the velocity signal [m/s] of the Station 2 time series ranging from 07-11-1994 to 15-01-1995 (BODC, 2018).